Experimental Evaluation of Flow-Measurement-Based Drag Estimation Methods

by

Holly Clowance Neatby

A thesis
presented to the University of Waterloo
in fulfillment of the
thesis requirement for the degree of
Master of Applied Science
in
Mechanical Engineering

Waterloo, Ontario, Canada, 2014

I hereby declare that I am the sole author of this thesis. This is a true copy of the thesis, including any required final revisions, as accepted by my examiners.

I understand that my thesis may be made electronically available to the public.

Abstract

The accuracy of existing methods for estimating the drag based on experimental flow field measurements were assessed for two-dimensional bodies. The effects of control volume boundary placement and inherent simplifying assumptions were also investigated.

Wind tunnel experiments were performed on a circular cylinder operating at a Reynolds number of 8,000 and 20,000, and on a NACA 0018 airfoil operating at a chord Reynolds number of 100,000 for three angles of attack (α), specifically, 5°, 10°, and 15°. The circular cylinder experiments fall within the the shear layer transition flow regime. Airfoil investigations span both types of flow development common to low Reynolds number airfoil operation. For $\alpha = 5°$ and 10°, a separation bubble forms on the upper surface of the airfoil, while, for $\alpha = 15°$, the flow separates without reattaching, resulting in a stalled airfoil.

Wake velocity and pressure measurements were performed at several downstream locations to investigate the impact of control volume boundary placement. Wake profiles were measured between 3 and 40 diameters downstream from the circular cylinder axis and between 1 and 4.5 chord lengths from the trailing edge of the airfoil. In addition to wake profiles, the outer flow velocity variation was quantified to investigate the appropriate location to measure freestream flow characteristics in a test section with streamwise-varying outer flow conditions.

The results show that drag estimates are strongly dependent on the streamwise position of the measured wake profile for all methods investigated. Drag estimates improved, and streamwise variation decreased, with increasing streamwise position of the flow measurements. For the pressure based method examined, wake measurements should be taken at least 10 times the projected model height downstream of the model. In the case of the circular cylinder, this is equivalent to 10 diameters and, for the airfoil investigated, it is approximately 1 chord length from the trailing edge. For the methods relying on velocity measurements, acceptable estimates of drag were possible when based on measurements taken at least 30 projected heights downstream, i.e., 30 diameters for the circular cylinder and 3 chord lengths for the airfoil model investigated.

The findings highlight the importance of providing a detailed description of the methodology and experimental implementation for drag estimates based on flow field measurements. Finally the study offers guidelines for implementing momentum integral based drag calculations in future investigations.

Acknowledgements

I would like to thank my supervisor, Professor Serhiy Yarusevych, for his indispensable guidance, expertise, and common sense. His understanding of experimental work helped avert many disasters and his willingness to help me achieve my goals was remarkable.

I am very grateful for the companionship and assistance my fellow graduate students have provided over the course of this project. Specifically, I wish to thank Tom Kirk and Andrew Lambert for being fellow wind tunnel companions; Chris Morton for being willing to discuss circular cylinders and numerous other topics in great depth; Manpreet Bansal for always being happy to lend a hand; and Mike Boutilier for training on wind tunnel operation and providing the foundation for much of my research.

The laboratory staff, including Jim Merli, Terry Ridgeway, Jason Benninger, and Andy Barber, helped to keep things running smoothly and were involved in construction of experimental equipment. In particular, I would like to thank Jason for building numerous pieces of experimental equipment, including the cylinder model and three-hole probe. And many thanks to Ryan Gerakopulos for building an excellent airfoil model during his tenure; it was an asset to my work.

To the many others, too numerous to mention individually, thank you for keeping me on the rails during my research. Your help, commiseration, friendship, ideas (both good and bad), and cups of tea, have been invaluable.

I also wish to acknowledge the financial support of the Natural Sciences and Engineering Research Council of Canada and the Queen Elizabeth II Graduate Scholarship in Science and Technology, without which this project would not have been possible.

Table of Contents

List of Tables

List of Figures

Nomenclature

b	model unit span
c	airfoil chord length
c_d	drag coefficient, $c_d = \frac{D}{\frac{1}{2}\rho U^2 d}$
$c_{d,p}$	drag coefficient based on surface pressure measurements
$c_{p,w}$	wall pressure coefficient, $c_{p,w} = \frac{p_w - p_\infty}{q_\infty}$
C_α	three hole probe calibration variable; see Eq. 3.1
C_{p_0}	three hole probe total pressure variable; see Eq. 3.2
C_{p_s}	three hole probe static pressure variable; see Eq. 3.3
$c_{p,surf}$	model surface pressure coefficient, $c_{p,surf} = \frac{p_{surf} - p_\infty}{q_\infty}$
d	cylinder diameter
D	drag force
$\vec{F_B}$	body reaction force
G	total pressure, nomenclature specific to Eq. 5.1
G_∞	total pressure in the outer flow, nomenclature specific to Eq. 5.1
l	control volume boundary contour
L	characteristic length
L_m	spanwise length of the cylinder
$\hat{n}$	unit normal vector
p_0	total pressure
$p_{0,min}$	minimum total pressure along a vertically measured wake profile
p_{0-R}	total pressure measured with respect to reference floor pressure tap
p_1	freestream pressure at boundary 1 of the control volume
p_4	outer flow pressure at boundary 4 of the control volume
p_A	mean pressure of tube 1 in three-hole probe
p_B	mean pressure of tube 2 in three-hole probe
p_C	mean pressure of tube 3 in three-hole probe
p_s	static pressure

$p_{s,4}$	static pressure in the outer flow at boundary 4
p_{s-R}	static pressure measured with respect to reference floor pressure tap
p_{surf}	mean model surface pressure at a point
p_w	wall static pressure
p_∞	freestream static pressure
P	static pressure, nomenclature specific to Eq. 5.1
q_0	freestream dynamic pressure, $q_0 = \frac{1}{2}\rho U_0^2$
R_{xx}	Reynolds stress in the $x - x$ plane
Re_c	Reynolds number based on airfoil chord length, $Re_c = U_0 c/\nu$
Re_d	Reynolds number based on cylinder diameter, $Re_d = U_0 d/\nu$
S	control volume surface
u'	streamwise RMS component of velocity
u'_{max}	maximum measured streamwise RMS component of velocity in a vertical wake profile
U	mean streamwise velocity
U_0	outer flow velocity at model pivot location
U_1	freestream velocity at boundary 1 of the control volume
U_4	freestream velocity at boundary 4 of the control volume
U_{min}	minimum streamwise velocity along a vertically measured wake profile
U_∞	freestream velocity
v'	vertical RMS component of velocity
v'_{max}	maximum measured vertical RMS component of velocity in a vertical wake profile
V	mean vertical velocity
$\vec{V}$	velocity vector
$\mathcal{V}$	volume encompassed by the control volume
w	wake half width
x	streamwise distance from the trailing edge of the airfoil model
x_c	chordwise distance measured from the leading edge of the airfoil
X	streamwise distance measured from model pivot point
y	vertical distance from the trailing edge of the airfoil model
Y	vertical distance measured from model pivot point
α	angle of attack
β	top and bottom boundary angle relative to horizontal in four sided control volume
γ	flow angle in X-Y plane relative to X
Δp_c	pressure drop over the inlet contraction

ζ	ratio of velocity in the outer flow at boundaries 1 and 4, $\zeta = U_1/U_4$
θ	angle measured from stagnation point on cylinder surface
μ	dynamic viscosity
ρ	density of air in test section
ρ'	fluctuating component of density
τ	viscous stresses
τ_{xx}	viscous stresses

Chapter 1

Introduction

Airfoils operating at a chord Reynolds number between 10^4 and 5×10^5 can be found in many engineering applications. Examples of these applications are unmanned aerial vehicles, sail planes, and small scale wind turbines [1, 2]. The aerodynamic performance of airfoils operating under these conditions is often of great concern to designers. When operating at low Reynolds numbers, airfoils can exhibit poor aerodynamic characteristics [3]. Understanding the flow development and the corresponding aerodynamic forces is essential for designers employing airfoils which will operate under low Reynolds number conditions. Researchers are also interested in improving low Reynolds number airfoil performance through airfoil design and flow control systems [4]. The success of airfoil improvements is typically assessed through the change in aerodynamic forces, which requires accurate methods of experimentally measuring lift and drag.

The measurement of drag forces has long been of interest, and the importance of drag prediction has increased as design techniques have developed. In aircraft design, slight differences between predicted drag and actual drag can have a significant impact on the potential payload of an aeroplane [5]. Furthermore, as environmental considerations have started to have a larger impact on aircraft design, due to tighter emission regulations and higher fuel costs [6], drag reduction techniques are being investigated as an answer to these concerns. The effectiveness of such techniques can only be accurately assessed by quantifying changes in drag. Even with this long-standing need for accurate methods of

measuring drag, it can be challenging to measure experimentally with the desired level of accuracy [7].

Experimentally measuring the drag of a streamlined body tends to be more challenging than measuring lift. Drag is usually at least an order of magnitude smaller than lift, which makes the relative error due to measurement uncertainty more significant [7]. Additionally, while lift may be affected indirectly by model support components in terms of flow development, the components are unlikely to directly contribute to the lift. However, this is not the case with drag, where model support components and other devices, such as endplates, increase the measured drag of a model. Model drag must then be differentiated from support component drag [7]. In the case of an airfoil operating at a low Reynolds number, there are several characteristics of flow development which further complicate drag measurements.

Airfoils operating at low Reynolds numbers are prone to laminar boundary layer separation which is primarily responsible for the associated poor aerodynamic performance [2]. Once separated, the boundary layer undergoes transition to turbulence and either reattaches forming a separation bubble, or remains separated, stalling the airfoil [2]. Another characteristic of flow development over an airfoil at a low Reynolds number is sensitivity to experimental conditions [8]. Parameters including Reynolds number, turbulence intensity, blockage, and experimental set up, affect the flow development on the airfoil and, consequently, the aerodynamic forces.

The discussed features of low Reynolds number flows raise several concerns regarding measuring aerodynamic forces acting on an airfoil in such conditions [9]. Specifically, the two distinct forms of flow development that are common to low Reynolds number airfoils mean any measurement technique applied in drag measurements must be suitable for both attached and separated flows. Since the flow development is sensitive to disturbances, the drag technique cannot require significant alterations to the experimental setup which might affect flow development. This might be the case if it is necessary to alter model supports or remove devices such as end plates to enable drag measurements [7].

There are three primary methods for experimentally measuring the drag of a body: direct force measurements, surface measurements, and conservation of linear momentum

based methods [7]. For low Reynolds number airfoils, the method which promises to be most suitable is one based on conservation of linear momentum. Such a method can be implemented without altering the model mounting setup or, in most cases, the flow conditioning devices such as endplates. Also, if suitable flow measurement equipment is selected, the method is appropriate for streamlined and bluff body flows [5]. The basis of this technique is applying conservation of linear momentum to a control volume encompassing the airfoil, which requires flow field measurements [5].

The motivation for the present work was to measure the drag of a low Reynolds number NACA 0018 airfoil, operating in a closed test section, using an experimental technique based on conservation of linear momentum. This method of experimentally measuring drag has been in use since the 1920's [10]. The theoretical formulation which forms the basis of the experimental methodology has been modified for specific applications in a number of studies [5, 6, 11–13]. However, a direct implementation of this technique is hindered by a scarcity of information regarding the details of necessary experimental measurements, e.g. the location and extent of wake measurements, and the uncertainty in generated drag estimates.

The primary goal of this study is to develop a standard methodology for applying conservation of linear momentum to experimentally measure the drag of a low Reynolds number airfoil. To accomplish this, first the drag of a circular cylinder is estimated through application of conservation of linear momentum based on experimental measurements taken in the flow field. The findings of the cylinder experiment are then applied to estimate the drag of a low Reynolds number airfoil. The following main objectives are set for this study: (i) detail common simplifying assumptions and provide concrete qualification to their applicability, (ii) evaluate the accuracy of several drag formulations, (iii) quantify the effect of measurement location and identify appropriate bounds, and (iv) estimate the error in drag measurements obtained through the formulation and experimental methodology employed. All aspects of these objectives will be combined to arrive at recommendations for implementing conservation of linear momentum based drag measurements in two-dimensional, incompressible flows.

Chapter 2

Background

The main focus of this thesis is developing a robust method, based on conservation of linear momentum, for experimentally determining the drag of a submerged body in a low-speed flow. A brief outline of experimental methods of measuring aerodynamic forces is presented below. This is followed by a more detailed review of the history of linear momentum based drag techniques and the challenges which prevent drag from being reliably estimated solely from existing information on the experimental implementation. An introduction to the flow over a circular cylinder and low Reynolds number airfoil are included since these represent the two experimental test cases used to verify and refine the methodology of measuring drag.

2.1 Low Reynolds Number Flow Over an Airfoil

A brief overview of airfoil operation at low Reynolds numbers is provided here to highlight key aspects of airfoil behaviour under these conditions. In depth reviews of the topic can be found in the work of Carmichael [15], Lissaman [2], and Mueller [3]. An airfoil is operating under low Reynolds number conditions when the chord Reynolds number (Re_c) is between about 10^4 and 5×10^5. The boundary layer that develops over the surface remains laminar for a much greater extent of the airfoil surface than at higher Reynolds numbers [15]. Thus, the laminar boundary layer is likely to encounter an adverse pressure gradient and

is therefore prone to separation [15]. Upon separating, the shear layer is unstable and transition to turbulence occurs. After transitioning the shear layer may either reattach or remain separated, stalling the airfoil [2]. These two regimes are pictured in Fig. 2.1. Shear layer separation results in a relatively wide wake forming behind the airfoil [16]. In the case of reattachment, a much narrower wake forms and the turbulence intensity decreases [16].

Airfoil behaviour at low Reynolds numbers is primarily determined by the airfoil profile, Reynolds number, and angle of attack (α). At a specific Reynolds number, there is a critical angle which divides the two regimes of flow development. Below the critical angle,

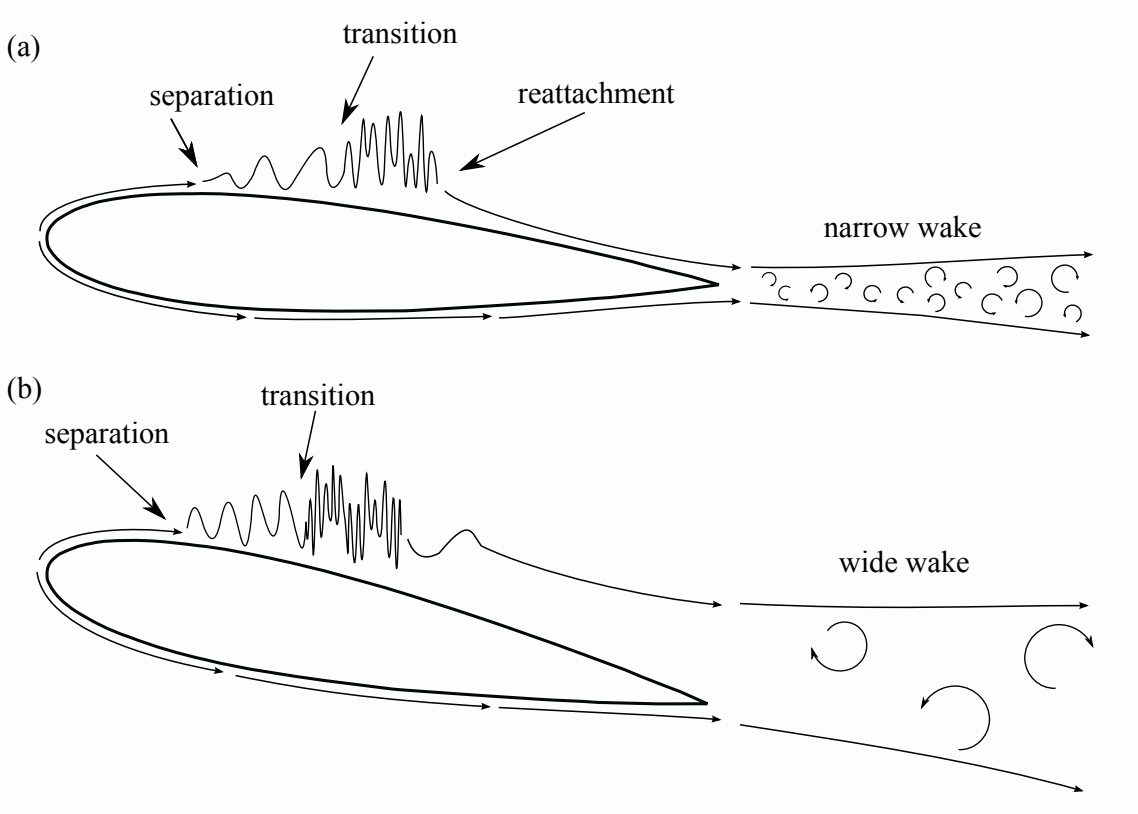

Figure 2.1: Two flow regimes common to low Reynolds number airfoil operation, based on illustration in Yarusevych et al. [14]: (a) laminar separation bubble; (b) separation without reattachment.

a separation bubble forms, and above it the airfoil stalls. The critical angle is affected by flow hysteresis; it changes based on the initial flow development [1, 17]. For a specific airfoil, the critical angle increases with Reynolds number.

Low Reynolds number airfoil experiments are sensitive to freestream turbulence intensity, Reynolds number, and test section disturbances [17]. For example, Boutilier and Yarusevych [18] show that endplates not only increase the two-dimensionality of the flow but also affect the size and location of the separation bubble. In turn, flow development is closely linked to aerodynamic forces [19–22]. This can lead to different aerodynamics forces recorded in separate facilities for the same parameters [17].

Since flow development and, therefore, aerodynamic forces are affected by experimental conditions, it is beneficial if force measurements can be linked with flow development. The current study focuses on measuring the drag of a NACA 0018 airfoil. The flow development over the airfoil and aerodynamic forces, excluding drag, have previously been studied in the same facilities. The results of this work can be found in Refs. [23] and [16]. The completion of the present study will add information on the drag and wake development, to create a complete set of experimental data detailing flow development and aerodynamic force for the NACA 0018 airfoil.

2.2 Flow Over a Circular Cylinder

The following is a brief description of flow development over circular cylinders. Extensive reviews on the subject include the following works: Roshko [24], Williamson [25], Norberg [26], and Zdravkovich [27, 28]. The boundary layer that develops over a cylinder initially faces an adverse pressure gradient and, except at very low Reynolds numbers, will eventually separate. With the exception of very low Reynolds numbers, the separated flow will transition to turbulence [25]. The angle of separation and location of transition are affected by Reynolds number [27]. For flows where the separated shear layer transitions to turbulence, the regimes that arise can be divided into the following categories: $200 < Re_d < 400$ turbulence transition occurs in the wake [27], $400 < Re_d < 200,000$ transition occurs in the separated shear layer [27], and $Re_d > 200,000$, transition occurs in

the attached boundary layer [27]. The experimental tests in this study fall into the range of $400 < Re_d < 200,000$ which is common in many engineering applications [26], as well as permitting a greater flexibility in selection of Reynolds number.

For $400 < Re_d < 200,000$, transition to turbulence occurs in the shear layer prior to roll up [29]. The vortices that form, through shear layer roll-up, combine to form a turbulent wake [29]. Vortices develop within the wake formation region, which extends up to 3 diameters (d) downstream of the cylinder [27]. A vortex street is formed in the cylinder wake as vortices are shed alternatively from either side [27]. As the eddies are carried downstream in the wake, they decay, becoming less coherent [30]. The flow development and wake growth is pictured in Fig. 2.2. In a plane unbounded wake, the width grows proportionally to $X^{1/2}$ and the maximum velocity deficit decays proportionally to $X^{-1/2}$ [31]. However, in experimental tests where blockage plays a role, wake growth is diminished [32].

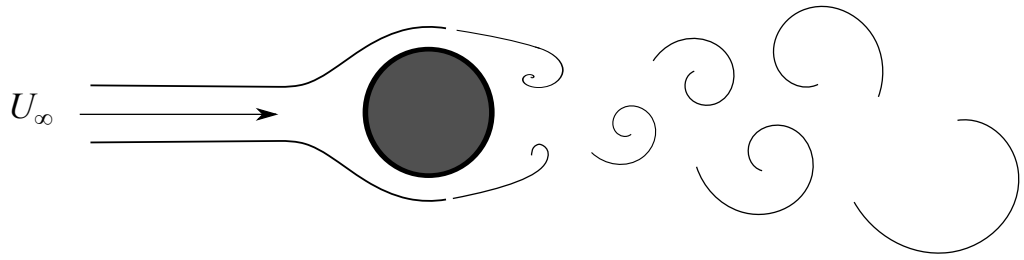

Figure 2.2: Flow development over a circular cylinder.

Vortex shedding induces unequal instantaneous pressure distributions on the surface of the cylinder, leading to fluctuating lift and drag forces [33, 34]. The mean aerodynamic force consists of drag alone; the lift, on average, is zero [33]. The total drag experienced by a cylinder consists of skin friction and pressure drag. However, the contribution to total drag from skin friction is less than 4% in the flow regime studied, allowing drag to be estimated solely from the surface pressure distribution [35].

2.3 Experimental Methods of Measuring Drag

Experimental methods of measuring aerodynamic forces can be classified as belonging to one of two categories: direct and indirect techniques [5]. Force balances provide a method of measuring drag directly. Indirect techniques include both surface measurements and momentum integral methods. Since each technique has its own benefits and shortcomings, the most appropriate method depends upon the experimental conditions. These include the fluid, dimensionality of the flow, compressibility effects, and test facilities.

Force balances are widely used for steady and unsteady drag measurements [36] and have the advantage of measuring forces directly. However, the measured drag is a combination of drag due to the model, support components, and end effects [7]. A method of separating these components is necessary before model drag can be found. Force balances are widely used in experiments where model supports, or models themselves, can be modified to accommodate balance measurements without significantly affecting flow development [7, 36]. For low Reynolds number flows, which are particularly sensitive to experimental setup, force balances are often employed in investigations where drag trends, and not absolute drag values, are of interest [37].

Surface measurements are often used to determine the lift of streamlined bodies, e.g. airfoils, and the drag of bluff bodies, such as circular cylinders [5]. In both situations, the primary contribution to the force is from normal forces and surface shear stress has a minimal effect [35]. This technique is not as easily applied for drag measurements of streamlined bodies since surface shear stresses are not negligible [5], but surface shear stress measurements are experimentally challenging to obtain [38].

While the momentum integral method of determining forces could be applied to calculate both lift and drag of a body [5], it is employed primarily for drag measurements. The momentum integral method has been used to calculate drag in a wide variety of experimental investigations [6]. Often, momentum integral methods can be employed to determine drag without altering the model setup and, since the technique relies on flow field measurements, drag calculations can be combined with investigations of flow field development. Under some experimental conditions, instantaneous drag measurements can be linked directly with specific flow features [12]. However, the specifics of the momentum integral

drag formulations vary greatly between experimental implementations [5,6,10]. One of the challenges in using the momentum integral technique to determine drag is selecting the suitable formulation for the specific experimental setup.

2.4 Momentum Integral Drag Measurements

Momentum integral methods of determining drag are based on conservation of linear momentum. This is translated into an experimental technique by applying conservation equations to a fixed control volume encompassing the model. A general sketch of such a control volume is shown in Fig. 2.3. Conservation of linear momentum for a fixed control volume is given by Eq. 2.1 taken from [39].

$$\sum \vec{F} = \frac{d}{dt}\left(\iiint_{\mathcal{V}} \vec{V}\rho \, \mathrm{d}\mathcal{V}\right) + \iint_{S} \vec{V}\rho \left(\vec{V}\cdot\hat{n}\right) \mathrm{d}S \tag{2.1}$$

Included on the left hand side of Eq. 2.1 is the body force, force due to pressure acting on the control volume, and force due to viscous stresses. The right hand side represents the

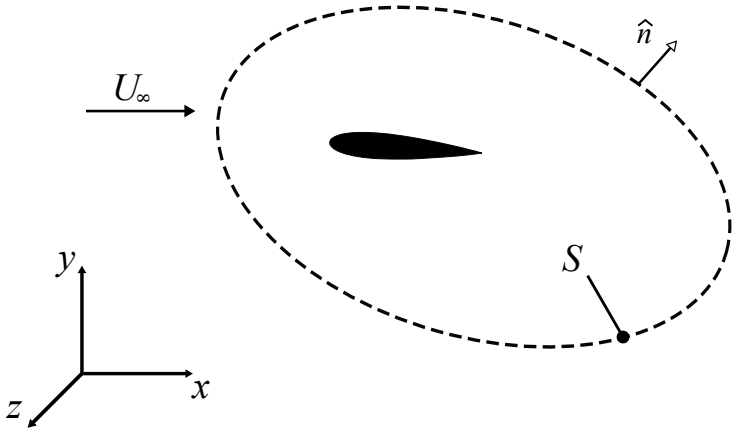

Figure 2.3: General control volume formulation.

rate of change of linear momentum in the control volume [39]. The method is implemented experimentally by measuring the required flow properties in the control volume, computing the integral quantities, and calculating the resulting drag. Practical implementation of the method dictates that Eq. 2.1 is simplified prior to measuring flow properties. In addition, properties which cannot be measured directly must be eliminated from the analysis or a suitable approximation must be applied.

2.4.1 Historical Development

The theory which forms the basis for the momentum integral method has existed for many years and it has been implemented as an experimental method for determining drag for nearly as long. It is documented as being employed by Froude to estimate the skin friction on the hull of a boat in the 1800's [40]. Since that time, it has been applied in many forms to determine the drag of operational aircraft [10], experimental models [11, 12, 41–43], and computational simulations [5, 44]. The flow conditions which it has been applied to include two- and three-dimensional, and compressible and incompressible flows. Flow field quantities in these experiments have been obtained through pressure measurements, hot-wire probes, and particle image velocimetery (PIV), to name only a few.

Even though this method of measuring drag has existed since the 1800's, its prominence rose in the 1920's, when the topic was independently investigated by Betz [45] and Jones [10]. While the specifics differed between the methods developed by Betz and Jones, the end goal was to measure the section drag of a wing [10]. At the time their work was undertaken, it was known that wing drag could be determined from flow properties measured far downstream of the wing [10]. However, this seriously limited the practical implementations of the method and increased uncertainty in section drag coefficients due to wake interactions [10]. To allow in-flight measurements and isolate section drag, both Betz and Jones proposed methods for which measurements can be taken relatively close to the trailing edge [10]. The two methods provided similar results for most of the experimental test cases investigated [10], and form the basis of most methods presently employed [6,11]. Other early contributors to this field of research include the work of Taylor [40] and Fage and Jones [46].

Since the work of Betz and Jones, many researchers have revisited the momentum integral formulation. Their goals have included reducing the flow field limitations associated with existing methods, applying it with new measurement techniques, or adapting it for a specific application. With reference to Betz's work, Maskell [11] developed a formulation applicable to three dimensional, incompressible flows. The theory was extended to general compressible flows independently by ONERA [6], van Dam [5], and Kusunose [13]; all three investigations employed unique approaches to the problem [6].

This description of existing drag formulations based on conservation of linear momentum is not intended to be comprehensive, but does cover the major developments in the area. Other formulations have been developed and employed for drag measurements; however, they tend to focus on adapting the methodology to specific experimental investigations. One notable example is the work performed by van Oudheusden [12, 44] focused on calculating model drag through PIV measurements.

2.4.2 Experimental Implementation

While there exists a large body of work on the topic of applying conservation of linear momentum to determine drag, it can be challenging to find a method suitable for the experimental investigation being undertaken. Not only does the method selected have to be appropriate to the flow conditions and type of experimental measurements feasible, but there are other impediments to be overcome. They include identifying the appropriate location to conduct measurements, applying valid simplifying assumptions, selecting an appropriate reference condition if applicable, and correctly identifying and quantifying experimental limitations.

Simplifying Assumptions

To circumvent the physical limitations associated with experimental work, simplifying assumptions and approximations are employed in virtually all momentum integral formulations. In addition to reducing the drag formulations to measurable quantities, simplifying assumptions have been used to reduce the number of required flow measurements

to minimise experimental cost. However, when simplifying assumptions are employed, restrictions are placed on the flows for which the formulation is valid, such as the flow dimensionality. The simplifying assumptions used to generate specific drag formulations are not always clearly documented or defined, making it challenging to apply the existing drag formulation in new experimental applications. The simplifying assumptions which introduce uncertainty generally relate to flow properties affected by measurement location, determined by the control volume boundary placement.

For simplicity, one can consider a quadrilateral control volume depicted in Fig. 2.4, in the following discussion. An assumption which is common to the majority of momentum integral formulations is that the upstream boundary (boundary 1 in Fig. 2.4) is located far enough upstream of the model, so that it is located in uniform freestream flow. Upstream flow conditions must therefore be measured far enough upstream, where model effects are negligible. If drag measurements are taken under non-uniform freestream conditions standard momentum integral drag formulations are no longer valid.

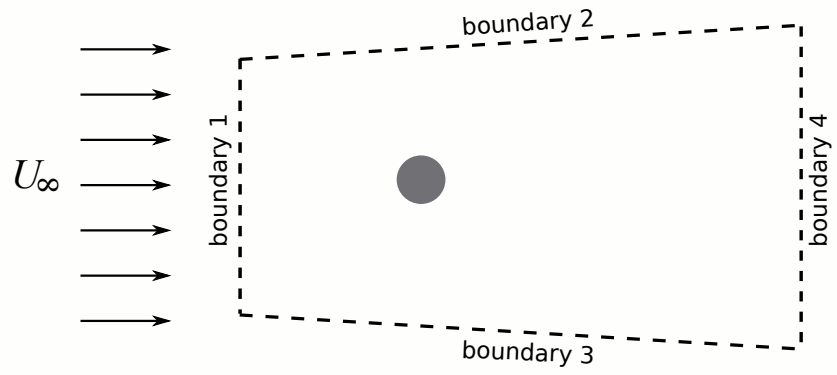

Figure 2.4: Quadrilateral control volume with boundary labels.

Momentum integral formulations are usually based on a body operating in an unbounded flow and the top and bottom boundaries (2 and 3 in Fig. 2.4) are generally assumed to be located in the uniform freestream. For experiments conducted in finite test sections, the outer flow along 2 and 3 will likely differ from an unbounded flow field due

to blockage effects. However, the variation along boundaries 2 and 3 is often neglected, and the error due to this approximation has not been quantified. Not all drag formulations assume uniform freestream conditions along boundaries 2 and 3. Some researchers have addressed this issue through modification of the drag formulation. In Ref. [43], average mass flux across this boundary is used to approximate the momentum flux, and, in Ref. [47], these boundaries are assumed to lie on streamlines. In both cases, further simplifying assumptions were necessary to employ these approximations.

It is along the downstream boundary (boundary 4 in Fig. 2.4) where assumptions tend to vary dramatically between different drag formulations, which leads to variation in the restrictions on downstream boundary placement. A lack of summative guidelines prevents the researcher from easily being able to identify the limitations in measurement location for specific experimental measurements and the error introduced by the choice of boundary location. Van Dam [5] reports that the standard location for airfoil wake measurements is one chord length downstream from the trailing edge. However, no quantitative analysis is provided to support this standard. Also, the standard is not necessarily applicable to bluff bodies or stalled airfoils.

There are several studies which provide more concrete information on the effects of specific simplifying assumptions and control volume placement. However, even when combined, there is still insufficient information to generate guidelines for employing conservation of linear momentum to estimate drag. In experiments on streamlined bodies at angles of attack below stall, the viscous stress term tends to be negligible even when measurements are conducted less than one chord length downstream from the model [5]. In contrast, for flows over bluff bodies, the viscous stress is more significant in the near wake [5]. For a circular cylinder, the contribution of Reynolds stresses towards the momentum integral drag estimate has been quantified by Antonia and Rajagopalan [48]. They found it to be significant up to an $X/d = 30$. Specifically, these terms account for 22% of the drag coefficient (c_d) at $X/d = 5$, and 5% at $X/d = 20$ [48]. The rate of decay of Reynolds stresses likely differs in the wake of a streamlined body, preventing these findings from being applicable to such models [48]. To allow pressure recovery in the wake, Barlow et al. [7] recommends that measurements be made at least 0.7 chord lengths downstream. On

the other hand, the data presented by van Dam [5] indicates that pressure recovery is still occurring up to 10 chord lengths downstream.

Reference Conditions

Momentum integral formulations for estimating drag are often based on the assumption of unbounded, uniform flow [5, 10]. The fact the flow is unbounded is usually an implicit assumption. The effects of the body are limited to a narrow region surrounding the model and the wake. This is the situation which prevails in free flight experiments, such as the originally intended application of the methods developed by both Betz [45] and Jones [10]. However, for experiments conducted in confined test sections, the flow conditions often differ from those found in an unbounded flow [7]. In particular, the freestream parameters change along the test section due to blockage effects. This is problematic in employing momentum integral equations since the majority of them are written in terms of a reference velocity, usually the freestream velocity. This variation was noted in 1936 by Jones [10] in an appendix note. His study was designed to experimentally verify the drag calculations through wind tunnel measurements behind an airfoil and free flight measurements on a wing [10]. Wind tunnel measurements proved especially challenging for several reasons, one of which being the quantification of reference pressure [10]. Daily variation in experimental conditions made a standard pressure reference unsuitable, instead it had to be measured during each run [10]. To achieve this, wake measurements were extended outside the velocity deficit region and pressure measurements were taken at this location to define the reference [10]. It was suggested that measuring the reference pressure upstream of the model would have been more suitable, however it was not possible [10].

Takahashi [42] explored the consequences of failing to account for variation in the outer flow velocity. There is a paradox which arises when the following conditions are applied in developing the momentum integral equation: uniform inlet freestream, applying Bernoulli's equation along the sides of the control volume, and satisfying the conservation of mass [42]. The three cannot be simultaneously enforced, e.g. if the first two are applied, then mass is not conserved in the control volume. To ensure conservation of mass, Takahashi assigned a non-physical velocity at the upstream boundary; however, the resulting drag estimates re-

mained unsatisfactory [42]. Other researchers have attempted to address this issue through various means. Bohl and Koochesfahani [43] modified the momentum integral equation to account for variation in the outer flow. Mass in the control volume was conserved by approximating the mass flux through the top and bottom boundaries [43]. Zaman and Culley [37] noted that the outer flow velocity in the wake profile was greater than the reference velocity, U_∞. To address this, wake profiles were truncated at an arbitrary value of $U/U_\infty = 0.95$ [37]. While the discrepancy between unbounded flow and test conditions has been noted and, in some cases, accounted for, the effect on drag estimates has not been quantified.

Chapter 3

Experimental Methodology

This study is focused on implementing an experimental technique for measuring the drag of two-dimensional bodies, submerged in incompressible flows and developing comprehensive guidelines. To verify the accuracy of the drag technique, for specific flow situations, the method was applied in the experimental investigation of a circular cylinder and an airfoil. The resulting drag estimates were compared to values found through alternative methods of estimating drag applied to the same experimental measurements. Details of the wind tunnel facility, models, experimental measurements employed, and methods of analysis used are provided in the following sections. Experimental uncertainty and the uncertainty in drag estimates are detailed in Appendix A.

3.1 Experimental Setup

Experimental work presented in this study was conducted in an adaptive-wall, suction-type, open-return wind tunnel at the University of Waterloo. Flow conditioning is accomplished through an aluminium honeycomb structure and a series of four steel screens, located upstream of the 9.55 contraction. Details regarding the flow conditioning can be found in Ref. [49]. Freestream turbulence intensity is less than 0.3% for all tests presented in this study. The freestream velocity is set by measuring contraction pressure drop, Δp_c, with a resulting uncertainty of less than 2.5%. The contraction pressure drop is measured from

six, 1 mm, static pressure taps; a set of three taps are located on the walls of both the large and small areas of the tunnel contraction. The pressure taps are connected, through 1.6 mm tubing, to an inclined manometer with a resolution of 1.25 Pa.

The 6.0 m long test section is nominally rectangular with a width of 0.61 m and an initial height of 0.89 m. The test section has two fixed and two adjustable walls. The top and bottom walls, roof and floor, are adaptable, while the two side walls, front and back, are permanently fixed. The roof and floor are made of Lexan and can be contoured to the desired shape along the entire length of the test section. The front and back fixed walls of the test section are respectively made of clear cast acrylic and particle board, to allow observation of the experimental set up [49]. The gaps between the rigid and adjustable walls are filled by rubber seals pressurized to 150 kPa as recommend by Sumner [50].

The adaptable walls are contoured with 48 independent rack and pinion type jacks. The jacks are spaced 100 mm apart for a 2.25 m span, in the region of the model mounting assembly, to allow for refined adjustment in this area, and 150 mm apart elsewhere. The linear resolution of the jacks is 0.1 mm and the uncertainty in wall position is ± 1 mm. For all tests in this study, the walls of the test section were set in the aerodynamically straight wall (ASW) configuration. In the ASW configuration, the walls are contoured to accommodate boundary layer growth on the four walls of the empty test section. The boundary layer growth is predicted using the $1/7^{th}$ power law for turbulent boundary layers, as described in Ref. [50]. The accuracy of this approach was verified through boundary layer measurements for a chord Reynolds number of $10,000$ in Ref. [8]. The ASW configuration results in a constant centreline velocity, thereby creating a neutrally buoyant test section. Wall coordinates for the ASW configuration are dependant on the freestream velocity in the test section. Therefore, while all tests were conducted with walls in the ASW configuration three different sets of wall coordinates were employed; one for each freestream velocity. The wall coordinates are provided in Appendix B.

The floor and roof of the test section are equipped with 70 pressure taps, positioned along the centreline. The 1 mm static pressure taps are drilled normal to the surface every 50 mm in the region surrounding the model, and 150 mm apart in the remainder of the test section. The taps are connected to two parallel pressure transducers by 1.6 mm flexible

tubing. The tubing is routed though a series of Scanivalve mechanical multiplexers to allow measurement of wall pressure distributions. The pneumatic and wiring diagrams for the Scanivalve control system can be found in Ref. [8].

3.2 NACA 0018 Model

Airfoil testing was conducted on a NACA 0018 airfoil that has an anodized aluminium shell. The model has a chord length, c, of 200 mm and a span of 600 mm. The model axis of rotation is located on the chord line, $0.3c$ from the leading edge. When mounted in the test section, the axis of rotation is fixed $10c$ downstream from the test section inlet. The airfoil has 65 built-in, chordwise pressure taps, 0.4 mm in diameter, located on a center-span plane. Surface pressure profiles are measured by sequentially connecting two pressure transducers to the model pressure taps with a series of Scanivalve mechanical multiplexers. The model pressure taps are connected to the multiplexers with 0.8 mm tubing. More detail regarding airfoil design and construction can be found in Ref. [51].

The coordinate systems relating to the airfoil model are pictured in Fig. 3.1, where x_c is the chordwise distance from the leading edge, X-Y the horizontal and vertical distance from the model axis of rotation, and x-y the horizontal and vertical distance from the trailing edge of the airfoil, at a given angle of attack. The angle of attack is set with a digital protractor, which has a resolution of 0.1°.

Circular endplates with a diameter of $2.25c$ were installed during all tests to increase the two-dimensionality of the flow over the center-span of the airfoil. An endplate spacing of $2.0c$ was used based on the recommendations of Boutilier and Yarusevych [18]. More details regarding endplate design and the effect of positioning can be found in Ref. [18]. Solid blockage is increased by 1.1% by the installation of endplates with the test section wall in the ASW configuration for $Re_c = 10,000$. Two, 5 mm endcaps, cut to the airfoil profile, were used to fill the gaps between the ends of the model and test section walls. The solid blockage due to the airfoil model, with endplates installed, varies between approximately 5% at $\alpha = 0^\circ$ and 8% at $\alpha = 15^\circ$.

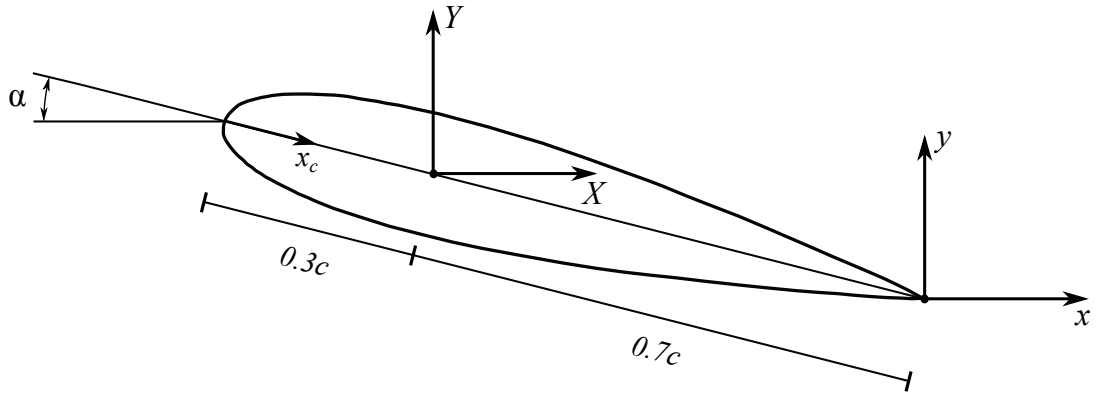

Figure 3.1: Coordinate systems related to the airfoil model.

3.3 Circular Cylinder Model

A uniform circular cylinder model, with a diameter, d, of 22.7 mm, was used for all cylinder wake investigations. The model is equipped with a single 0.5 mm pressure tap on the center-span. The tap is connected to a single pressure transducer, located outside the test section, by tubing 1.6 mm in diameter. Surface pressure distributions were recorded by rotating the model, and embedded pressure tap, through 180°. The angle was set by a digital protractor, with a resolution of 0.1°. Endplates were employed to create a two dimensional flow over the center span of the cylinder. The length of the model, L_m, between endplates is $21.5d$. The endplates were installed on the cylinder outside the wall boundary layer. Circular endcaps were used to fill the 5 mm gaps between the ends of the model and the test section walls.

Endplates were necessary since the L_m/d ratio of the model is less than 30. With this ratio, endplates are required to ensure a two-dimensional region of flow [52]. Circular endplates with a diameter of $7d$ were designed for this model setup. Circular endplates were selected over rectangular endplates [53] to prevent the blockage ratio and flow development from changing with model rotation. The endplate diameter was based on the

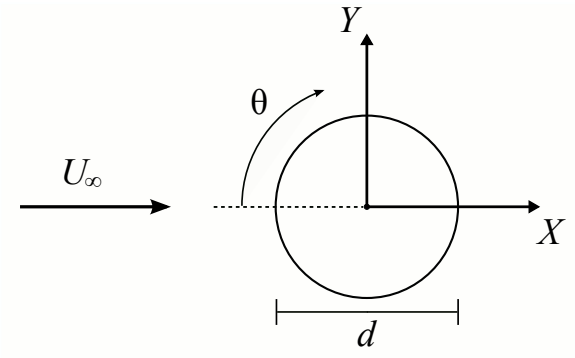

Figure 3.2: Coordinate system belonging to the circular cylinder model.

recommendations of Stansby [53] for the dimensions of rectangular endplates. The outer circumference of the endplates have a 30° chamfer.

3.4 Hot-wire Measurements

A cross-wire was used to measure mean and root mean squared (RMS) velocity profiles in the wake. The cross-wire was oriented to resolve the horizontal, U, and vertical, V, components of velocity. The probe was a Dantec miniature 55P61 cross-wire probe operated with a Dantec StreamLine Pro bridge. Bridge balancing was performed through the Dantec StreamWare Pro software. The voltage signals were digitized with a National Instruments PCI - 4472 data acquisition card.

The cross-wire was calibrated in-situ against a pitot-static tube, located 10 mm below the cross-wire. To perform the calibration, the hot-wire and pitot-static tube were moved into the freestream, upstream of the model and in the upper half of the test section. The pitot-static tube was connected to an inclined manometer with a resolution of 1.25 Pa. The cross-wire was calibrated for the range of velocities expected during experimental testing. A 5^{th}-order polynomial fit was used to generate calibration curves for interpolating velocities between calibration points [54].

The cross-wire was positioned in the flow with a three axis traversing assembly. The

positioning of the traversing mechanism is accurate within ±0.05 mm. More details regarding the traversing mechanism can be found in Ref. [55]. The probe holders were extended upstream from the rails of the traverse system by a 12.7 mm diameter sting. The measurement location is 500 mm upstream of the traverse rails. The solid blockage of the traverse system is approximately 4.5% in the nominal test section. It was verified through wall pressure distributions measured while moving the traverse system in the test section, that the traverse does not affect the flow development in the flow region of interest.

A sampling rate of 5000 Hz was used for all hot-wire measurements. Sample length was based on the flow conditions at the measurement location, however, the minimum sample duration was 20 s. For tests where a longer sample time was employed, the specific sample length has been noted. The estimated uncertainty in the freestream mean velocity values is less than 1%, this increases to a maximum of 12% in highly turbulent wake regions [56]. More details regarding the hot-wire uncertainty can be found in Appendix A.

3.5 Pressure Measurements

Pressure measurements were performed during the experimental work included in this study to characterize the following parameters: pressure drop along the contraction (Δp_c), wall static pressure (p_w) distributions, pitot-static tube parameters, model surface pressure (p_{surf}) distributions, and three-hole probe parameters. To accomplish these pressure measurements, six pressure traducers, and an inclined manometer were employed. The pressure transducers, operating range, signal output, and application are listed in Table 3.1. All transducers were calibrated against a Druck DPI 610 Pressure Calibrator. Zero offsets were measured prior to each experimental run to account for any drift due to changes in ambient conditions. The voltage signals were collected with a National Instruments PCI - 6221 data acquisition card.

3.5.1 Test Section Wall Static Pressure

Wall pressure distributions are measured from the 70 floor and 70 roof pressure taps. The wall pressure taps are connected to the pressure transducer through a Scanivalve mechani-

Table 3.1: Details of the pressure transducers employed in the current study.

Transducer	Range [Pa]	Output [V]	Measurement
Inclined Manometer	0 - 63	-	Δp_c
			Pitot-static tube (calibration)
Lucas Schaevits	±250	0 - 5	(1) p_w, p_{surf} - airfoil, p_B
P3061-2WD			(2) p_w, p_{surf} - airfoil, p_C
All Sensors	±250	0 - 5	(1) p_{0-R}
1-INCH-D-4V			(2) p_{s-R}
Setra-239 0.5WC	±125	-2.5 - 2.5	p_{surf} - cylinder, Δp_c
Setra-239 1WC	±250	-2.5 - 2.5	p_A

cal multiplexer. Pressure is measured with respect to a reference floor pressure tap, located 1.3 m upstream from the model axis of rotation. Wall pressure coefficients were measured with the traverse system placed at the furthest downstream position, approximately 1.1 m from the model pivot point, with the vertical arm against the test section wall and the sting located at the half-way point of vertical travel. A rise time of 25 s was used for pressure measurements, with the exception of initial pressure measurements where a 60 s settling time was employed. Mean pressures were determined from 20,000 samples at 5000 Hz. The uncertainty in the wall coefficients of pressure is estimated to be less than 3.0% of freestream dynamic pressure for all tests presented in this study.

3.5.2 Pitot-Static Tube

During wake profile measurements the pitot-static probe was used to measure total (p_{0-R}) and static (p_{s-R}) profiles independently. This was accomplished by measuring both values with respect to a common reference pressure, a floor tap 1.3 m upstream from the model. Two identical pressure transducers were employed to measure the two profiles; indicated by 1 and 2 in Table 3.1. The pitot-static tube was positioned with the same traverse system as the cross-wire, see Section 3.4 for more details. Hot-wire velocity profiles and pitot-static pressure profiles were measured simultaneously, with the pitot-static probe mounted 10

mm beneath the hot-wire probe. The total pressure port and the wire cross were aligned within approximately 0.5 mm in the streamwise direction.

3.5.3 Three Hole Probe

The wake of a circular cylinder and a stalled airfoil have large regions of rotational, highly turbulent flow [16, 27]. These aspects make a pitot-static tube an unsuitable tool for measuring the pressure distribution in the wake. To investigate the significance of the error in drag calculations due to pitot-static measurements, and to provide an alternative measurement technique, a three-hole probe was also employed to measure wake profiles. The three-hole probe was selected as the alternative since it is a pressure based technique suitable for two dimensional flows.

The tip design of the three-hole probe is shown in Fig. 3.3. This design was selected over other existing three-hole probe configurations for robustness and simplicity of construction [57]. Having a tip angle of 45° and the space between tubes filled decreases the pitch sensitivity while having a minimal effect on yaw (γ) sensitivity [57]. A three-hole probe of this design is capable of measuring, in the non-nulling mode, flow angles up to ±35° [58].

The probe was operated in a non-nulling mode for ease of use and to minimise measure-

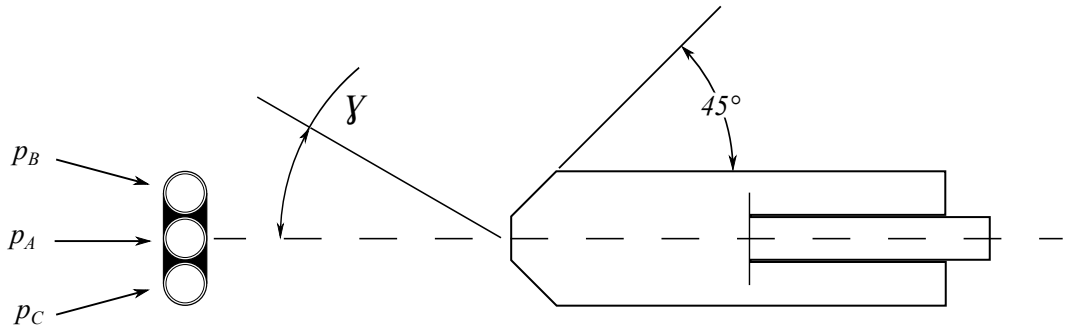

Figure 3.3: Details of the three-hole probe tip design.

ment time. In the non-nulling mode the probe position is fixed, and velocity and incidence angle, γ, are determined from the tube pressures. To accomplish this, calibration curves were constructed for C_α, C_{p_0}, and C_{p_s} based on the method in Ref. [59]. The equations for C_α, C_{p_0}, and C_{p_s} are given in Eqs. 3.1 - 3.3; as specified in Ref. [60].

$$C_\alpha = \frac{p_B - p_C}{p_A - 0.5\,(p_B + p_C)} \tag{3.1}$$

$$C_{p_0} = \frac{p_0 - p_A}{p_A - 0.5\,(p_B + p_C)} \tag{3.2}$$

$$C_{p_s} = \frac{p_0 - p_s}{p_A - 0.5\,(p_B + p_C)} \tag{3.3}$$

Numerical interpolation was employed for measurements which fell between calibration points instead of creating mathematical curve fits, since the introduced error has been shown to be lower for the former technique [60]. The calibration was conducted upstream of the model mount, in the empty test section. The three-hole probe was pivoted though 48° while the pressures of the three tubes were measured. At the same time, pressure measurements were taken from a stationary pitot-static probe located 15 mm to the left of the three-hole probe. These five measurements were then used to construct calibration curves for the probe. Typical calibration curves have been included in Appendix C.

The three-hole probe pressure profiles were measured at the same time as the pitot-static and hot-wire profiles. The three-hole probe was mounted in-plane with the other probes 10 mm below the pitot-static tube and 20 mm below the cross-wire. The tip of the central probe was aligned with the total pressure port of the pitot-static probe. The tips of the three probes were within 0.5 mm in the streamwise direction.

3.6 Control Volume Drag Formulation

To obtain a reliable experimental methodology for measuring drag, it is necessary to develop a theoretical formulation with experimentally obtainable variables. In order for the method to be widely applicable, it is necessary to create a detailed list of the restrictions

of the method and estimate the associated uncertainty in drag. Recording the simplifying assumptions applied in generating the drag formulation is necessary to achieve this. The conservation of linear momentum applied to a control volume in a continuous fluid is given by Eq. 2.1. For the applications of interest, the Mach number is much less than 0.3, allowing the fluid to be treated as incompressible, and, since the focus is on mean drag force the flow can be considered steady. Equation 3.4 is the expression for conservation of linear momentum applied to a fixed control volume in an incompressible, steady flow. The sum of the forces acting on the control volume has been expanded on the left hand side, neglecting external forces.

$$-\vec{F_B} + \iint_S -p\vec{n}\,\mathrm{d}S + \iint_S \tau : \vec{n}\,\mathrm{d}S = \iint_S \rho\vec{V}(\vec{V}\cdot\vec{n})\,\mathrm{d}S \tag{3.4}$$

The current study is restrained to nominally two-dimensional flows, and the focus is on drag, i.e., the component of $\vec{F_B}$ projected on the x axis. The area integrals can then be reduced. Drag, D, per unit width, b, is given by:

$$\frac{D}{b} = \underbrace{-\int_l \rho\vec{V}(\vec{V}\cdot\vec{n})\,\mathrm{d}l}_{\text{Term I}} + \underbrace{\int_l \tau : \vec{n}\,\mathrm{d}l}_{\text{Term II}} + \underbrace{\int_l -p\vec{n}\,\mathrm{d}l}_{\text{Term III}} \tag{3.5}$$

To evaluate the drag formulation presented in Eq. 3.5, it would be necessary to measure velocity, viscous stresses, and pressure distributions along the entire contour, l. The region of measurement can be reduced, and probe positioning simplified, by a careful manipulation of the control volume contour. A four sided control volume, depicted in Fig. 3.4 allows each term to be evaluated in only three different regions. If boundaries 2 and 3 are placed on streamlines, the mass flux is constrained to boundaries 1 and 4. If boundary 1 is placed sufficiently far upstream, the velocity distribution along it will be uniform (U_1) and a single point measurement will define the momentum flux. Term I in Eq. 3.5 will simplify to the following:

$$\text{Term I} = -\rho\int_{l_1} U_1^2\,\mathrm{d}y + \rho\int_{l_4} U^2\,\mathrm{d}y \tag{3.6}$$

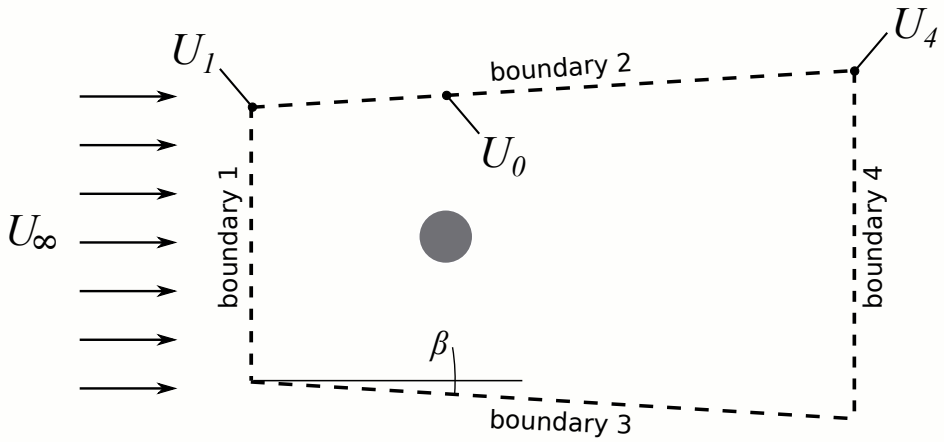

Figure 3.4: Four sided control volume with streamwise measurement locations of outer flow velocities noted.

Assuming that turbulent flow is limited to the wake region and vertical velocity gradients in the outer flow of the test section are negligible, the viscous stresses along boundaries 1, 2, and 3 are negligible. Therefore, it is only necessary to account for the viscous stresses along boundary 4; however, viscous stresses cannot be measured directly and are difficult to estimate. The only component of viscous stress which contributes to the drag is τ_{xx}, which is given by

$$\tau_{xx} = \mu \left(2\frac{\partial U}{\partial x} - \frac{2}{3}\nabla \cdot \vec{V} \right) + R_{xx} \tag{3.7}$$

from Ref. [31], where R_{xx} is the Reynolds stress term shown expanded in Eq. 3.8.

$$R_{xx} = -\rho u'^2 - 2U\rho' u' - \rho' u'^2 \tag{3.8}$$

where u' is the streamwise RMS velocity component and ρ' the RMS component of density. In an incompressible flow Eqs. 3.7 and 3.8 can be combined and simplified to the following expression:

$$\tau_{xx} = 2\mu\frac{\partial U}{\partial x} - \rho u'^2 \tag{3.9}$$

The viscous component is generally much smaller than the Reynolds stress term and, therefore, can be neglected [5]. Term II, from Eq. 3.5, will reduce to the following formula.

$$\text{Term II} = -\rho \int_{l_4} u'^2 \, \mathrm{d}y \tag{3.10}$$

While pressure can be measured experimentally, it is advantageous if the pressure distribution can be determined from velocity measurements. The experimental measurements can then be accomplished with a single measurement technique, such as hot-wire anemometry. For the purposes of drag calculations, two different pressure variations were considered: the pressure drop between boundaries 1 and 4 due to blockage effects, and the pressure variation in the wake.

Since boundaries 2 and 3 are located on streamlines in the outer flow, the change in pressure along this boundary can be predicted from Bernoulli's equation. The streamwise pressure variation in the outer flow makes it necessary to account for the pressure contribution to drag on all four control volume surfaces. Assuming that boundaries 2 and 3 can be approximated as straight lines at an angle β from horizontal, the contribution from pressure acting on these boundaries shall be proportional to $\sin\beta$. When β is small, the contribution from streamwise pressure variation along boundaries 2 and 3 is negligible and the pressure along these boundaries can be approximated as equal to that acting on boundary 1.

The pressure along boundary 4 can vary substantially in the wake region. This pressure variation can be approximated through the Reynolds averaged Navier-Stokes equation [43]. In addition to the flow being steady and two-dimensional the following must be valid: (i) zero mean vertical velocity, (ii) negligible change in vertical velocity with y, and (iii) negligible changes in the velocity field with streamwise distance. The resulting relationship between average pressure and the velocity field is given by

$$\frac{\partial p}{\partial y} = -\rho \frac{\partial v'^2}{\partial y} \tag{3.11}$$

where v' is the vertical RMS velocity. The restrictions to the applicability of Eq. 3.11

suggest that this relationship may only be valid sufficiently far downstream. When the pressure variation along boundary 4 is combined with the streamwise pressure drop, Term III takes the following form:

$$\text{Term III} = -\int_{l_4} \left[\frac{1}{2} \left(U_1^2 - U_4^2 \right) - \rho v'^2 \right] \, \mathrm{d}y \tag{3.12}$$

The resulting expression for drag coefficient per unit span is given in Eq. 3.13 for a body with a characteristic length L.

$$c_d = \frac{2}{U_0^2} \left\{ \underbrace{\int_{\frac{l_1}{L}} U^2 \, \mathrm{d}\left(\frac{y}{L}\right) - \int_{\frac{l_4}{L}} U^2 \, \mathrm{d}\left(\frac{y}{L}\right)}_{\text{Term I}} - \underbrace{\int_{\frac{l_4}{L}} u'^2 \, \mathrm{d}\left(\frac{y}{L}\right)}_{\text{Term II}} - \underbrace{\int_{\frac{l_4}{L}} \left[\frac{1}{2} \left(U_1^2 - U_4^2 \right) - \rho v'^2 \right] \, \mathrm{d}\left(\frac{y}{L}\right)}_{\text{Term III}} \right\} \tag{3.13}$$

where U_0 is the outer flow velocity at the model location, indicated in Fig. 3.4. To summarize, Eq. 3.13 is valid for an incompressible, two-dimensional, steady flow and when the following conditions are satisfied at the control volume boundaries: (i) uniform flow along boundary 1, (ii) negligible velocity gradients along the streamlines which form boundaries 2 and 3, (iii) negligible streamwise changes in the velocity field at the location of boundary 4, and (iv) there is no vertical component of velocity along boundary 4.

Chapter 4

Wake Development

4.1 Cylinder Wake

This section contains experimental flow field and model surface measurements for a circular cylinder operating at a Reynolds number (Re_d) of $8,000$.

4.1.1 Test Section Pressure Distribution

The static pressure distribution along the test section walls, set in the ASW configuration, is presented in Fig. 4.1 for the empty test section and with a circular cylinder installed at $X/d = 0$. Due to symmetry and for clarity, only roof measurements are shown. Assuming there is no vertical pressure gradient in the boundary layer, wall pressure distributions are equivalent to the pressure distribution along a streamline in the outer flow of the test section. The surface pressure coefficients in the empty test section show a nearly constant distribution, as is expected in the test section with the walls in the ASW configuration. This confirms the velocity is constant along the length of the test section. The effect of the cylinder model, on the outer flow, is illustrated by comparing the two pressure distributions in Fig. 4.1. The variation with streamwise position in the wall pressure coefficients is due to solid and wake blockage, and the physical flow behaviour. The solid blockage due to the cylinder model and end plates is approximately 2.8%. Based on the solid blockage ratio

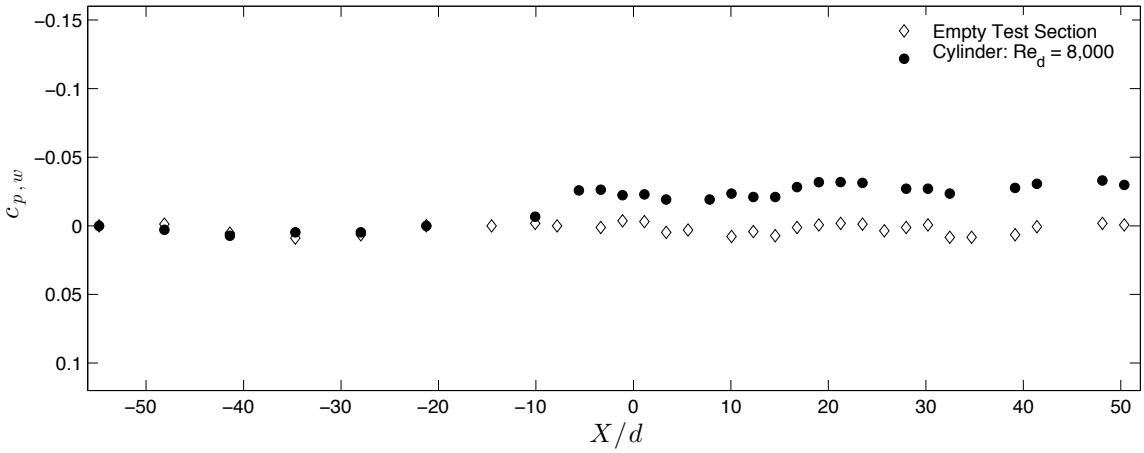

Figure 4.1: Wall pressure distribution along the roof of the test section, when set in the ASW configuration while empty and with a circular cylinder installed. Uncertainty in the measured coefficients of wall pressure is estimated to be less than 3.0% of the freestream dynamic pressure.

and the findings of a wall streamlining study, conducted by Bishop [49], the primary cause of the variation in the outer flow velocity is due to blockage. Blockage effects in the outer flow are first apparent at approximately $X/d = -10$. The largest streamwise variation in measured pressure coefficient occurs over $-15 < X/d < 0$, the region immediately upstream of the model.

Velocity variation along the outer flow streamline can be determined from the definition of $c_{p,w}$. The expression for velocity variation in the outer flow is

$$\frac{U}{U_1} = \sqrt{1 - c_{p,w}} \tag{4.1}$$

where U_1 is the velocity at boundary 1 of the control volume, located at $X/d = -55$. Since the wall pressure coefficients were measured with respect to the wall tap at boundary 1, the streamwise variation is calculated in relation to the freestream velocity at boundary 1. Therefore, Fig. 4.2 depicts the variation in outer flow with respect to U_1. This is important to control volume drag analysis since the difference between the velocity at boundary 1

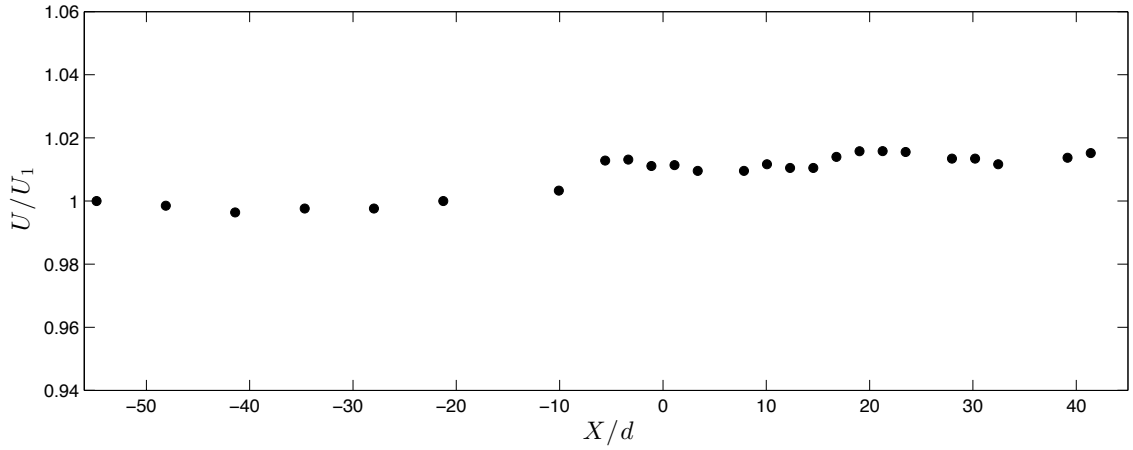

Figure 4.2: Streamwise variation in the outer flow velocity around the circular cylinder.

(U_1) and at boundary 4 is necessary for drag calculations (see Eq. 3.13). In addition, in two of the drag formulations investigated during this study there exists some ambiguity as to the appropriate location to measure freestream properties. The data contained in Figs. 4.1 and 4.2, permits the change, in drag coefficients due to reference location selected, to be quantified. The greatest change in the outer flow velocity occurs at $X/d < -3$, upstream of the wake profile measurements. The outer flow is between 1% and 2% higher at the downstream wake profile locations investigated in this study, $3 \geq X/d \geq 40$, than at the control volume inlet. Therefore, U_4 varies by approximately 1% of U_1 over the streamwise region of interest, i.e. location of wake profile measurements. The effect this will have on drag estimates is unknown.

4.1.2 Surface Pressure Distribution

The surface pressure distribution on the cylinder is shown in Fig. 4.3 along with results from three previous studies. The Reynolds numbers of the reference data are close to 8,000, the exact values are given in Table 4.1. The results from the current study show good agreement with the three reference profiles, with minor variations attributed to differences in the L_m/d ratios and experimental conditions. The pressure drag coefficient ($c_{d,p}$) for the

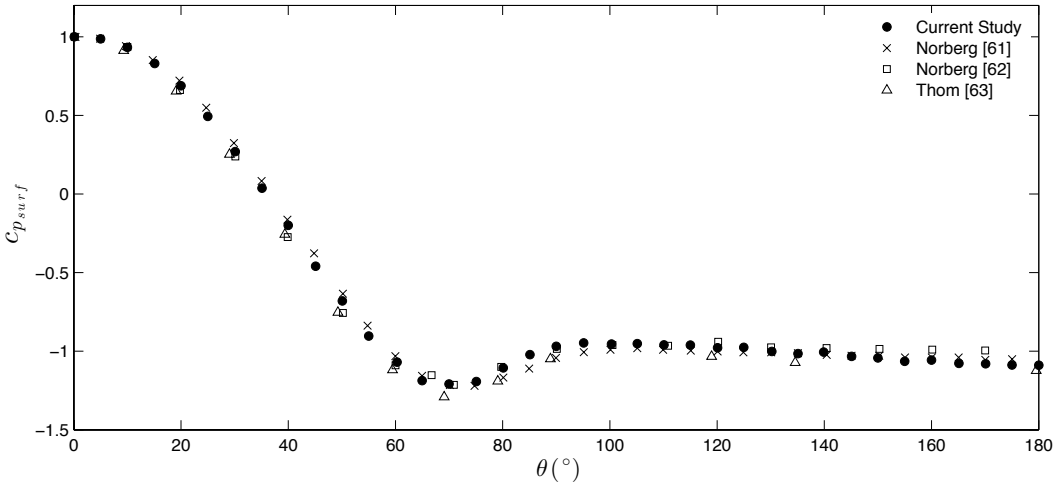

Figure 4.3: The measured cylinder surface pressure coefficient distribution shown with reference to profiles from the work of Norberg [61, 62] and Thom [63].

circular cylinder was calculated by integrating the surface pressure distribution, shown in Fig. 4.3, as

$$c_{d,p} = \int_0^\pi c_{p_{surf}}(\theta) \cos\theta \, \mathrm{d}\theta \tag{4.2}$$

where $c_{p_{surf}}(\theta)$ is the pressure coefficient measured on the surface of the cylinder at θ. Due to symmetry, the integration is only performed over the upper half of the cylinder. The distribution was integrated numerically using the trapezoidal rule. The resulting pressure drag coefficient is 1.22 with an estimated uncertainty of about 5%. Although the estimate is higher than most of those listed in Table 4.1, it falls well within the range of experimental values reported for $Re_d = 8,000$ in other studies [33, 64, 65]. The difference in drag coefficients is probably due to differences in the L_m/d and blockage ratios of the individual experiments. The measured $c_{d,p}$ will later be used for comparison with momentum integral based drag estimates.

Table 4.1: Drag coefficient and Reynolds number of the cylinder data references.

Experiment	Re_d	c_d
Current study	$8,000$	1.22
Norberg [61]	$8,020$	1.14
Norberg [62]	$8,000$	1.05
Thom [63]	$8,500$	1.08
Cantwell and Coles [64]	$8,000$	0.9 - 1.23

4.1.3 Wake Velocity Measurements

The mean and RMS wake velocity profiles measured downstream of the circular cylinder are presented in Figs. 4.4 - 4.7. The profiles were measured at intervals from $X/d = 3$, which is just outside the recirculation region [27], to $X/d = 40$, the maximum extent of measurement. All wake profiles have been normalized by the edge velocity at the corresponding measurement location, i.e., in terms of control volume notation, the normalization velocity is U_4 (see Fig. 4.2).

The streamwise velocity profiles show characteristic wake development for a circular cylinder. As the downstream distance increases, the wake width grows and the maximum streamwise velocity deficit decreases along with the magnitude of velocity fluctuations. The streamwise RMS profiles measured prior to $X/d = 10$ downstream show the double peak typical of cylinders [66], while the vertical RMS profiles have a single peak as expected [66]. The two peaks present in the streamwise RMS profiles are not symmetric, however the difference between the maximum of each peak is less than 1% of the freestream velocity, which is less than the experimental uncertainty.

The mean vertical velocity profiles, Fig. 4.6, are characteristically asymmetric [66]. The vertical component of velocity is relatively small, 5% of the wake edge velocity at the maximum location, and decays rapidly with increasing X/d. These are lower relative values of vertical velocity than those reported in Ref. [66] for $Re_d = 3,900$, where at $X/d = 3$ the maximum vertical velocity was approximately 10% of the freestream. Since the Reynolds number and L_m/d ratio are lower for the experimental measurements in Ref. [66], the

formation region is likely to be longer than in the current study [27]. It is expected that fast decaying parameters such as V would be sensitive to the distance from the formation region, therefore, with different formation lengths the magnitude of V would differ at the same X/d location. Regardless, the contribution of vertical velocity in momentum integral drag calculations is negligible. The minor vertical velocity gradient (less than 1% of U_4 over the vertical span of the wake profile) apparent outside the wake region also appears in empty test section profiles.

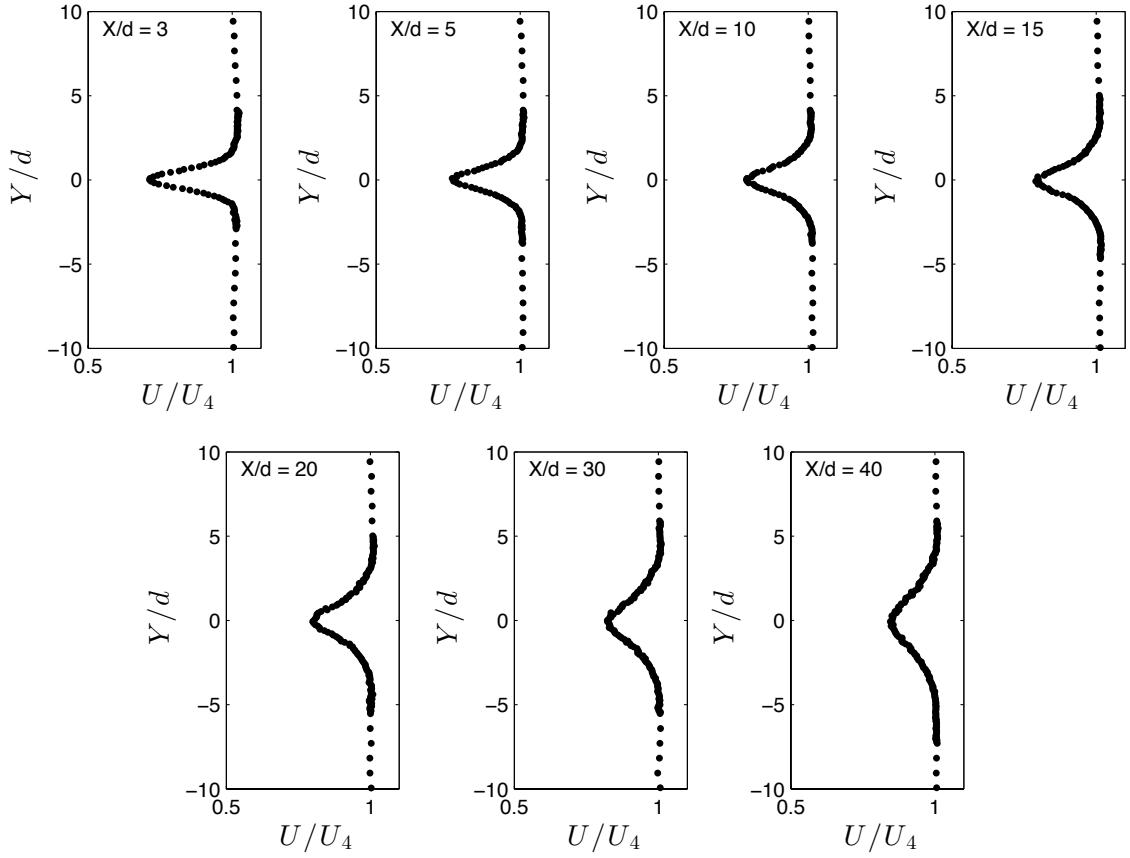

Figure 4.4: Mean streamwise velocity wake profiles for the circular cylinder.

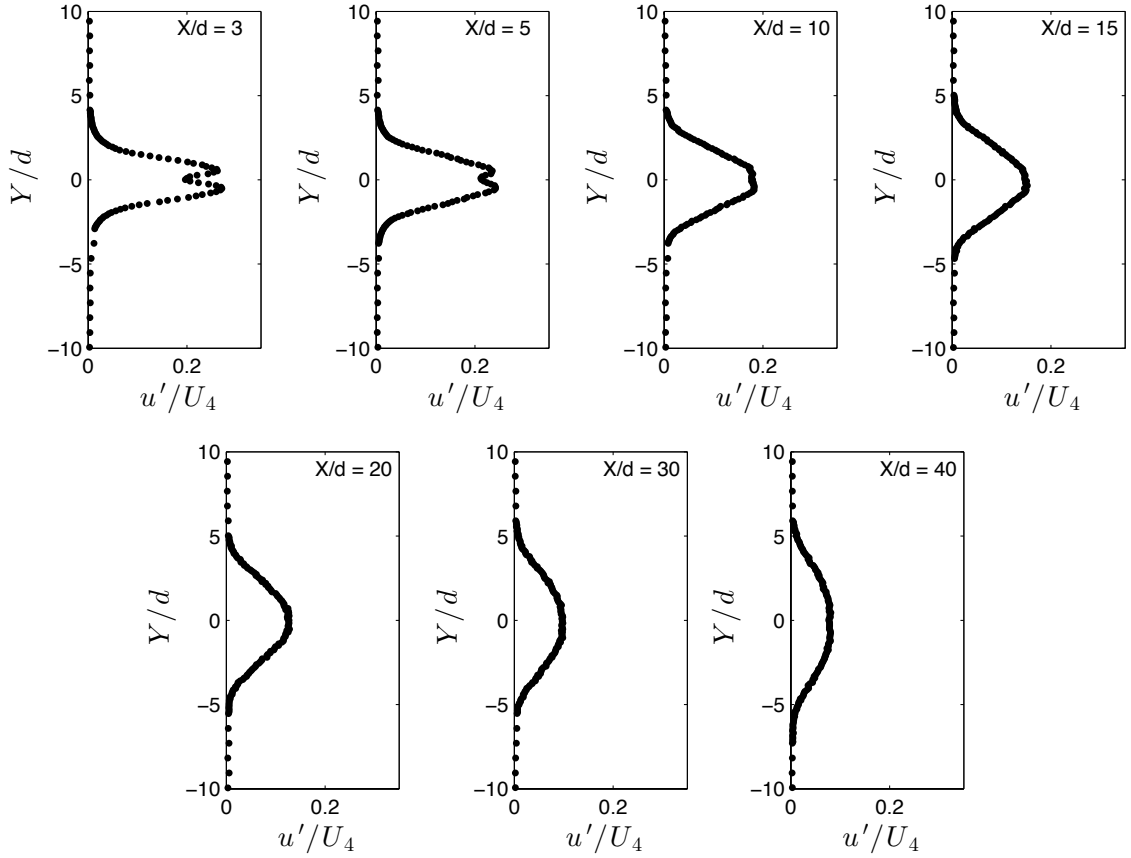

Figure 4.5: Streamwise RMS velocity wake profiles for the circular cylinder.

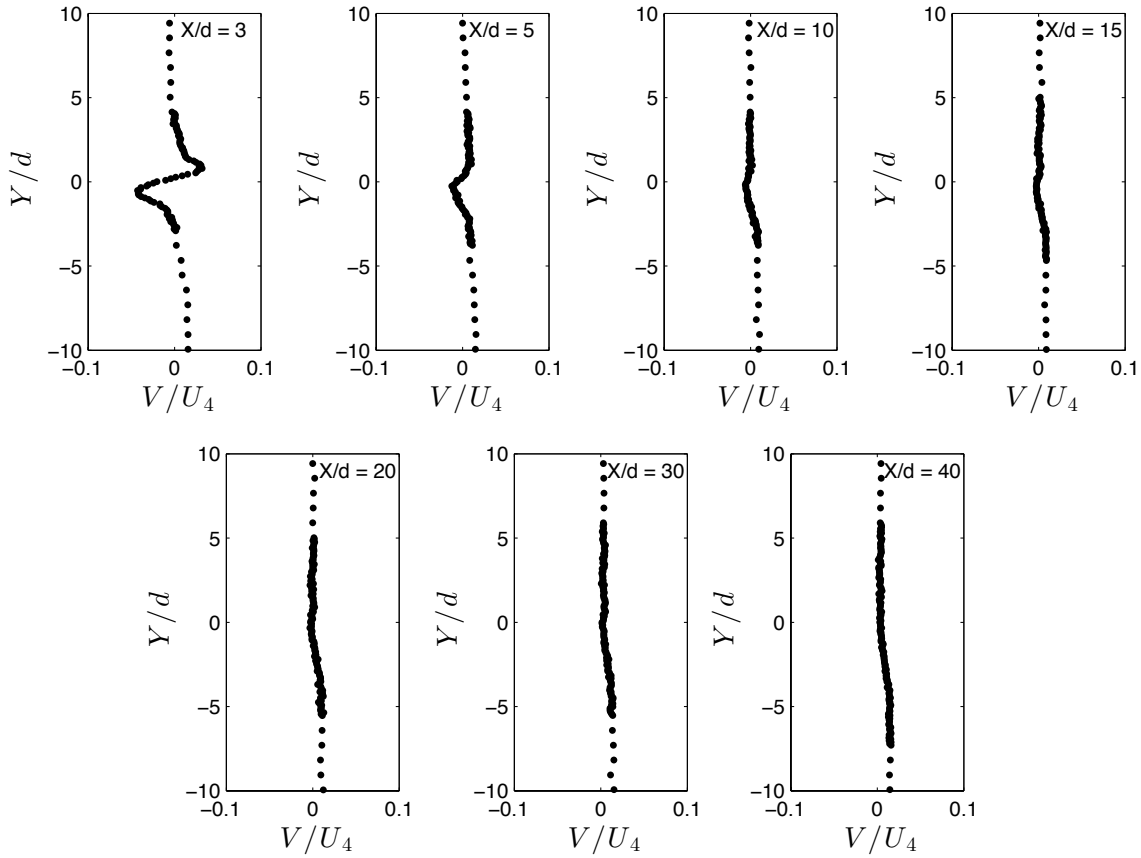

Figure 4.6: Mean vertical velocity wake profiles for the circular cylinder.

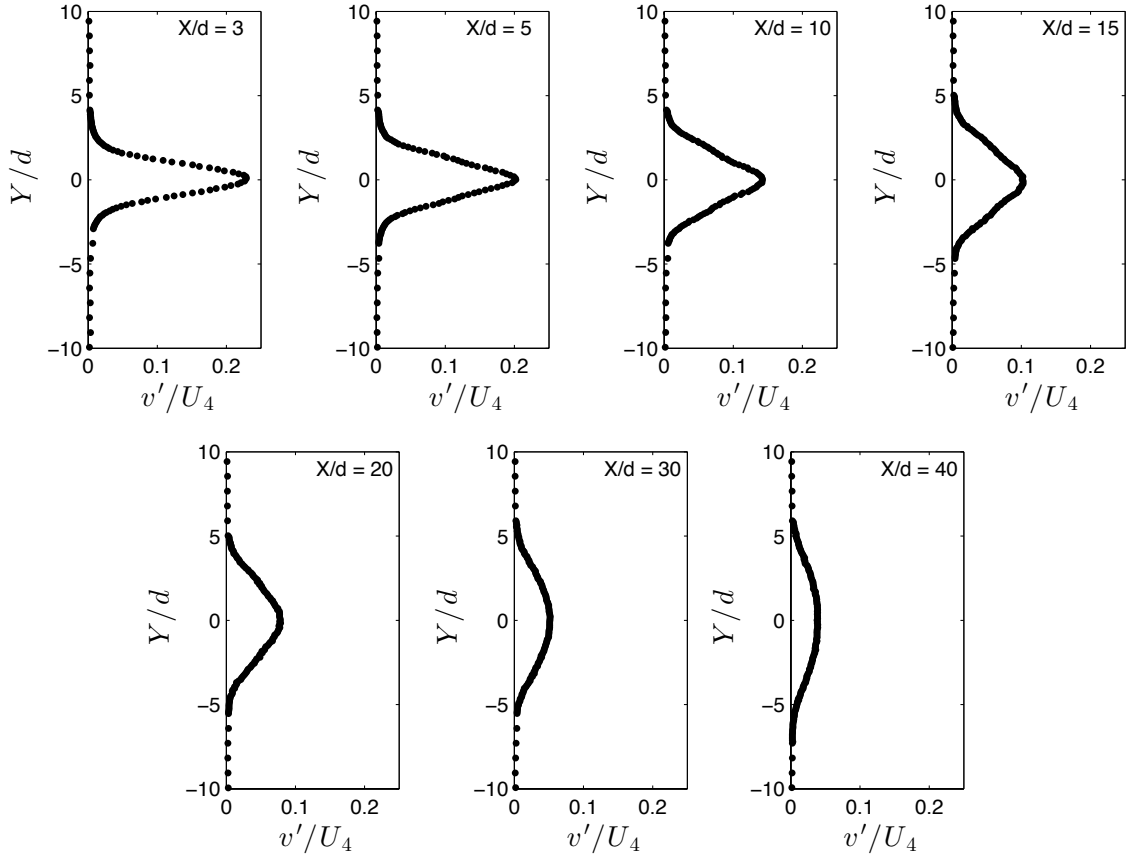

Figure 4.7: Vertical RMS velocity wake profiles for the circular cylinder.

Wake half width (w) is plotted in Fig. 4.8 as a function of streamwise position. To calculate w, the points equivalent to half the maximum velocity deficit were identified on either side of the centreline and the vertical distance between the points was used as the wake half width. This technique was based on the method presented in Ref. [67]. The curve fit included in Fig. 4.8 shows growth proportional to $X^{0.4}$. For comparison, data from Refs. [32] and [68] is shown in Fig. 4.8 for Reynolds numbers of 32,200 and 5,830 respectively. While the total wake widths are different, the rate of wake growth is similar in all three studies. A curve fit to the data indicates wake growth proportional to $X^{0.41}$ in Ref. [32] and $X^{0.44}$ in Ref. [68]. According to Schlichting [69] plane wake growth, in

an unbounded flow, will be proportional to $X^{0.5}$, however lower experimental values are common in the near wake region [70]. In a study by Okamoto and Takeuchi [32], test section blockage was shown to restrict wake growth. Increased blockage has also been seen to diminish wake growth even where solid and wake blockage has been mitigated through wall streamlining [49]. In the current investigation, solid blockage with endplates installed is less than 3%.

The change in maximum velocity deficit with streamwise position is shown in Fig. 4.9. The trend line in Fig. 4.9 is proportional to $X^{-0.2}$. According to Schlichting [31], recovery of the streamwise velocity deficit in a plane, unbounded wake will occur proportionally to $X^{-0.5}$. However, in experimental situations lower rates of centreline velocity recovery are common. For comparison, data on the wake recovery from Refs. [66] and [49] is shown in Fig. 4.9. The investigations were conducted at $Re_d = 3,900$ in Ref. [66] and $Re_d = 57,000$ in Ref. [49]. In Ref. [66] recovery was found to be proportional to $X^{-0.34}$ and in Ref. [49] it was proportional to $X^{-0.26}$.

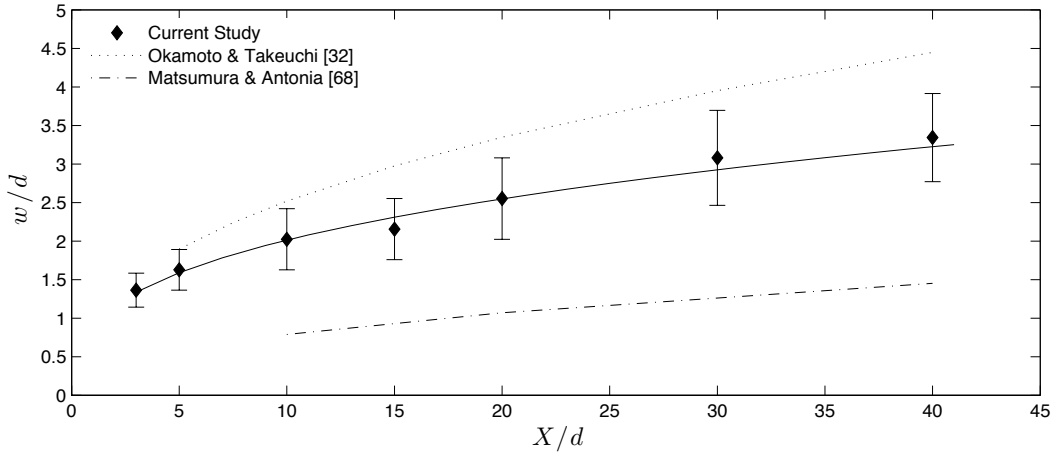

Figure 4.8: Streamwise variation of the wake half width for the circular cylinder.

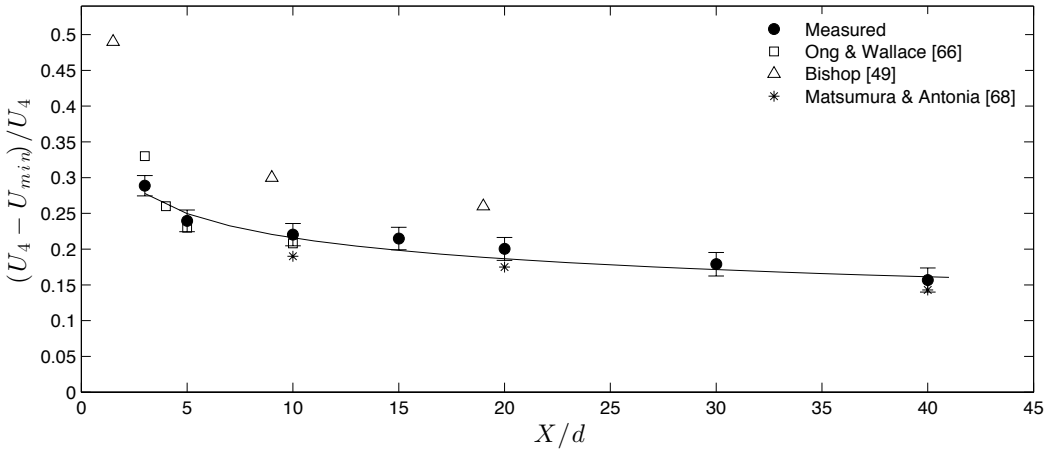

Figure 4.9: Streamwise evolution of the maximum velocity deficit in the wake of the circular cylinder.

The decay of the maximum streamwise and vertical RMS velocity fluctuations is shown in Fig. 4.10. For each wake location surveyed, the maximum streamwise fluctuations are greater than the maximum vertical fluctuations by approximately 5% of U_4. The reference data set from Ref. [66] indicates that the reverse trend is true in the wake of a circular cylinder. This is confirmed by the wake profiles presented in Ref. [71] measured between $X/d = 91$ and 725 in the wake of a circular cylinder operating at Reynolds numbers of 100 to $7,000$. This finding, when coupled with the lower vertical velocities noted in Fig. 4.6 and the agreement of the streamwise characteristics in Figs. 4.8 and 4.9, suggests that the vertical component of velocity is under-predicted by the current method used for calculating velocity components from the cross-wire data. This will effect drag estimates since in certain drag formulations the pressure variation in the wake is predicted from the vertical velocity fluctuations (Eq. 3.11). The effect the under estimation may have on drag values will be explored further when examining drag calculations. The vertical position of the maximum streamwise and vertical fluctuations observed in the current study matches observations from Refs. [66] and [71]. The RMS profiles (Figs. 4.5 and 4.7) show that the maximum vertical fluctuations occur along the wake centreline, whereas the maximum streamwise fluctuations occur away from the centreline at the double peaks until $X/d = 20$.

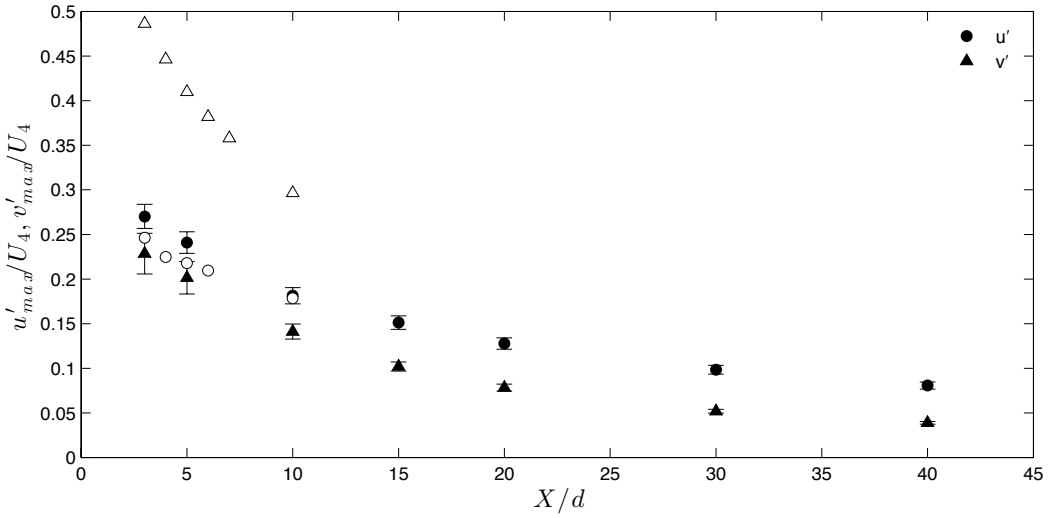

Figure 4.10: Decay of maximum streamwise and vertical RMS velocity components. Hollow symbols indicate fluctuations measured in the wake of a circular cylinder operating at $Re_d = 5,600$ from Ref. [66].

The mean and RMS profiles are shown normalized by wake half width in Fig. 4.11. This summative plot illustrates the streamwise wake development. The greatest rate of change occurs prior to $X/d = 10$, for all four parameters. The streamwise velocity (Fig. 4.11a) decreases with increasing streamwise position, however, the profile shape remains similar. The double peaks seen in the streamwise RMS profiles (Fig. 4.11b) become less distinct as the profile develops and merge into a single peak by $X/d = 20$. With the overlay of the profiles the minor gradient in the mean vertical velocity profiles (Fig. 4.11c) remains approximately constant with streamwise position. Overall, with the magnitude of vertical velocity components being the sole exception, the wake velocity profiles display wake characteristics that fall within the range of values observed in comparable studies.

4.1.4 Wake Pressure Measurements

Wake pressure profiles were measured relative to the wall pressure tap located at boundary 1. The resulting total pressure profiles, measured with a pitot-static tube and three-hole

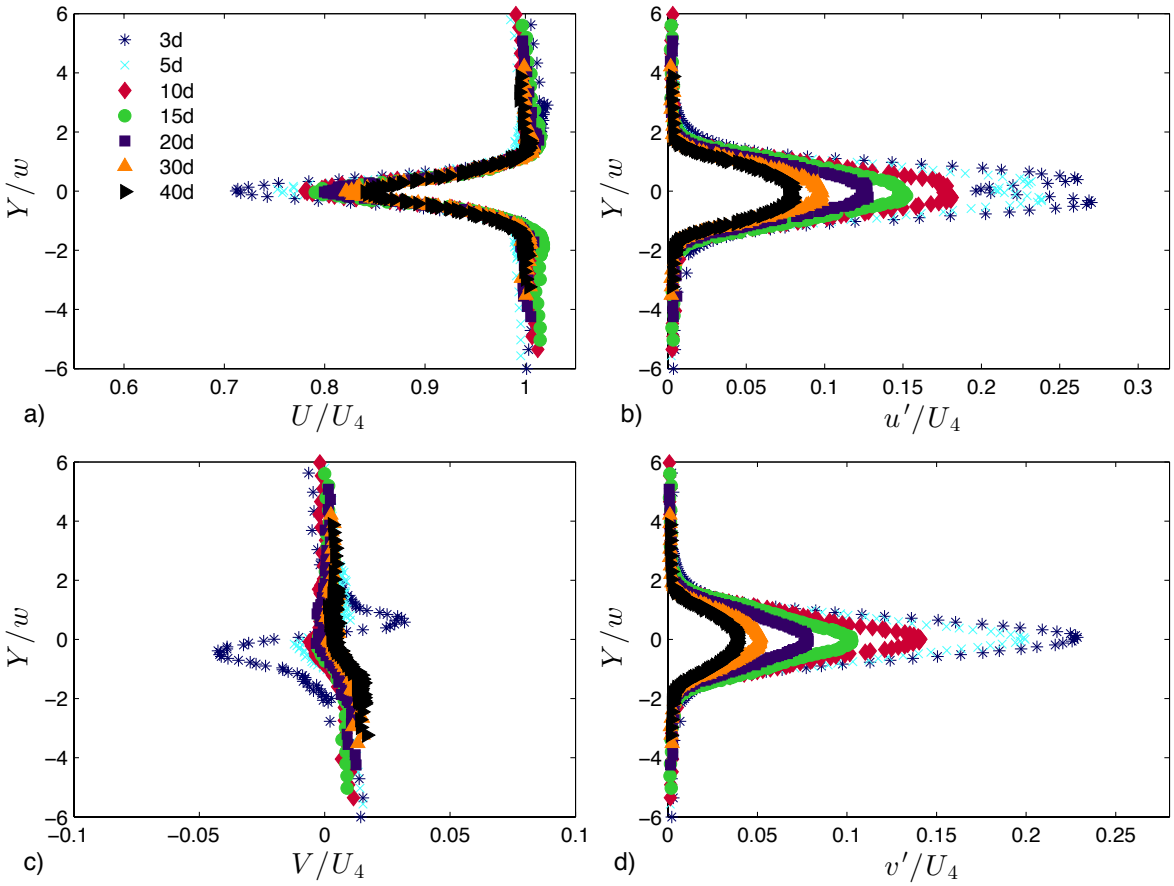

Figure 4.11: Normalized velocity profiles scaled by wake half width.

probe, are shown in Fig. 4.12. The data are normalized by the total pressure measured in the outer flow at each streamwise measurement location, i.e. p_4. Both measurement techniques show good agreement in measured total pressure over the entire length of the profiles at all wake locations surveyed. The results show that total pressure variation across the wake decreases with increasing distance from the cylinder, as expected.

Wake static pressure profiles, normalized by p_4, are presented in Fig. 4.13. The static pressure profiles measured by the pitot-static tube and three-hole probe differ for profiles measured up to $X/d = 20$. The three-hole probe profiles indicate a smaller pressure drop

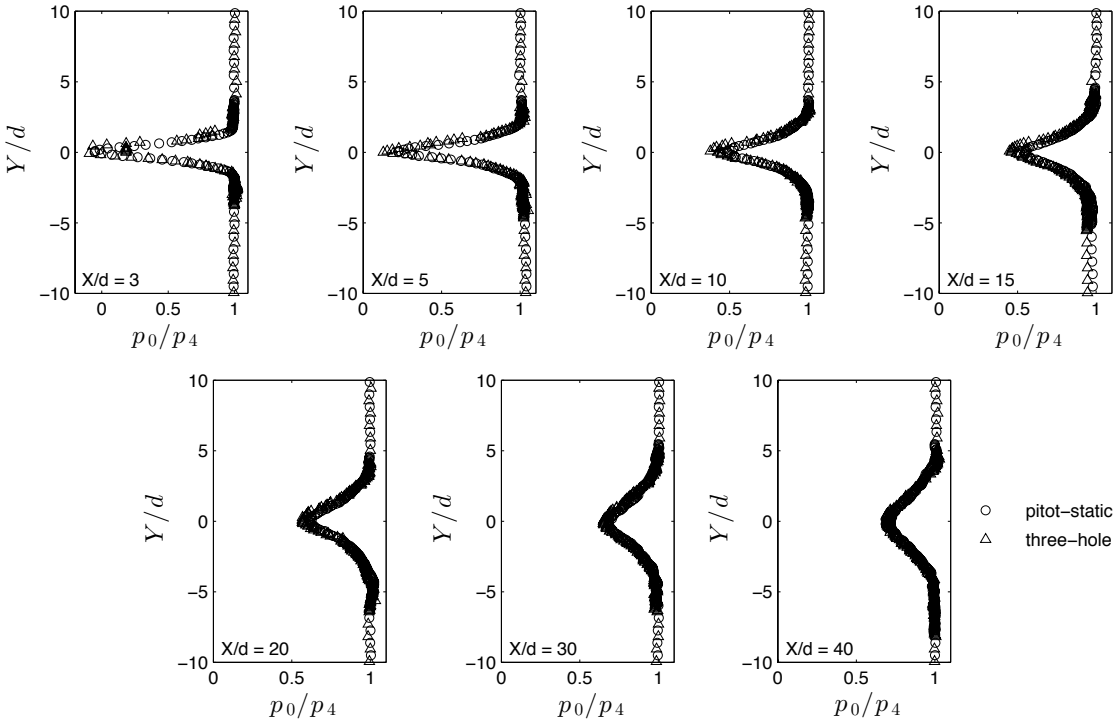

Figure 4.12: Normalized total pressure profiles measured with the pitot-static tube and the three hole probe.

across the wake than the pitot-static tube profiles. To compare the pressure measurements and cross-wire measurements, streamwise velocity profiles have been calculated, shown in Fig. 4.14. Calculations were based on the streamwise velocity components for the cross-wire data, the dynamic pressure for the pitot-static tube measurements, and the dynamic pressure and flow angle for three-hole probe data. With the exception of measurements taken at $X/d = 3$, the velocities based on pitot-static data agree well with those based on cross-wire measurements. The three-hole probe measurements deviate from the pitot-static and cross-wire measurements for profiles measured up to $X/d = 20$. Flow angularity is an important factor in the accuracy of all three measurements. However, the maximum flow angle is less than 5° from horizontal, well within the acceptable range for the pitot-static tube [57] and the three-hole probe calibration limits. Furthermore, the maximum

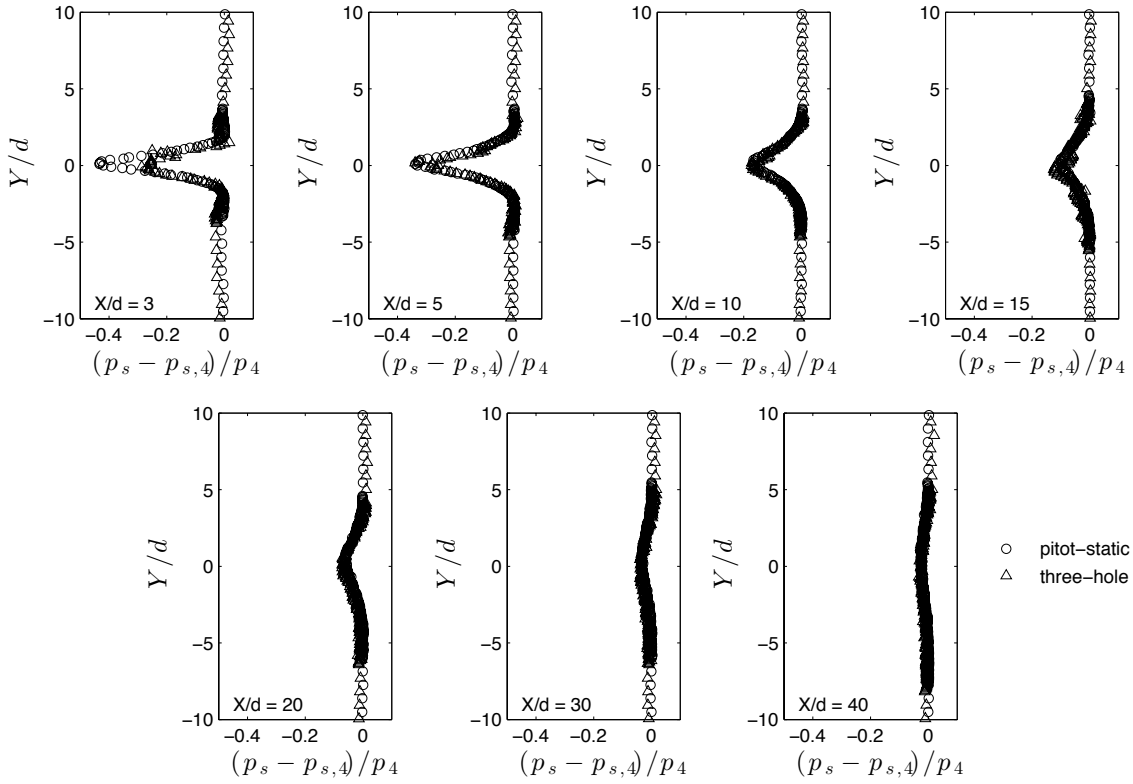

Figure 4.13: Static pressure variation in the wake profiles measured via the pitot-static tube and the three hole probe.

flow angle occurs away from the centreline while the maximum discrepancies occur at the centreline. Therefore, flow angle is not the cause of the observed discrepancy between measurement techniques.

Since measurements are being conducted in the presence of vertical pressure and velocity gradients, the spatial resolution of the probes is an important factor. Of the three measurement probes employed, the cross-wire has the smallest vertical span, approximately 1.25 mm. Therefore, the cross-wire measurements will be least affected by the gradients in the flow. The pitot-static tube and three-hole probe have similar vertical spans, the pitot-static tube is 3 mm in diameter and the three-hole probe is 3.5 mm tall. However, measurements from each will be affected differently by the presence of a pressure gradient.

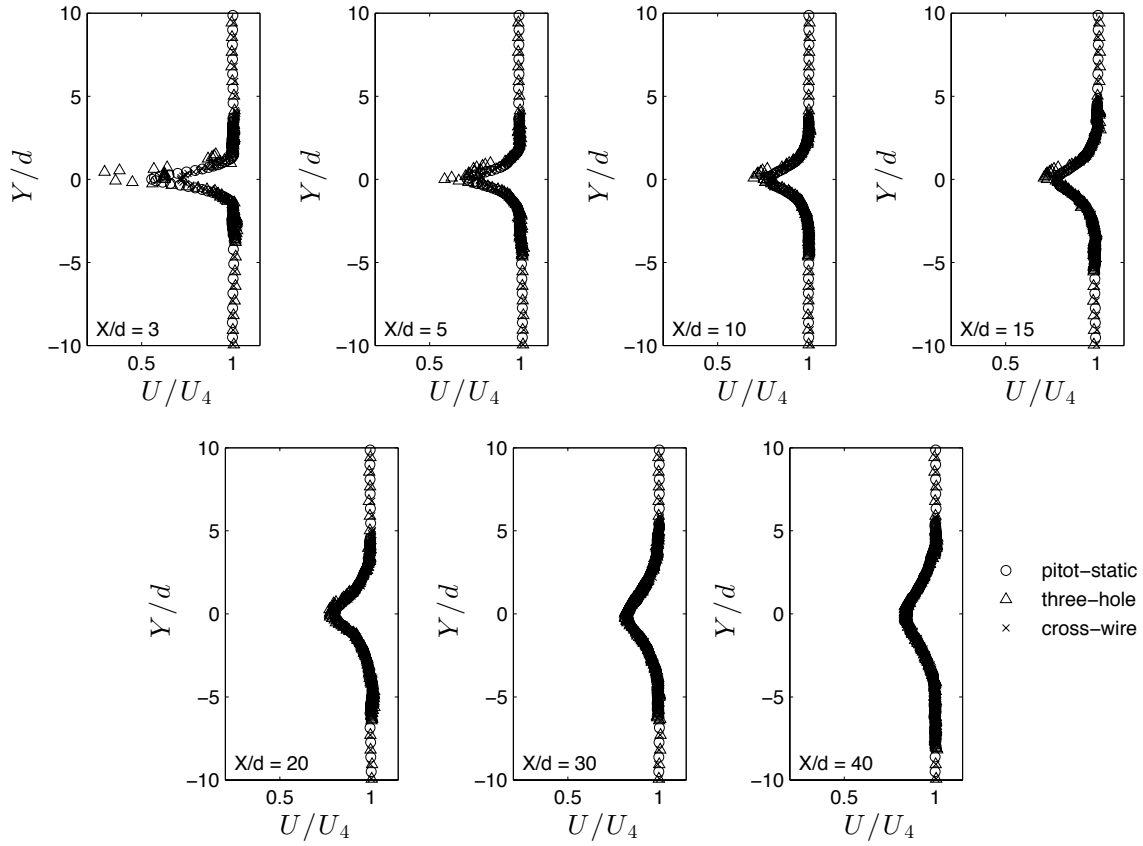

Figure 4.14: Comparison of calculated streamwise velocity profiles based on pitot-static tube, three hole probe, and cross-wire measurements.

With a pitot-static tube, the measured static pressure is averaged over the vertical span of the probe, thus moderating the effect of the static pressure gradient. The three-hole probe relies on three independent pressure measurements each taken approximately 1 mm vertically apart. To determine the sensitivity of the calculated total and static pressure of the three-hole probe, the magnitude of the vertical pressure gradient was determined from the pressure profiles measured at each streamwise location. The effect of the measured pressure gradients was then quantified by perturbing the inputs of the total and static pressure equations (Eqs. 3.2 and 3.3) by the measured gradients. The resulting total and

static pressures were compared to the pressures that would have been calculated without the presence of a pressure gradient. Three types of prescribed pressure gradients were applied, in the calculations, to estimate the introduced error, specifically, a constant positive gradient, a constant negative gradient, and a variable pressure gradient. The magnitudes of the constant gradients were based on the measured pressure gradients above and below the centreline and the variable pressure gradient was based on the magnitudes measured near the centreline. The error in the calculated static pressure is estimated to be between 5 and 40% at $X/d = 3$, and between 1 - 15% at $X/d = 20$. The static pressure was discovered to be most sensitive in the presence of a non-constant pressure gradient, which exists around the centreline. Since the experimental error is significant for profiles measured between $X/d = 3$ and 20, pressure profiles measured with the three-hole probe will not be used for drag calculations in the next section.

As noted previously, the three velocity profiles at $X/d = 3$, shown in Fig. 4.14, are not in agreement. While it is expected that the three-hole probe measurements will diverge from those of the pitot-static tube around the centreline, the divergence of the pitot-static tube and the cross-wire measurements is unexpected. The profile at $X/d = 3$ is just outside the recirculation zone which may lead to increased experimental error. That, coupled with the steep gradients means that the measurements at this location will be excluded from pressure based calculations and treated with care in the hot-wire based calculations. The agreement between the pitot-static based and the cross-wire based measurements for profiles at $X/d > 3$ is excellent. There is less than 5% maximum error along the wake profile, which is within the estimated experimental uncertainty. These measurements confirm the accuracy of the streamwise cross-wire measurements.

Pressure recovery in the wake is summarized in Figs. 4.15 and 4.16, showing variation of minimum total pressure and maximum static pressure deficit with X/d, respectively. Data from Ref. [42], pertaining to $Re_d = 40,000$, is also shown for comparison. Figure 4.15 shows that a similar total pressure recovery is observed in the two experimental data sets. Fig. 4.16 illustrates the static pressure recovers sooner in the wake of the airfoil at $Re_d = 40,000$ than in the current study. However, in both data sets the maximum static

pressure deficit recovers rapidly in the near wake and then the streamwise recovery slows significantly, in the current study pressure recovery slows after $X/d = 20$.

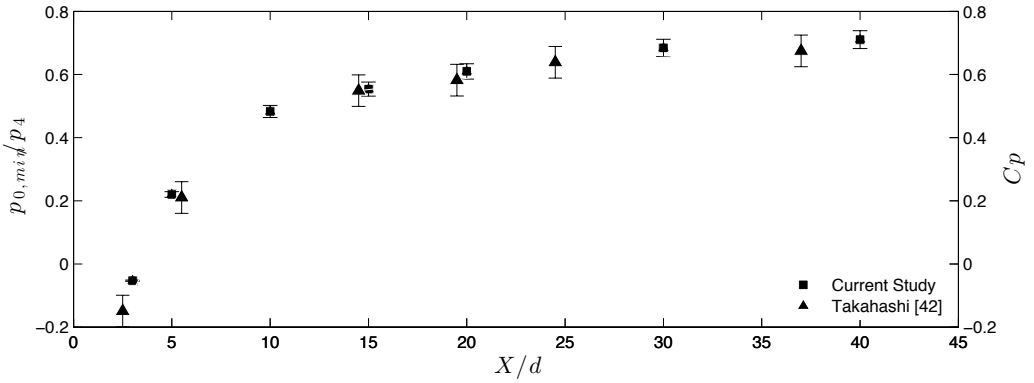

Figure 4.15: Streamwise change of centreline total pressure in the wake of a circular cylinder. The error bars on data points from Ref. [42] represent the uncertainty in value due to the scale of the source data plots, while the error bars on the data from the current study are based on experimental and calculation uncertainty

.

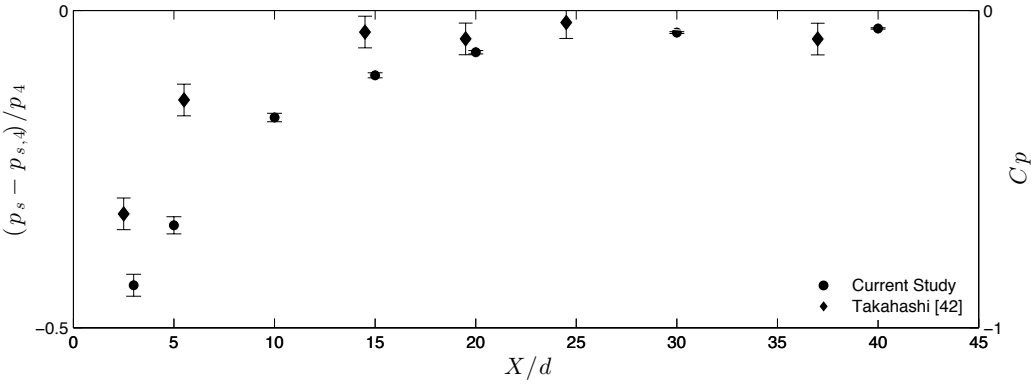

Figure 4.16: Recovery of maximum static pressure deficit in the wake of the circular cylinder. The error bars shown for the Ref. [42] data represent the uncertainty in value due to the scale of the source data plots, whereas the error bars for the current study are based on experimental and calculation uncertainty

4.2 Airfoil Wake

This section details the wake development behind, and surface pressure distribution over, a NACA 0018 airfoil operating at a chord Reynolds (Re_c) number of $100,000$. Measurements were taken at four angles of attack (α), namely, 0°, 5°, 10°, and 15°. These experimental conditions permit the two flow regimes common to low Reynolds number airfoil operation to be investigated: i) at $\alpha = 0°$, 5°, and 10°, a separation bubble forms over the airfoil, and ii) flow separates without subsequent reattachment at $\alpha = 15°$. The results are similar for 0°, 5°, and 10°, so for brevity only a single angle is presented here, $\alpha = 10°$. The results for 0° and 5° are included in Appendix D.

4.2.1 Test Section Pressure Distribution

The pressure coefficients measured along the test section walls set in the ASW configuration are shown in Fig. 4.17 for all angles of attack investigated. Note, only the roof pressure

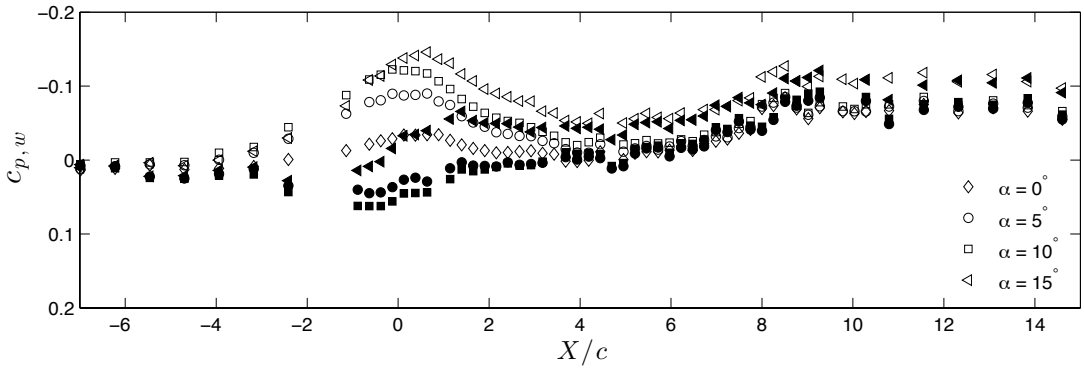

Figure 4.17: Roof (hollow) and floor (solid) pressure distributions, with the NACA 0018 airfoil installed in the test section set in the ASW configuration and operating at $Re_c = 100,000$.

coefficients are shown for $\alpha = 0°$ due to symmetry and for clarity. The wall pressure distributions for $\alpha = 5°$, 10°, and 15° show the asymmetry introduced into the outer flow as a result of the non-symmetric model setup. The outer flow asymmetry is first discernible

roughly $X/c = -3$ from the airfoil axis and extends downstream to approximately $X/c = 4$. The pressure in the outer flow of the far wake is similar for $\alpha = 0°$, $5°$, and $10°$, where a separation bubble forms on the surface of the airfoil, and the pressure is lower in the far wake for $\alpha = 15°$, where the flow separates without reattachment. Separated flow leads to a wider wake, higher wake blockage, and a greater pressure drop along the test section.

The variation in the velocity of the outer flow, with respect to the velocity at boundary 1 (U_1), is shown in Fig. 4.18, where boundary 1 is located at $X/c \approx -6.25$. The variation in velocity was calculated from Eq. 4.1, based on the wall pressure distributions. The outer flow over the upper surface of the airfoil is faster than over the lower surface, demonstrating that the test section walls are close enough to the model to be affected by the flow acceleration around the model. Wake profiles were measured from $X/c \approx 1$ to 4.5. In this

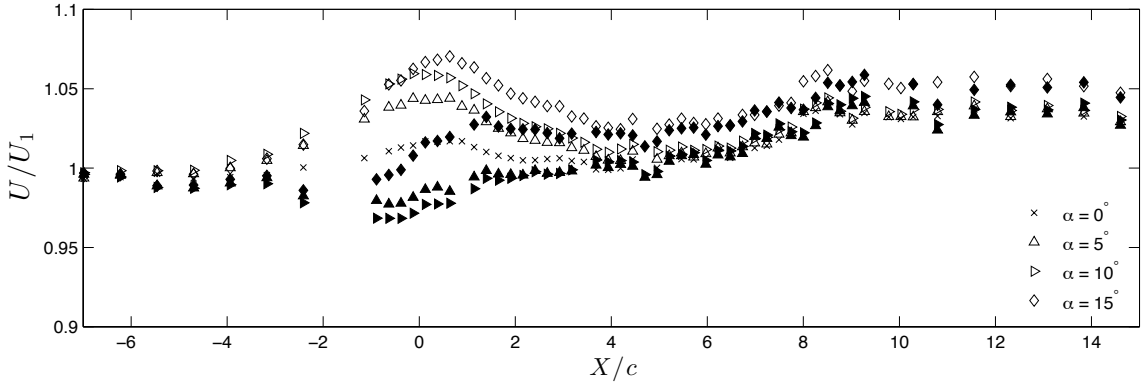

Figure 4.18: Variation in the outer flow around the NACA 0018 model, along the upper (hollow) and lower (solid) regions of the test section.

region the outer flow velocity is between 2% lower and 5% higher than the inlet velocity, U_1. The change in outer flow velocity is related to the streamwise location of the wake profile and vertical position in relation to the wake. Quantifying the change in the outer flow velocity permits the change in linear momentum to be calculated for drag coefficient calculations, when coupled with measured wake profiles of the streamwise velocity. Also, there exists some ambiguity in the appropriate location to measure freestream reference

properties for specific drag formulations. The values in Fig. 4.2 will permit the change in drag estimate due to measurement location, of the reference properties, to be quantified.

4.2.2 Surface Pressure Distribution

The airfoil surface pressure distributions are shown in Fig. 4.19. For attached flow conditions (Figs. 4.19a, 4.19b, and 4.19c), the existence of a separation bubble, on the suction side of the airfoil, is identified by the presence of a nearly constant region of pressure, in the surface pressure distribution, followed by rapid pressure recovery [72]. The approximate locations of separation (S), transition (T), and reattachment (R) taken from Ref. [73] are shown in Fig. 4.19. At $\alpha = 15°$ (Fig. 4.19d), a similar, approximately constant, pressure region exists, which extends to the the trailing edge. This identifies flow separation without subsequent reattachment [72]. Unlike with the circular cylinder, the viscous stress contribution to the drag is non-negligible, therefore, the drag cannot be accurately estimated from surface pressure measurements alone.

4.2.3 Wake Velocity Measurements

The mean and RMS velocity profiles measured in the wake of the NACA 0018 airfoil operating at a 10° angle of attack are shown in Fig. 4.20 - 4.23. The same parameters measured in the wake of the airfoil operating at $\alpha = 15°$ are shown in Figs. 4.24 - 4.27. The profiles for $\alpha = 0°$ and 5° can be found in Appendix D. For $\alpha = 5°$, 10° and 15° wake profiles were measured at four streamwise locations, specifically, $x/c = 1$, 2, 3, and 4.5, measured from the trailing edge. This streamwise range of wake profile measurement locations spans between the farthest upstream point typically recommended, $x/c = 1$, and the maximum extent of measurement, $x/c = 4.5$. All wake velocity profiles have been normalized by the average freestream velocity at the streamwise location of the profile, U_4. The average value of U_4 is found from the average freestream velocity measured in the upper and lower sections of the wake profile. To achieve acceptable levels of measurement uncertainty in the regions of highly turbulent flow, data were sampled for 40 seconds at 5000 Hz, resulting in 200,000 samples, at each measurement point.

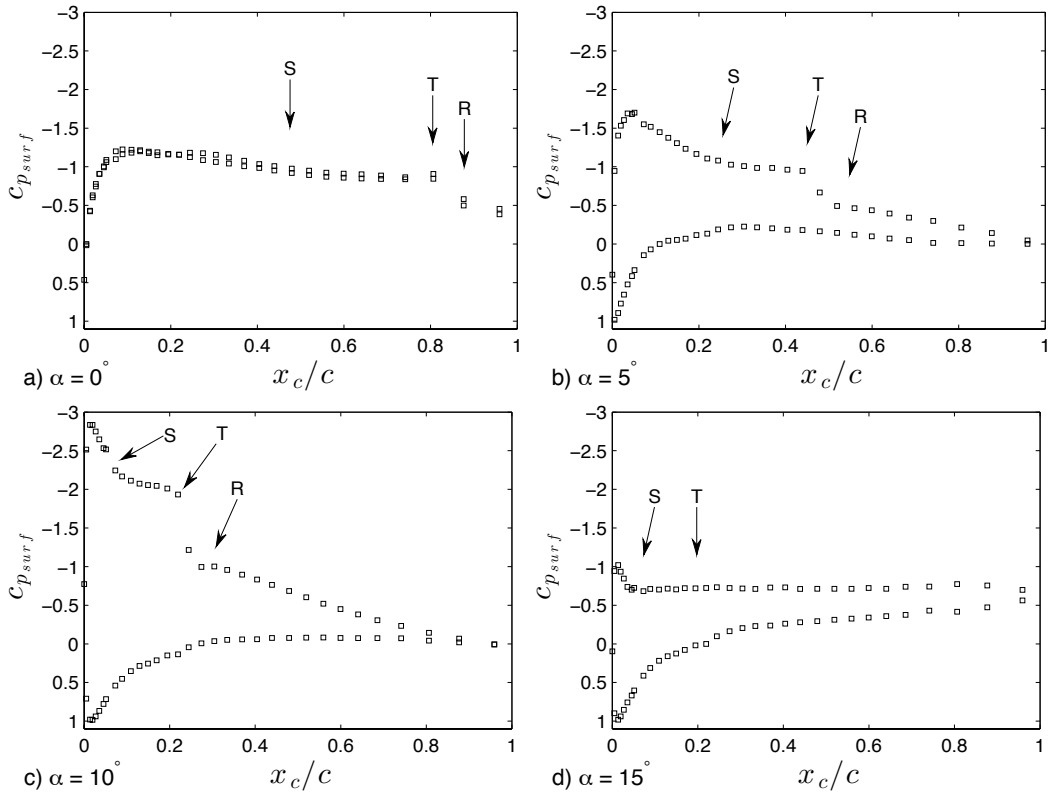

Figure 4.19: Surface pressure distributions measured over the upper and lower surfaces of the NACA 0018 airfoil. Locations of separation (S), transition (T), and reattachment (R) are taken from Ref. [73].

The wake profiles measured at all angles of attack show classical turbulent wake development. As the downstream distance increases, the wake spreads vertically while the maximum streamwise velocity deficit and turbulence intensity decreases. For non-zero angles of attack, the wake profiles contain the expected asymmetry relative to x. The discrepancy between the outer flow above and below the wake decreases with increasing streamwise distance. The difference is less than than 1% downstream of $X/c = 3$. This suggests drag estimates based on wake profiles measured farther downstream will be less affected by neglecting the differences in outer flow velocities, or averaging the flow characteristics.

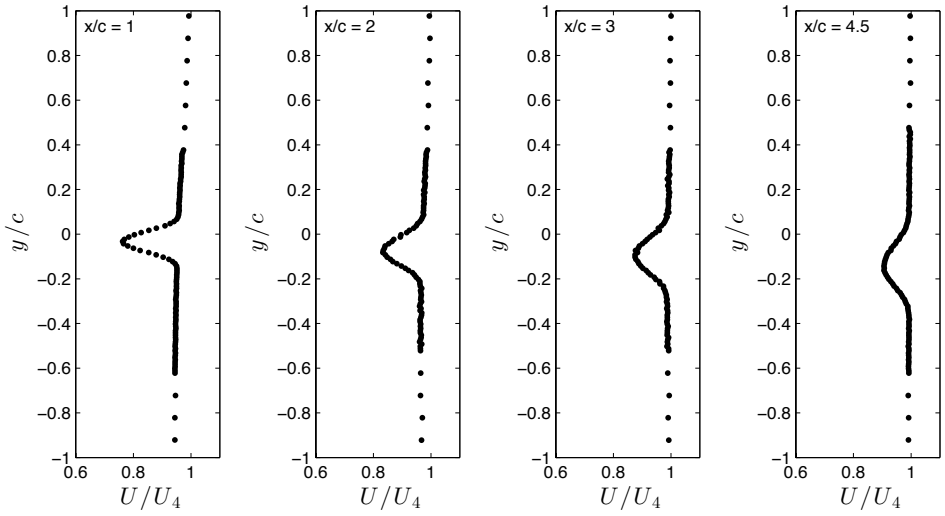

Figure 4.20: Mean streamwise wake profiles measured for the airfoil operating at an angle of attack of 10°.

As expected, when flow separates without reattaching ($\alpha = 15°$) the wake is much wider than the wake of the airfoil with attached flow at the trailing edge. In addition to a significant increase in wake width, the wake of the stalled airfoil is more similar to that of a bluff body than a streamlined body [16]. At $\alpha = 5°$ and 10°, the downwash from the airfoil results in a wake which develops at an angle, which is observable in the changing vertical position of the maximum vertical velocity deficit [74]. The same downwash effects are less significant in the airfoil wake at $\alpha = 15°$.

The streamwise growth of the wake half width is shown in Fig. 4.28, along with lines of best fit of each angle of attack investigated. Figure 4.28 illustrates the effect of flow separation on wake width. The increase in angle of attack between 5° and 10° results in a moderate increase in wake width, while increasing the angle of attack from 10° to 15° results in a significant increase in wake width since flow separates without reattachment on the suction side. Also, the growth rate of the wake increases with increasing angle of attack. The width of the airfoil wake at $\alpha = 15°$ grows proportionally to $x^{0.48}$, while at $\alpha = 5°$ and 10° it grows proportionally to $x^{0.46}$ and $x^{0.44}$, respectively. Also shown in

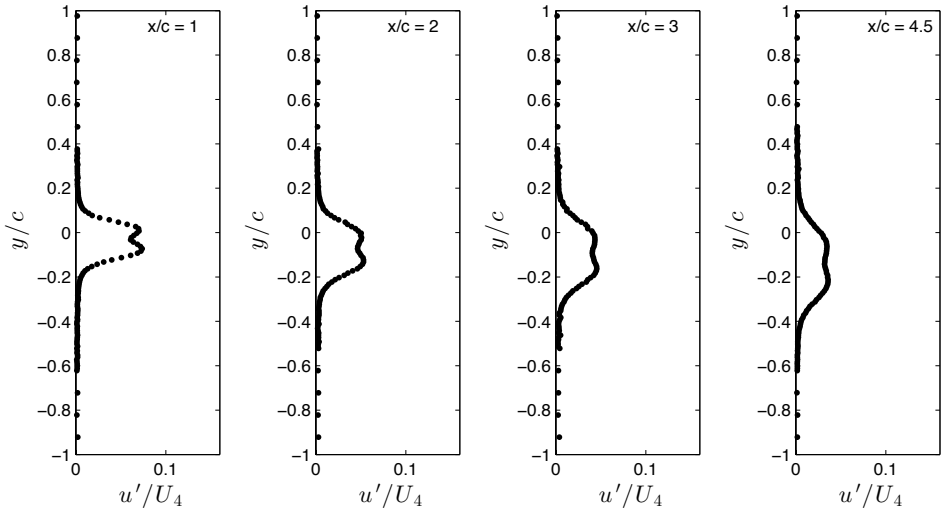

Figure 4.21: RMS streamwise wake profiles measured for the airfoil operating at $\alpha = 10°$.

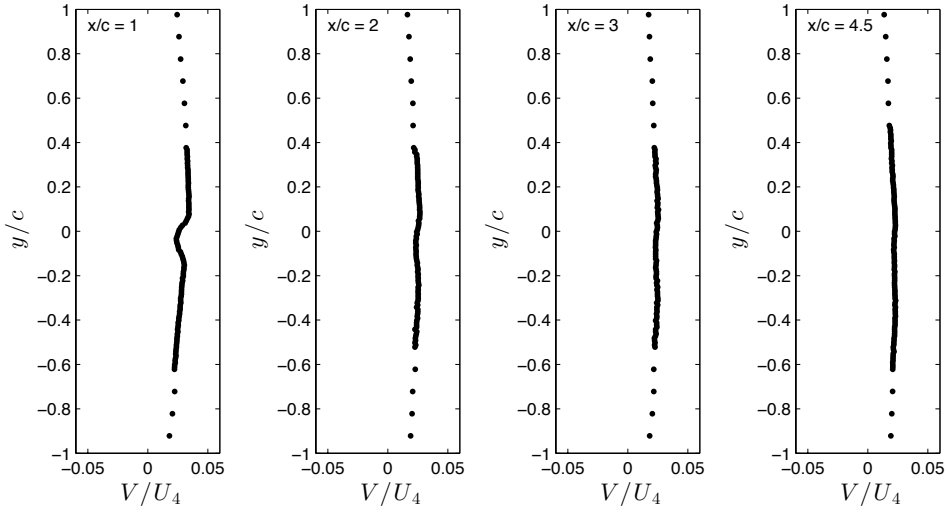

Figure 4.22: Mean vertical wake profiles measured for the airfoil operating at $\alpha = 10°$.

Fig. 4.28 is the wake half width taken from Ref. [74]. In Ref. [74] measurements were taken in the wake of a NACA 0018 airfoil set at $\alpha = 0°$ and operating under such conditions that the drag coefficient is 0.0073 [74]. Wake growth is proportional to $x^{0.43}$. This is similar to

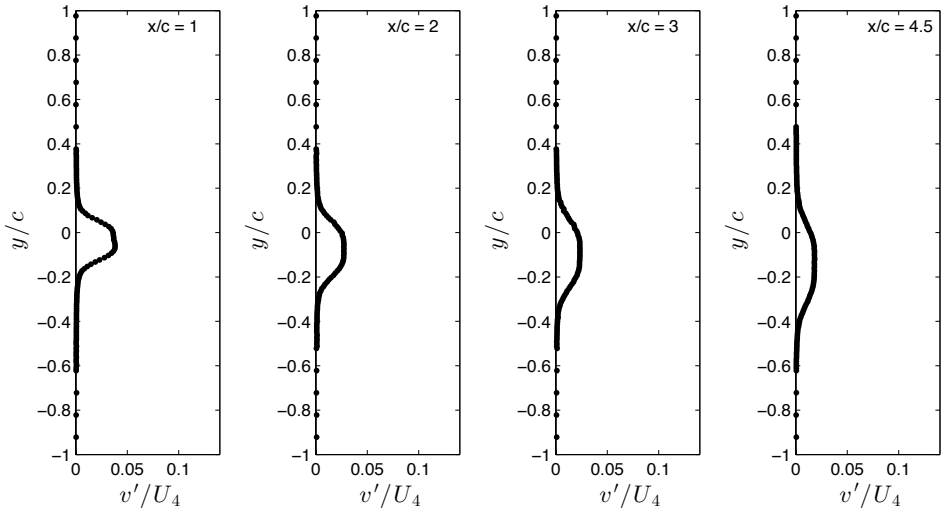

Figure 4.23: RMS vertical wake profiles measured for the operating airfoil at $\alpha = 10°$.

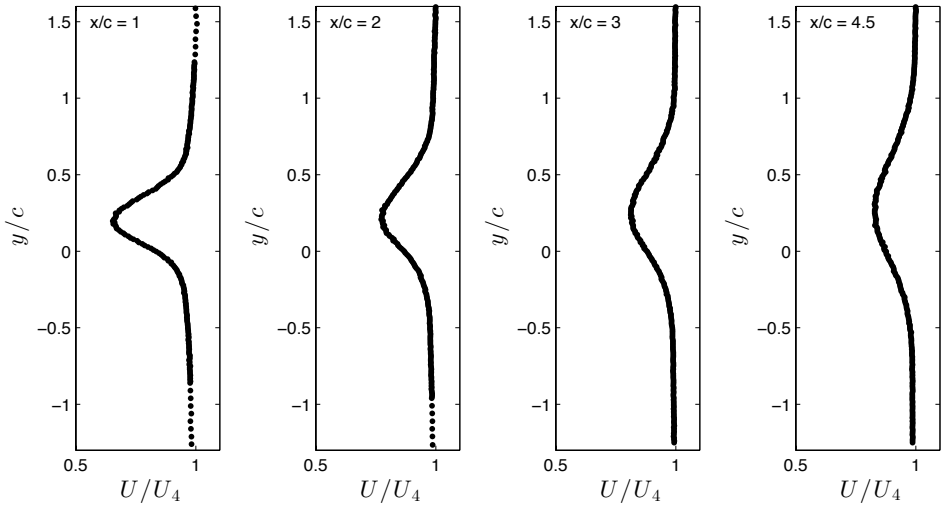

Figure 4.24: Mean streamwise wake profiles measured for the airfoil operating at an angle of attack of 15°.

the wake growth observed for the attached flow cases in the current study and lower than when flow separates without reattaching, as expected.

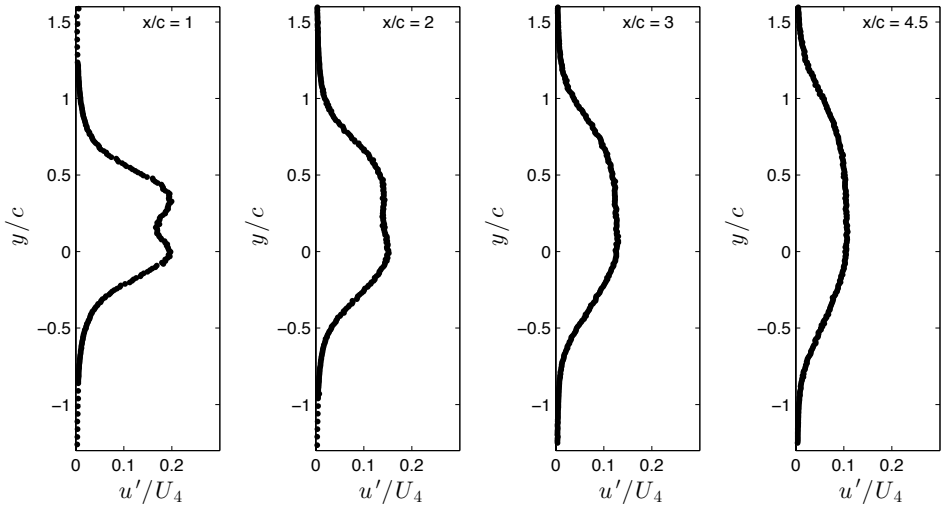

Figure 4.25: RMS streamwise wake profiles measured for the airfoil operating at $\alpha = 15°$.

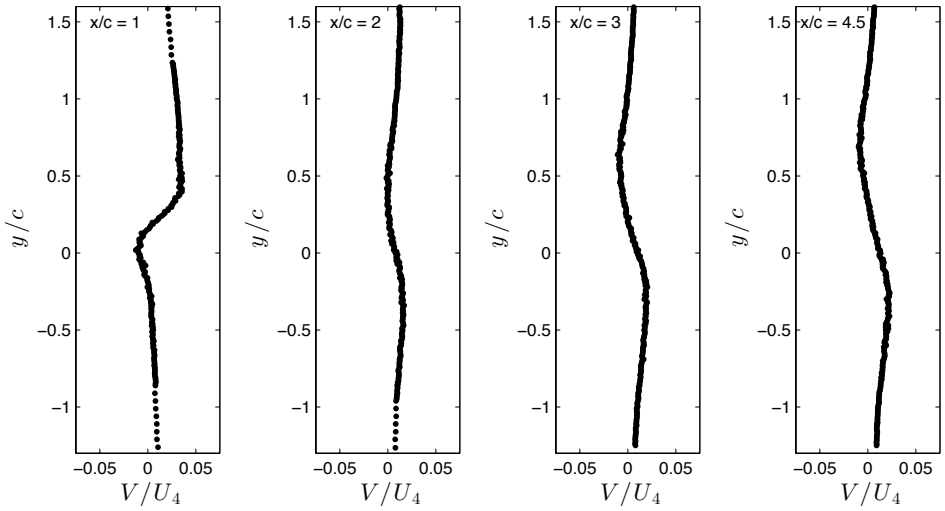

Figure 4.26: Mean vertical wake profiles measured for the airfoil operating at $\alpha = 15°$.

Recovery of maximum velocity deficit, pictured in Fig. 4.29, shows a similar difference between pre and post-stall wake characteristics. Post-stall the maximum velocity deficit

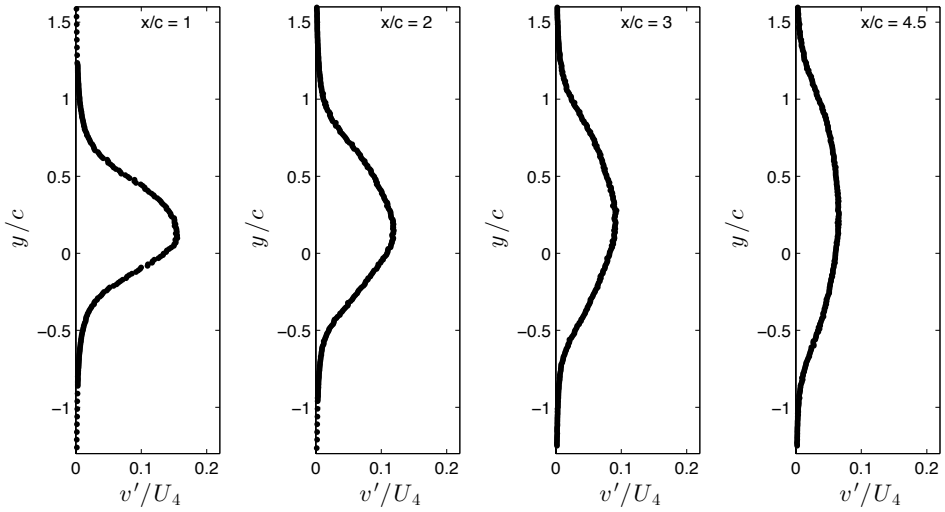

Figure 4.27: RMS vertical wake profiles measured for the airfoil operating at $\alpha = 15°$.

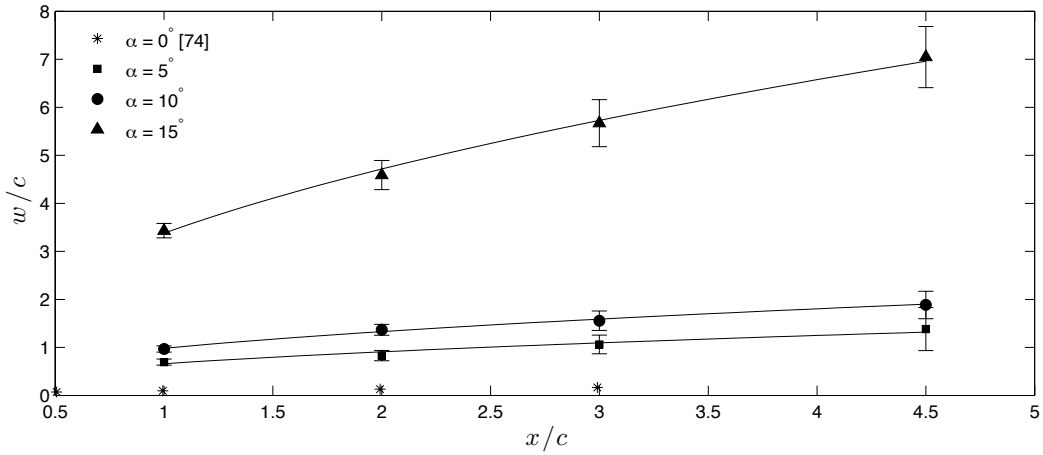

Figure 4.28: Streamwise growth of the wake half width. The wake growth for $\alpha = 0°$, shown for comparison purposes, wake measured in the wake of a NACA 0018 airfoil operating with a drag coefficient of 0.0073 published in Ref. [74].

is larger than in the wake of the airfoil with the flow attached at the trailing edge. Again the rate of recovery is not as significantly different, here the trendlines shown in Fig. 4.29

correspond to a velocity deficit recovery proportional to $x^{-0.55}$, $x^{-0.57}$, and $x^{-0.49}$, for $\alpha = 5°$, $10°$, and $15°$ respectively. The recovery of the streamwise maximum velocity deficit has been shown for a NACA 0025 airfoil operating at $\alpha = 5°$ and $Re_c = 100,000$ from Ref. [75]. Measurements were not extended far enough downstream to allow a reliable rate of recovery to be estimated, however, the reference points do not raise any concerns regarding the current data set.

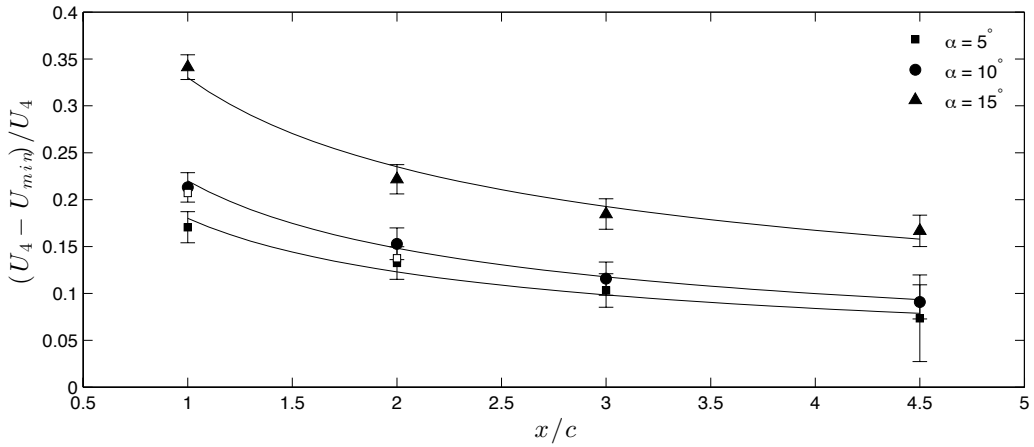

Figure 4.29: Streamwise evolution of the maximum velocity deficit measured in the wake. Solid symbols indicate values found in the current study. The hollow symbols, for $\alpha = 0°$, were based on wake profiles measured behind a NACA 0025 airfoil operating at $Re_c = 100,000$ published in Ref. [75].

The decay of the streamwise and vertical RMS velocity fluctuations in the wake are shown in Fig. 4.30, where the solid symbols indicate streamwise RMS fluctuations and the hollow symbols vertical RMS fluctuations at the same angle of attack. The maximum streamwise RMS fluctuations occurs at a different position, in relation to the maximum velocity deficit, for all three angles of attack. At $\alpha = 5°$, the maximum occurs below the wake center point at all streamwise positions. At $\alpha = 10°$ and $15°$ the streamwise RMS profiles contain a peak above and below the center point, similar to those of a circular cylinder. For $\alpha = 10°$ this double peak is found in all wake profiles and is slightly asymmetric in nature, the larger peak is located below the wake center point, and for $\alpha = 15°$

the double peaks are not distinguishable after $x/c = 2$. For comparison, the decay of the maximum streamwise RMS velocity fluctuations in the wake of a NACA 0025 airfoil, operating at $\alpha = 5^\circ$ and $Re_c = 100,000$, from Ref. [75] is shown in Fig. 4.30. As was observed in the wake of the circular cylinder, the maximum streamwise RMS fluctuations are greater than the maximum vertical RMS fluctuations at all streamwise locations and for all angles of attack. Profiles of the streamwise and vertical RMS velocity fluctuations measured downstream from a NACA 4418 airfoil operating at $Re_c = 40,000$ under stalled flow conditions published in Ref. [37] confirm that the streamwise components are larger than the vertical components in the near wake.

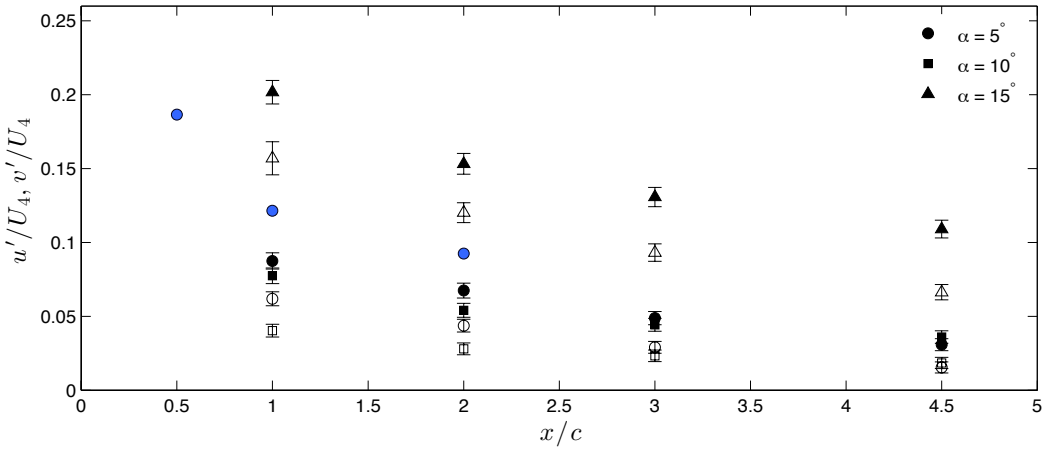

Figure 4.30: Decay of maximum streamwise (solid symbols) and vertical RMS (hollow symbols) velocity components in the wake of the airfoil. The symbols filled with blue indicate data from streamwise RMS profiles measured in the wake of a NACA 0025 airfoil operating at $Re_c = 100,000$ in Ref. [75].

4.2.4 Wake Pressure Measurements

Total pressure profiles and static pressure variation in the wake for $\alpha = 10°$ and the same profiles for $\alpha = 15°$, are shown in Figs. 4.31 and 4.32, and Figs. 4.33 and 4.34, respectively. Pressure measurements were taken with a pitot-static tube oriented along the streamwise axis. To compare the pressure based pitot-static tube measurements with the cross-wire

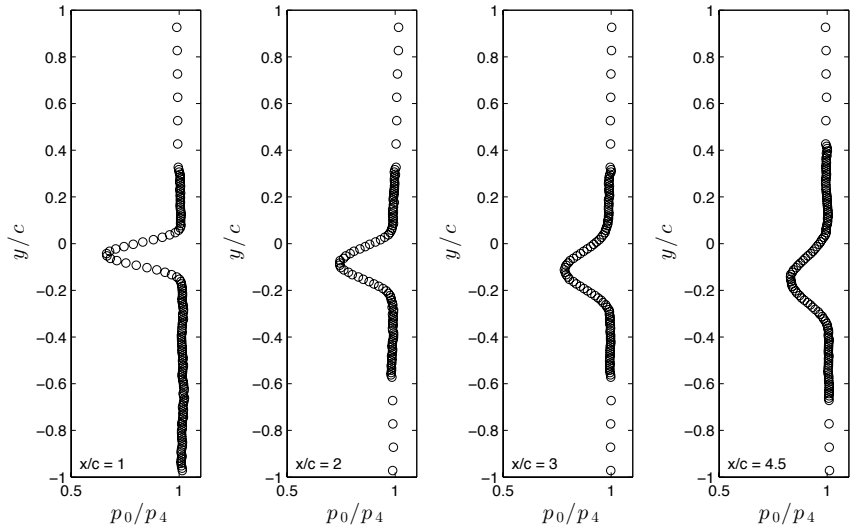

Figure 4.31: Normalized total pressure profiles measured with the pitot-static tube in the wake of the NACA 0018 airfoil operating at $\alpha = 10°$.

measurements, calculated velocity profiles, based on each set of measurements, have been compared for both angles of attack and at all streamwise locations. The comparison of the calculated streamwise velocities is shown in Figs. 4.35 and 4.36. With the exception of the profile measured at $x/c = 1$ for $\alpha = 15°$ the two measurement techniques show excellent agreement. At $x/c = 1$ for $\alpha = 15°$, there is a slight discrepancy between the calculated velocities predicted in the velocity deficit region of the wake. A similar discrepancy was also observed in the velocity profiles calculated for the cylinder at $X/d = 3$. The difference in measured values was related to the non-negligible vertical pressure gradient present in the flow, which is thought to also be the source of the error here. The streamwise recovery of minimum total pressure in the wake is shown in Fig. 4.37 for the angles of attack

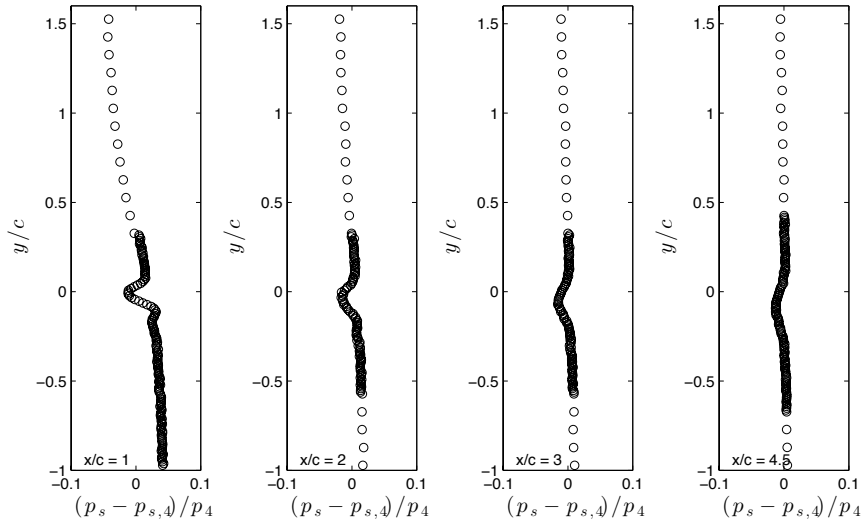

Figure 4.32: Static pressure variation in the wake profiles for the airfoil operating at $\alpha = 10°$.

investigated. Like the wake half width and maximum velocity deficit, there is a distinct difference in magnitude of the minimum total pressure in the wake of the airfoil without reattachment ($\alpha = 15°$) from that in the wake of an airfoil operating with attached flow at the trailing edge ($\alpha = 5°$ and $10°$). The minimum total pressure is lower, at all x/c locations in the former case than in the latter. For all three angles of attack the streamwise change in total pressure decreases as streamwise distance increases, and the minimum pressure approaches the total pressure in the outer flow. For the cases when flow remains attached at the trailing edge, i.e. $\alpha = 5°$ and $10°$, the total change in minimum static pressure is less than 20% of the outer flow total pressure between $x/c = 1$ and 4.5. For the stalled airfoil wake, $\alpha = 15°$, the overall recovery in minimum total is more than 40% of the total pressure measured in the outer flow. Recovery of the maximum static pressure deficit in the wake is shown in Fig. 4.38 for $\alpha = 5°$, $10°$, and $15°$. The same trends in recovery of static pressure deficit between the airfoil with a separation bubble and separated flow at the trailing edge are observed as in the total pressure recovery in terms of both magnitude

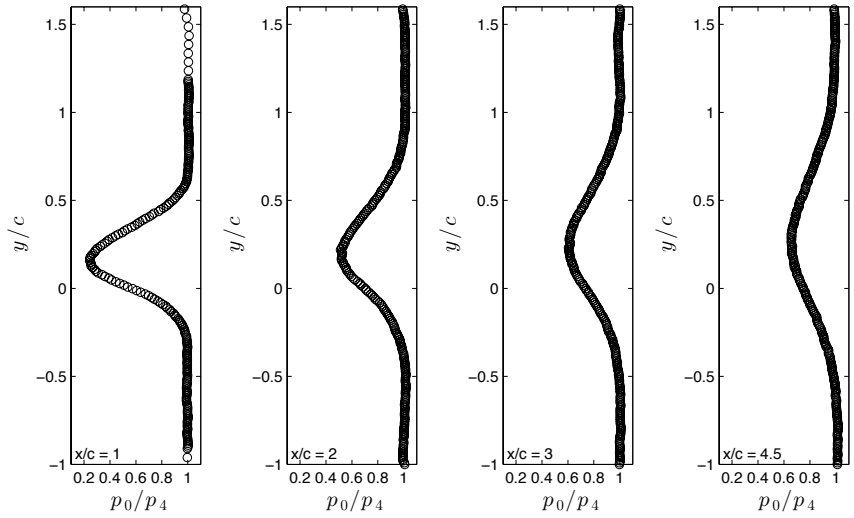

Figure 4.33: Normalized total pressure profiles measured with the pitot-static tube in the wake of the NACA 0018 airfoil operating at $\alpha = 15°$.

and rate of recovery. The total and static pressure recovery for the airfoil at $\alpha = 15°$ are similar to the recovery recorded for the circular cylinder (see Figs. 4.12 and 4.13).

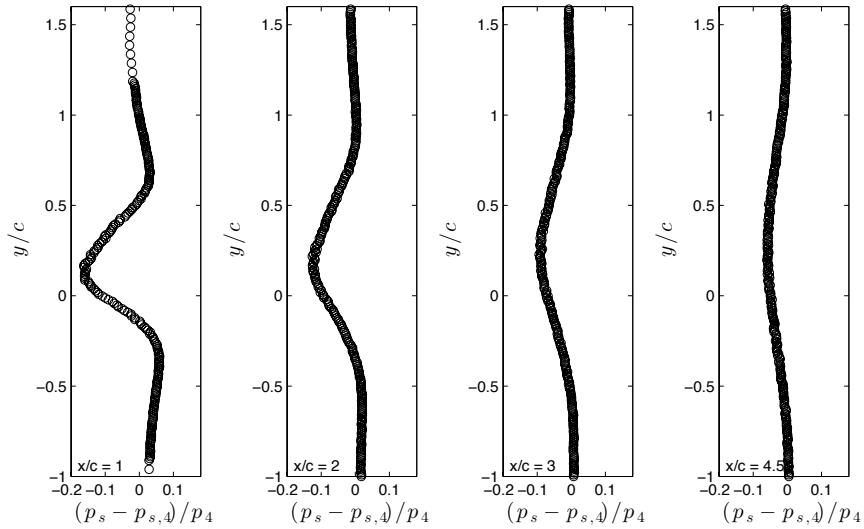

Figure 4.34: Static pressure variation in the wake profiles for the airfoil operating at $\alpha = 15°$.

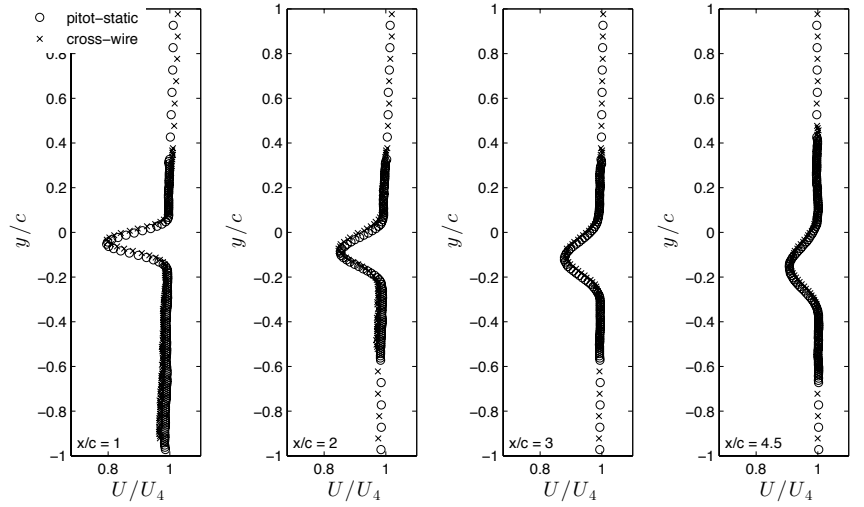

Figure 4.35: Comparison of calculated velocities based on pitot-static tube and cross wire measurements for the airfoil operating at $\alpha = 10°$.

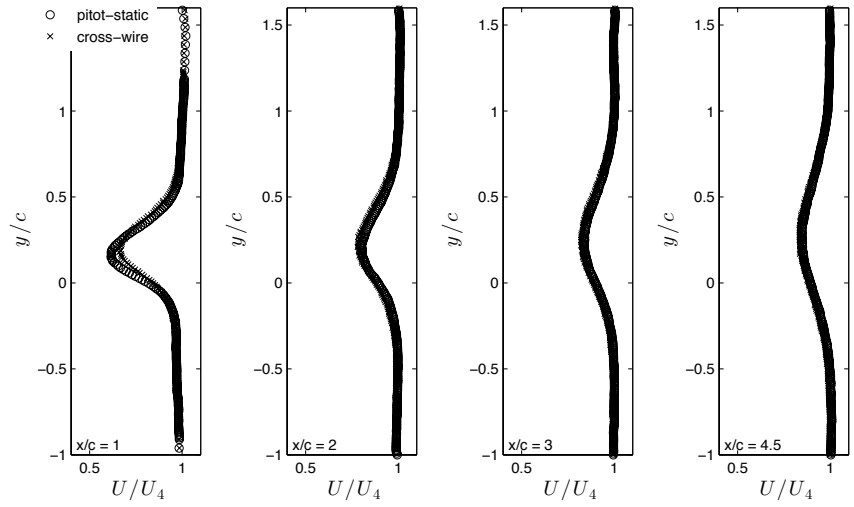

Figure 4.36: Comparison of calculated velocities based on pitot-static tube and cross wire measurements for the airfoil operating at $\alpha = 15°$.

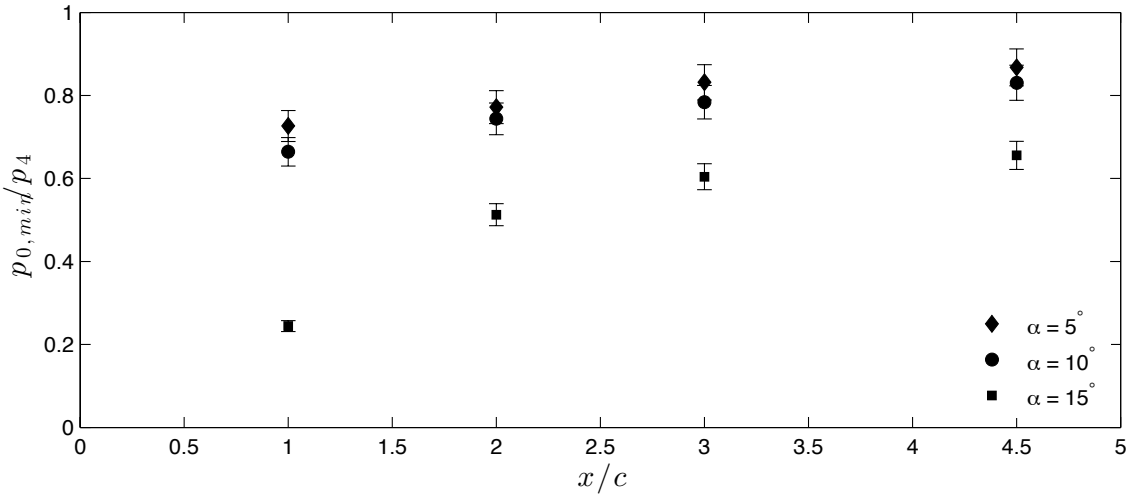

Figure 4.37: Streamwise change of minimum total pressure in the wake of the airfoil.

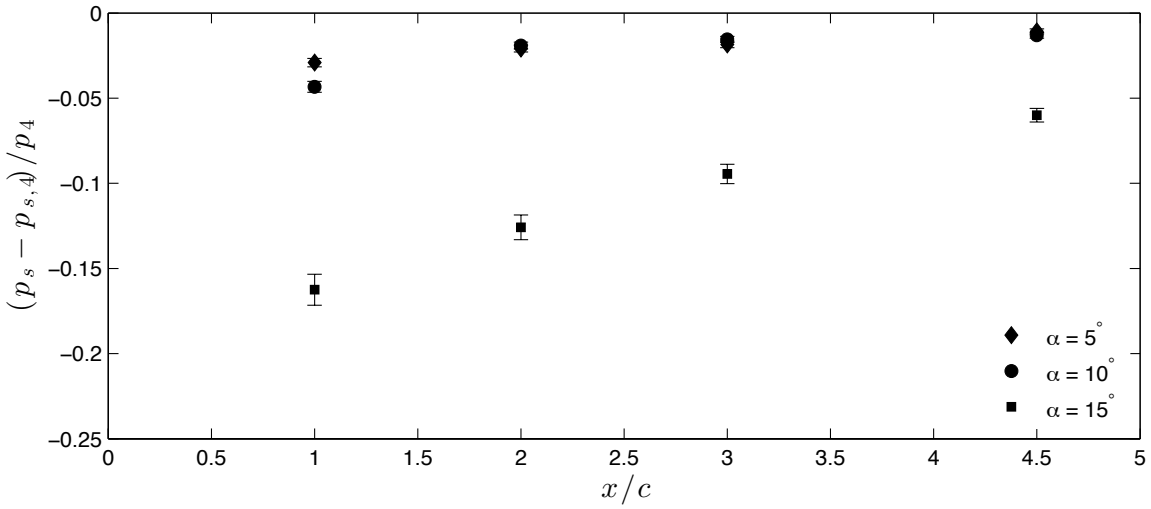

Figure 4.38: Streamwise change of maximum static pressure deficit in the wake of the NACA 0018 airfoil.

Chapter 5

Cylinder Drag Estimates

In this section drag coefficients for the circular cylinder shall be calculated from the measured wake profiles. The complete set of profiles measured in the wake of the cylinder operating at $Re_d = 8,000$ are presented in Chapter 4 and profiles measured for $Re_d = 20,000$ are presented in Appendix D. The error bars shown on the drag estimates, in Fig. 5.1, are based on experimental uncertainty in the measurements and calculated quantities involved in the drag estimates. The methodology for estimating drag coefficient uncertainty due to experimental uncertainties is detailed in Appendix A. Drag coefficients presented in Figs. 5.1 - 5.12 have been normalized by the pressure based drag coefficient for each Reynolds number. Pressure based drag constitutes about 96% of the total drag [35], it is therefore expected that the normalized estimates obtained from the control volume formulation shall exceed unity.

5.1 Control Volume Drag Estimation

Based on the measured profiles of mean and fluctuating velocity components, and the streamwise outer flow velocity variation, the drag coefficient of the cylinder can be calculated using the momentum integral drag formulation given in Eq. 3.13. This method, which shall be referred to as the complete control volume formulation since it relies on upstream measurements in conjunction with wake measurements, was used to calculate

drag estimates from each set of wake profiles measured. The results are shown in Fig. 5.1. Figure 5.1 reveals there is a strong variation in the calculated drag coefficient with the streamwise measurement location for both Reynolds numbers investigated. The change in drag coefficient with streamwise distance is unexpected since the drag formulation should be independent of control volume size, i.e. wake profile measurement location. The variation in drag estimates must be due to a combined effect of experimental uncertainties and inherent errors in the employed method, particularly due to simplifying assumptions.

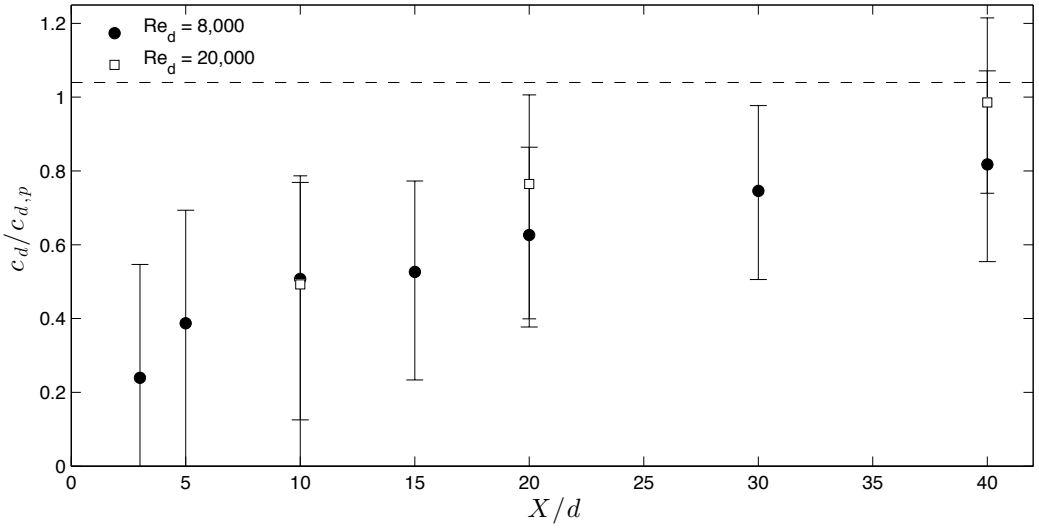

Figure 5.1: Drag coefficient estimated from the complete control volume formulation, normalized by the coefficient of drag based on surface pressure measurements. Error bars are calculated from measurement uncertainties.

The uncertainty in the drag estimates can be assessed using the error bars shown in Fig. 5.1. The estimated uncertainty is not large enough to explain the observed streamwise variation. As the streamwise distance increases, the experimental uncertainty decreases due to increasing wake width and decreasing turbulence intensity. Wake width is linked to estimated uncertainty since the spatial resolution in profile measurements was held constant. As the wake widens a greater relative spatial resolution is achieved, so that continuous velocity and pressure wake profiles are captured more accurately by the discrete

data points. This reduces the adverse effect of random measurement errors on the drag estimates. The uncertainty in cross-wire measurement is directly linked to turbulence intensity and, as the turbulence decreases, the measurements uncertainty decreases.

The results suggest that the observed variation in drag coefficient with x/c is due to inherent methodological errors. Two simplifying assumptions, tied to the variation of flow properties with X, were employed in deriving Eq. 3.13, (i) the relationship between the velocity field and pressure variation in the wake (Eq. 3.11), and (ii) the simplification of the τ_{xx} term (Eq. 3.9). To determine if either assumption is contributing to the variation in calculated drag coefficients, the validity of the assumptions will be checked at all streamwise locations investigated. The static pressure variation in the wake predicted with Eq. 3.11 has been compared against the pitot-static probe measured static pressure variation. The results are illustrated in Fig. 5.2 for $X/d = 3$ and 40 showing that Eq. 3.11, based on the cross-wire measurements, under-predicts the pressure variation within the wake. In the previous chapter, the vertical velocity fluctuations measured in the wake were found to be smaller than anticipated when compared to previous wake studies. Figures 5.2 and 5.3 adds further confirmation that the component of vertical velocity is under estimated with the current method of decomposing cross-wire measurements into the components of velocity. However, since streamwise velocity components have been verified as accurate, this only affects the prediction of pressure variation in the wake, from Eq. 3.11. The degree to which the pressure variation is under predicted by employing Eq. 3.11 diminishes with increasing streamwise distance. This is illustrated in Fig. 5.3 by the decreasing difference between the maximum static pressure deficit in the wake predicted by Eq. 3.11 and the maximum static pressure deficit from direct measurements.

To quantify the effect of the observed deviation in pressure estimation by Eq. 3.11 on the estimates of drag coefficient, drag calculations were repeated using the measured pressure variation in Eq. 3.13. The resulting drag estimates are shown in Fig. 5.4. Comparing Figs. 5.1 and 5.4, it can be seen that employing the measured pressure variation results in an increase in drag estimate and an overall decrease in the streamwise variation. As expected from Fig. 5.3, the relative increase in corrected drag coefficient decreases with streamwise distance. At $X/d = 3$, the drag increases by approximately 50% of $c_{d,p}$ and at, $X/d = 40$,

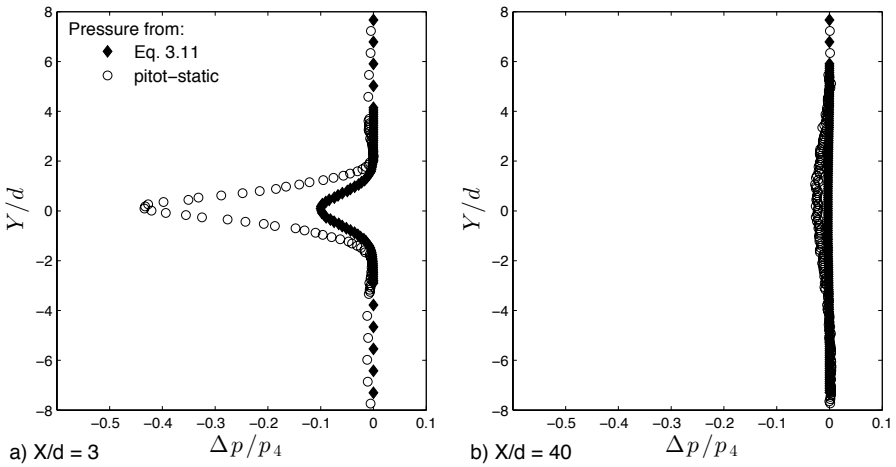

Figure 5.2: Pressure variation in the wake of the circular cylinder predicted through Eq. 3.11, based on cross-wire wire measurements, and through pitot-static tube pressure measurements.

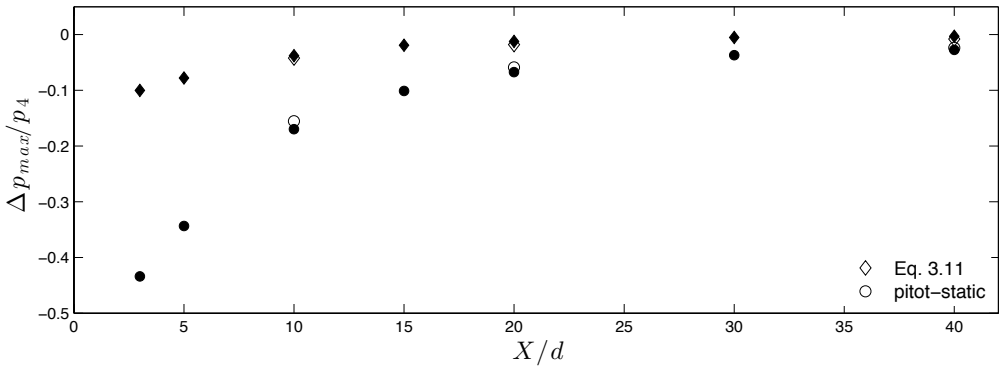

Figure 5.3: Comparison of the maximum static pressure deficit in the wake profile based on the predicted variation from Eq. 3.11 against the maximum static pressure deficit in the wake profile based on the pitot-static tube measurements. Filled symbols are used for $Re_d = 8,000$ data points and hollow symbols for $Re_d = 20,000$ data points.

the increase is less than 10% of $c_{d,p}$. With this correction, the drag estimates become closer to the expected value at all streamwise locations. The results suggest that, based on the

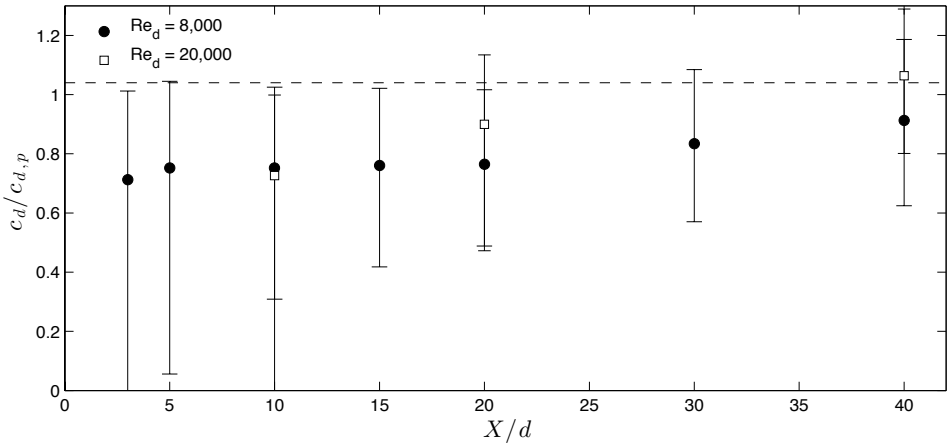

Figure 5.4: Drag coefficients calculated from Eq. 3.13, where static pressure variation in the wake is based on pitot-static measurements.

current method of measuring wake profiles, Eq. 3.11 is not a suitable approximation of the static pressure variation for profiles measured in the near wake.

To evaluate the possible significance of neglecting the viscous stresses, the magnitude of the viscous stress term in Eq. 3.9 was estimated. This was accomplished by approximating the streamwise change in U from the series of measured wake profiles and integrating the resulting $\frac{\partial U}{\partial x}$ profiles. Using this method, including viscous stresses are estimated to change the calculated drag coefficients by less than 0.01% at $Re_d = 8,000$. The contribution to the drag estimate, from viscous stresses, at $Re_d = 20,000$ was estimated to be lower than at $Re_d = 8,000$. This confirms that the viscous stress term is indeed negligible at all streamwise positions investigated here.

Even after verifying, and correcting, the assumptions with strong links to flow characteristics which change with streamwise position, the resulting drag coefficients still exhibit streamwise variation. To determine if the source of the remaining discrepancy can be identified, other simplifying assumptions that were employed to derive Eq. 3.13 shall be examined. The simplifying assumptions were employed to allow the formulation to be evaluated experimentally. The two remaining assumptions are related to neglecting the

contribution due to pressure on the top and bottom control volume surfaces and the effect of basing the upstream velocity, U_1, on outer flow measurements in the wake.

Pressure variation along boundaries 2 and 3 was neglected since the angle, β, the boundary makes with the x-axis was assumed to be small. To estimate the contribution to the drag from the pressure variation along these boundaries, it is necessary to approximate the pressure acting on the boundaries. Since boundaries 2 and 3 were assumed to lie on streamlines and the measured wall pressure distributions are equivalent the pressure variation in the outer flow (see Section 4.1.1 for details), the measured outer flow pressure variation was employed to approximate the distribution along the boundaries. Incorporating the estimated pressure variation into the calculation of drag coefficients resulted in a change of less than 0.1% in c_d for $Re_d = 8,000$. For $Re_d = 20,000$, this produced an average increase of 0.5% in c_d. These findings confirm that the contribution due to pressure variation along boundaries 2 and 3 can be neglected for all drag estimates presented here.

To evaluate Eq. 3.13, it is necessary to quantify the upstream velocity, U_1, during the experiment. Since it was not possible to experimentally measure this parameter in conjunction with wake profile measurements, the upstream velocity was calculated for each experiment. It was possible to calculate the upstream velocity from the outer flow velocity variation data (Fig. 4.18) and the outer flow measurements taken during the wake profile measurement, i.e. $U_1 = \zeta U_4$, where ζ is based on the measured freestream variation. The outer flow velocity at the wake profile location, U_4, is based on the average value of multiple data points measured in the outer flow, above and below the velocity deficit region. The estimated uncertainty in U_4, and therefore U_1, due to variation of U with Y at a given X location and data scatter due to random errors is estimated to be less than 0.5%. The effect of this uncertainty in U_1 has been captured in the estimates of drag coefficient error along with experimental uncertainty. The effect of this parameter alone is shown in Table 5.1 as a percentage of the reference pressure drag, $c_{d,p}$. The average change in drag coefficient, due to a 0.5% change in U_1, is 19% at $Re_d = 8,000$ and 16% at $Re_d = 20,000$. At $X/d = 40$ this accounts for more than 50% of the total uncertainty in the drag coefficients. The results in Table 5.1 indicate that this method of estimating drag is sensitive to uncertainty in the estimation of the upstream velocity, U_1. It is therefore essential to employ a reliable

Table 5.1: Change in drag coefficient, as a percent of $c_{d,p}$, resulting from $\pm 0.5\%$ perturbation of U_4.

Re_d	X/d						
	3	5	10	15	20	30	40
$8,000$	18.8	18.7	18.5	18.5	18.3	18.2	19.9
	-19.2	-19.0	-18.9	-18.9	-18.7	-18.6	-20.3
$20,000$	-	-	16.4	-	16.2	-	15.9
	-	-	-16.8	-	-16.5	-	-16.2

method of measuring the upstream velocity. In the current study, accuracy of wake profile measurements taken in the outer flow region is important.

After accounting for simplifying assumptions and experimental uncertainty, there still exists a discrepancy between the complete control volume based drag estimates and the pressure based reference drag coefficient, for profiles measured at $x/c \leq 30$. However, the pressure based drag coefficient was normalized by the dynamic pressure at boundary 1, which is equivalent to replacing U_0^2 with U_1^2 in Eq. 3.13. Changing the normalization parameter to U_1^2 results in a 2.5% increase at all streamwise locations for both Reynolds numbers. Even accounting for the normalization parameter, the drag estimates are lower than expected, except for the drag coefficient based on the wake profile measured at $X/d = 40$.

Figures 5.5 and 5.6 illustrate the significance of the individual terms in Eq. 3.13 to the total drag estimates for $Re_d = 8,000$ and $Re_d = 20,000$. The drag estimates from both Figs. 5.1 and 5.4 are included in Figs. 5.5 and 5.6. Terms I and II are common to both drag calculations and are therefore only shown once. It is Term III, the drag contribution due to pressure acting on the surface of the control volume, where the differences arise. Therefore, for this term, solid markers indicate the values based on pressure variation from cross-wire measurements, and hollow markers are for the values based on calculations including the measured static pressure variation. For clarity, experimental uncertainty estimates are not shown in Figs. 5.5 and 5.6. As expected from the decay of the streamwise velocity fluctuations (Fig. 4.10) the magnitude of Term II decreases with increasing streamwise

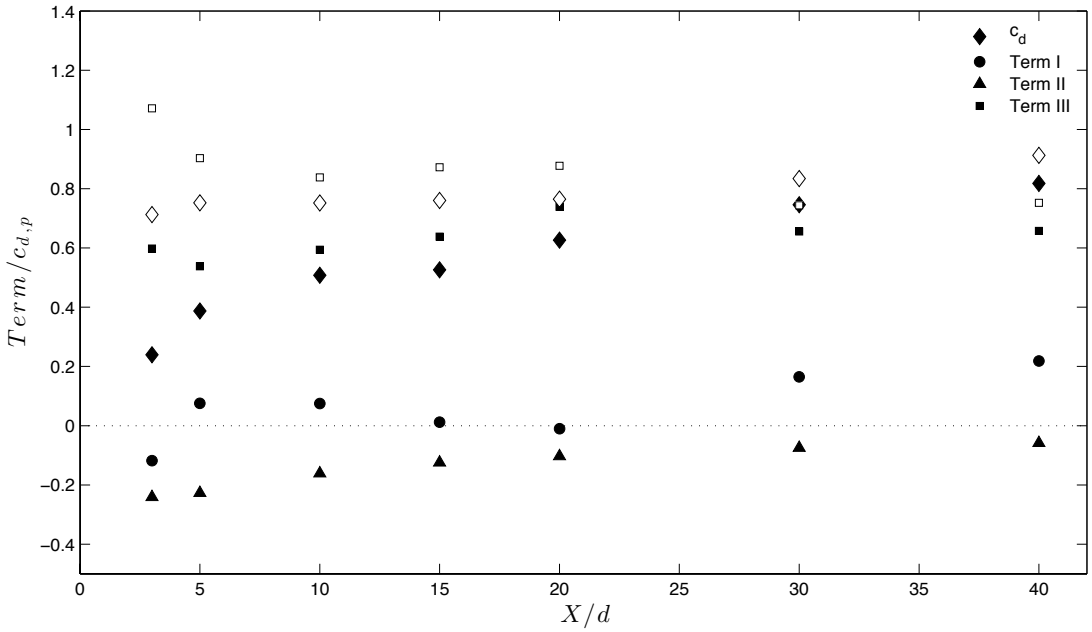

Figure 5.5: Contribution of the individual terms in Eq. 3.13 towards the total drag coefficient for $Re_d = 8,000$, where; Term I is the contribution due to rate of change of linear momentum in the control volume, Term II the contribution due to Reynolds and viscous stresses acting on the boundaries, and Term III the drag contribution due to pressure acting on the control volume surface. Solid markers indicate terms calculated from cross-wire measurements and hollow symbols those based on pitot-static tube measurements.

distance, however, even at $X/d = 40$, it remains non-negligible. At $Re_d = 8,000$, the variation of Term I with streamwise position appears unusual since it increases and decreases repeatedly over the region of the wake investigated, however, this mirrors the streamwise variation in outer flow observed in Fig 4.2. Term III, based on either method, follows a reverse trend to that observed in Term I, indicating that the primary cause of the streamwise variations in both terms is the variation in outer flow velocity in the test section. The difference between inlet, U_1, and outlet, U_4, velocities are a significant contribution to Terms I and III. Comparing Term III, based solely on cross-wire measurements (solid symbols in Figs. 5.5 and 5.6), and Term III, based on measured static pressure in addition to cross-wires measurements (hollow symbols in Figs. 5.5 and 5.6), reveals that the

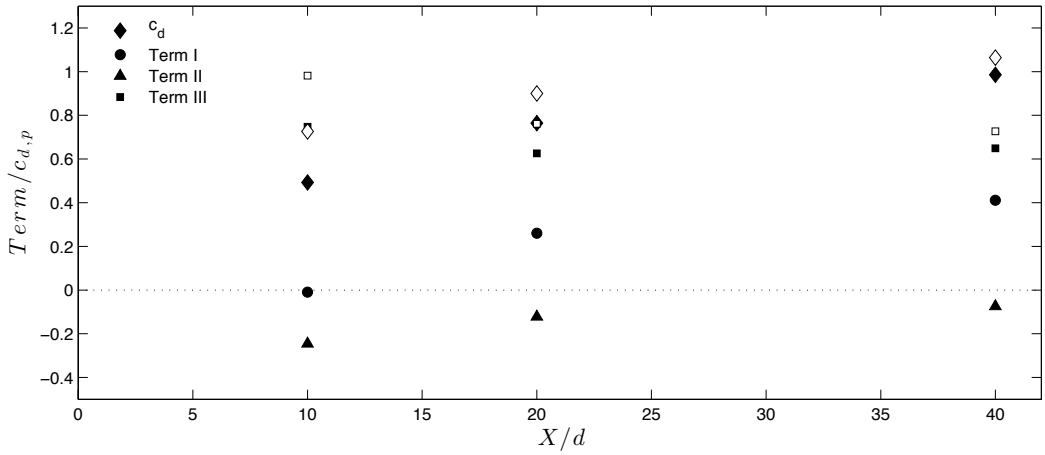

Figure 5.6: Contribution of the individual terms in Eq. 3.13 towards the total drag coefficient for $Re_d = 20,000$. Solid symbols indicate terms calculated from cross-wire measurements and hollow markers those based on pitot-static tube measurements.

underlying trend is the same. However, the difference between the two values decreases with increasing streamwise position. This matches expectations since the underlying trend is attributed to the difference between U_1 and U_4, which is the same in both calculations. The main conclusion supported by Figs. 5.5 and 5.6 is that no individual term in Eq. 3.13 is negligible.

The pressure variation in the near wake cannot be accurately estimated from Eq. 3.11 using the cross-wire measurements of the vertical velocity fluctuations. If drag calculations are performed using the static pressure variation predicted by Eq. 3.11, the drag coefficient can be up to 50% lower than the drag coefficient based on the measured pressure variation. It is therefore advisable, in the current study, to measure the static pressure variation in the wake directly. Drag estimates proved to be very sensitive to the value of U_1 employed. A change of 0.5% in the magnitude of U_1 resulted in a change of 15 - 20% in the calculated drag estimate. Therefore, employing an accurate method of measuring or calculating this parameter is essential for reliable drag estimates.

Calculated drag coefficients, based on measured static pressure variation, approach the expected value as the X/d location of the profile increases. At the furthest downstream

location, $X/d = 40$, the calculated drag coefficient is still approximately 10% lower than the expected value. The difference between calculated drag coefficients and the expected value can be explained by the estimated uncertainty for $X/d \geq 30$. At $Re_d = 20,000$, the expected value of drag is within the ranges of values predicted by the estimated experimental uncertainty for $X/d \geq 20$. These results indicate that if wake profiles are measured at $X/d \geq 30$, the drag estimates should have less than 10% error associated with the method.

5.2 Drag Estimates Based on Jones' Methods

Jones' method is a momentum integral drag formulation based on the assumption that the total pressure is constant in a streamtube which extends from the measured wake plane to an imaginary plane located infinitely far downstream. More details on the theoretical foundation of this method can be found in Ref. [10]. The equation for Jones' drag formulation is given in Eq. 5.1, taken from Ref. [10], where G is the total and P is the static pressure measured along a line normal to the wake. To use this method, it is necessary to measure total and static pressure profiles in the wake.

$$c_d = 2 \int_{\frac{l_4}{L}} \sqrt{\frac{G-P}{G_\infty}} \left(1 - \sqrt{\frac{G}{G_\infty}}\right) \mathrm{d}\left(\frac{y}{L}\right) \tag{5.1}$$

The reference pressure, G_∞, is the total pressure measured in the outer flow. Some ambiguity exists as to where G_∞ should be measured in wind tunnel experiments. The original formulation was designed for in-flight measurements where the outer flow characteristics are approximately constant. When originally implemented in a wind tunnel study, total pressure was measured in the outer flow at the location of wake profile measurement due to physical measurement limitations but, it was recommended that the reference should be measured upstream of the model where possible [10]. Drag calculations were initially performed with the reference total pressure measured in the outer flow at the wake location, i.e. $G_\infty = G_4$. The resulting drag coefficients are shown in Fig. 5.7 along with normalized drag coefficients from Ref. [42] estimated from Jones' method. The error bars

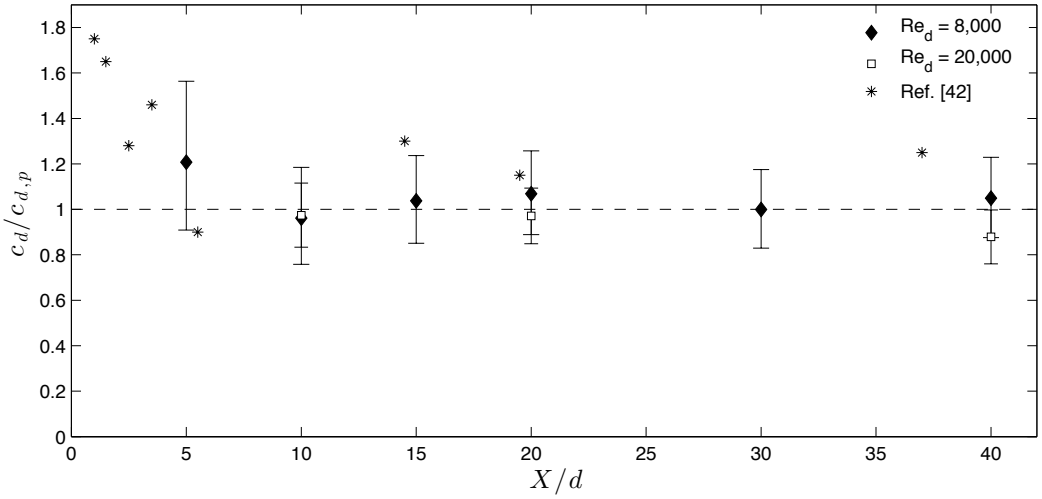

Figure 5.7: Drag coefficients for the circular cylinder calculated from Eq. 5.1 where $G_\infty = G_4$.

shown on the drag coefficients are computed based on experimental uncertainty, as detailed in Appendix A.

At $Re_d = 8,000$, drag estimates vary within approximately 20% of the reference value for all wake locations presented here. At $Re_d = 20,000$, the variation in drag estimates decreases to 10% of the reference value. The error in drag estimates decreases with increasing streamwise distance to $X/d = 10$. After this point, the drag estimates exhibit random variation within approximately 10% of the reference pressure based drag coefficient. However, for both Reynolds numbers, this variation is within the experimental uncertainty. In a study performed on a circular cylinder operating at a Reynolds number of $40,000$, Takahashi [42] reports a similar variation in drag coefficients found through applying Jones' method. In their study, the variation decreased dramatically downstream of $X/d = 10$, but remained present in all results up to the maximum X/d position investigated ($X/d = 37$). In Ref. [42], the observed variation in drag estimates for $X/d < 10$ was thought to be primarily the result of experimental uncertainty. The experimental uncertainty estimated for the current results supports this, as the estimated error decreases notably between $X/d = 5$ and $X/d = 10$. However, the source of the streamwise variation in drag estimates

may lie within the assumptions used to construct Eq. 5.1. The assumption of constant total pressure along a streamtube connecting the wake profile location with a plane infinitely far downstream is proven incorrect in Fig. 4.15. At $Re_d = 8,000$, pressure recovery occurs rapidly over $X/d < 20$ and then slows significantly. A similar trend is observed for the pressure recovery in the wake at $Re_d = 20,000$, see Appendix D for details. However, it is not possible to quantify the error introduced into the drag estimates due to this assumption.

To explore the suggestion in Ref. [10], of using an upstream reference pressure, drag calculations were repeated with the reference pressure measured at boundary 1, i.e. $G_\infty = G_1$. Measuring the reference pressure at boundary 1, resulted in negative values for some measurement locations. These results suggest that, while the approach may be valid in a test section where flow conditions resemble those of an unbounded flow, it is an unsuitable location to measure reference pressure when experiments are conducted in a test section where blockage effects exist.

Since G_4 is the reference pressure for the results presented in Fig. 5.7, the normalization velocity for the coefficient of drag is U_4. Adjusting the normalization to match that used for $c_{d,p}$ results in an increase in drag estimate of between 2% and 4% at $Re_d = 8,000$ and approximately 4% at $Re_d = 20,000$. Adjusting the normalization results in only a minor change to the drag estimates presented in Fig. 5.7 and does not change the observed trends.

The results indicate that Jones' formulation is a viable method for calculating drag only if wake profiles are measured at or beyond $X/d = 15$. Since measuring the reference pressure upstream of the cylinder resulted in non-physical drag coefficients, the reference pressure should be measured in the outer flow at the streamwise location of the measured wake profile. However, care should be taken in selecting the appropriate parameter for normalizing the drag coefficient.

5.3 Drag Estimates Based on van Dam's Formulation

The final formulation included for estimating drag based on flow field measurements has been presented in detail by van Dam [5]. This formulation is similar to the complete

control volume formulation, however, conservation of mass has been included in the linear momentum term to isolate the measurement region to the wake. The expression for drag coefficient is as follows,

$$c_d = \frac{2}{U_\infty^2} \int_{\frac{l_4}{L}} \left[\underbrace{U(U_\infty - U)}_{\text{Term I}} - \underbrace{\overline{u'^2}}_{\text{Term II}} + \underbrace{\overline{v'^2}}_{\text{Term III}} \right] \mathrm{d}\left(\frac{y}{L}\right) \tag{5.2}$$

Similar to Jones' formulation, van Dam's formulation is constructed based on unbounded flow assumptions, where U_∞ is a constant. To determine the appropriate location to measure U_∞ in a closed test section, drag calculations were performed with the reference velocity measured at boundary 1 and in the outer flow at boundary 4, i.e. $U_\infty = U_1$ and U_4, respectively. Drag coefficients calculated with $U_\infty = U_1$ are shown in Fig. 5.8a. Using an upstream reference results in non-physical drag coefficients for the majority of the wake profile locations surveyed. However, it is conceivable that, under certain test section conditions, reasonable, yet erroneous, drag estimates might be arrived at using an upstream reference. It is therefore important to note that the reference velocity must be measured in the outer flow of the wake at the location of the wake profile measurement. The drag coefficients calculated with such a reference are shown in Fig. 5.8b. The change in drag coefficient with streamwise position in Fig. 5.8b is the same as that observed in the initial drag calculations based on the complete control volume formulation (Fig. 5.1). The assumptions employed to arrive at Eq. 5.2 were also used in the complete control volume formulation, therefore the cause of the streamwise variation is due to the method used to predict the pressure variation in the wake (Eq. 3.11). As shown in Fig. 5.8c, recalculating drag estimates using the pressure variation measured with a pitot-static tube, instead of the velocity based approximation, results in reduced variation in drag estimates with streamwise position. Using this method brings the drag estimates closer to the expected value at all streamwise locations. The effect is more pronounced at lower X/d locations, where the difference between the predicted and measured static pressure wake profiles is the greatest. The overall variation with X/d is still present in the estimates but diminished.

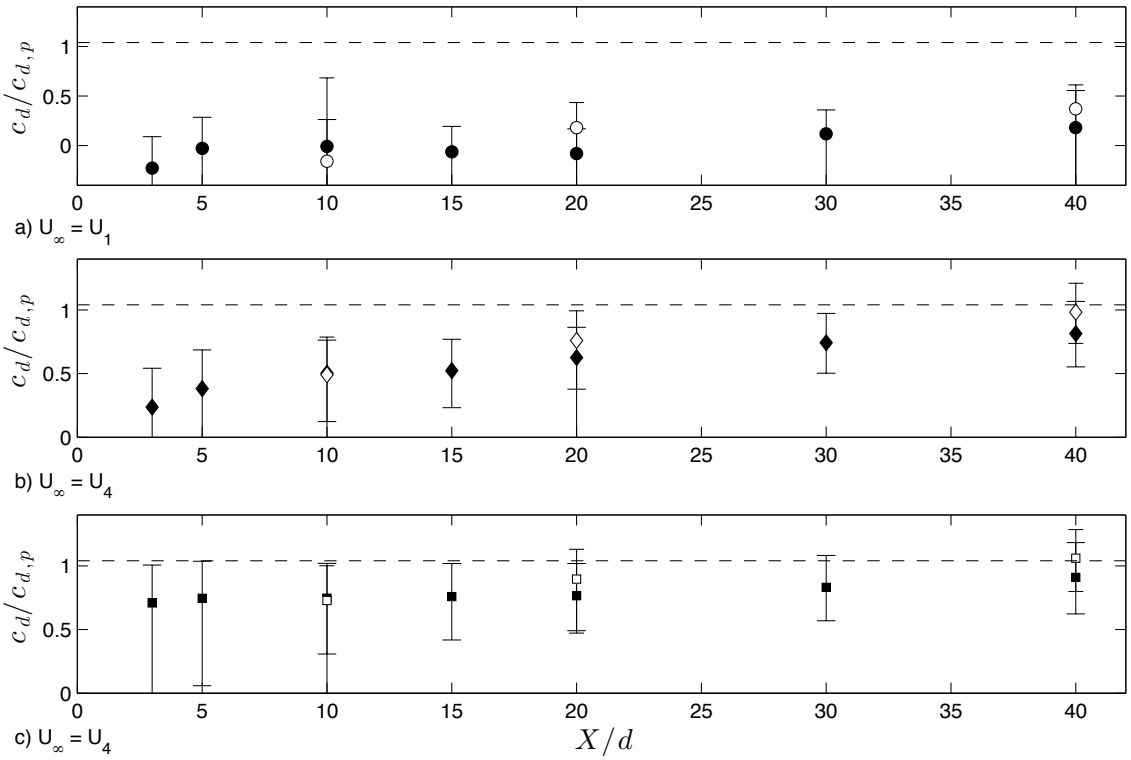

Figure 5.8: Drag coefficients for the circular cylinder based on van Dam's method. Drag coefficients for the cylinder operating at $Re_d = 8,000$ are indicated by the solid symbols and $Re_d = 20,000$ by the hollow symbols.

These changes are the same as those observed in the results based on the complete control volume method when the measured static pressure variation was employed (Fig. 5.4).

In the investigation of the complete control volume formulation it was determined that the estimates were sensitive to the value of U_1 employed in calculations. The estimates based on van Dam's method were found to be similarly sensitive to the value of U_∞. A 0.5% change in U_∞ resulted in a change in magnitude of 16 - 20% of the pressure based drag coefficient at $Re_d = 8,000$. At $Re_d = 20,000$, the change in drag estimate was approximately 15% of the pressure based drag coefficient. These levels of change are very similar to those reported in Table 5.1.

Using U_4 as the reference velocity results in a drag coefficient which was divided by U_4^2, unlike the reference pressure drag coefficient. Correcting for this results in an increase in drag of 2 - 4% at $Re_d = 8,000$ and approximately 4% at $Re_d = 20,000$. This adjustment of the drag coefficients results in drag estimates which are slightly closer to the expected value but does not change the observed trends.

Figures 5.9 and 5.10 illustrates the contribution to the total drag from the individual terms in Eq. 5.2. Terms I, II, and III are related to the linear momentum, Reynolds stresses, and pressure variation in the wake respectively. The magnitude of Terms II and III decrease with streamwise distance, while Term I increases. Comparing Term II based on cross wire measurements (filled symbols) and Term II based on the measured static pressure variation (hollow symbols) reveals that the two quantities follow the same trend with streamwise distance, though the rates of decay differ. Examining the drag coefficient terms at $X/d = 40$ reveals that if Terms II and III are neglected from the analysis, the

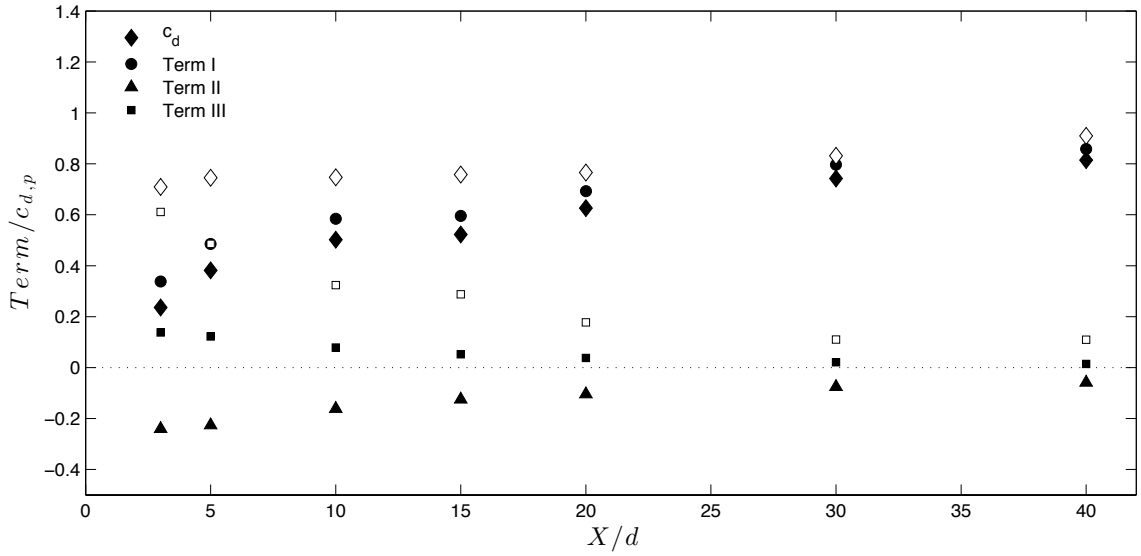

Figure 5.9: Contribution of the individual terms in Eq. 5.2 towards total drag coefficient for the cylinder operating at $Re_d = 8,000$. Solid markers indicate terms based on cross-wire measurements, whereas hollow markers indicate those terms based on static pressure measurements.

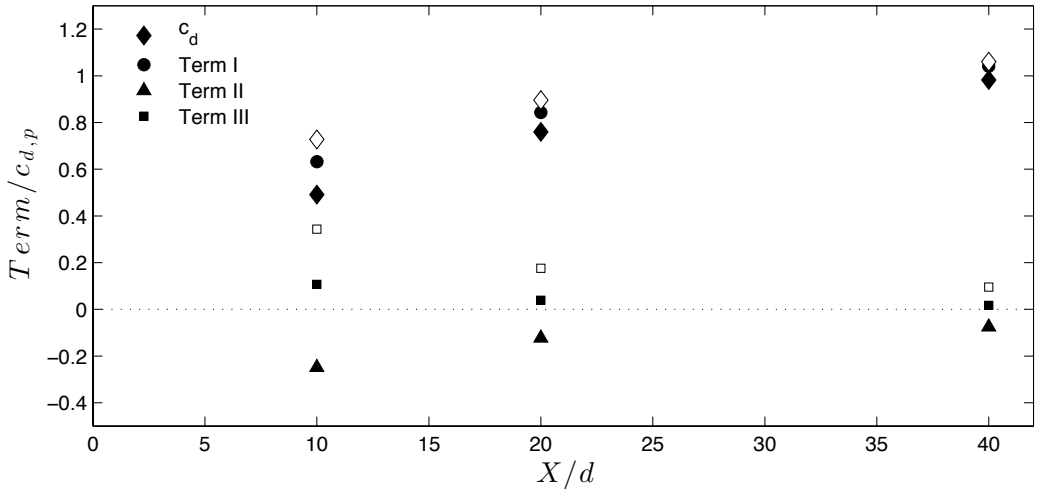

Figure 5.10: Contribution of individual terms in Eq. 5.2 to total drag coefficient at $Re_d = 20,000$. Solid markers indicate terms based on cross-wire measurements, and hollow markers indicate those terms based on static pressure measurements.

overall drag coefficient would change by less than 6% for the measured pressure variation estimate at $Re_d = 8,000$ and less than 2% for the same estimate at $Re_d = 20,000$. However, if only Term II or Term III, not both, are neglected, the drag estimate would change by up to 10% at both Reynolds numbers. The combined contribution of Term II and III towards the drag of a circular cylinder operating at $Re_d = 5,600$ was quantified, for multiple streamwise locations, in Ref. [48]. The contribution of Term II and III, in Eq. 5.2, towards the total drag estimate has been shown in Fig. 5.11 based on the values reported in Ref. [48] and those found in the current study. Comparison of the total contribution from Terms II and III based solely on cross-wire measurements indicates that Term III is smaller than expected when based on Eq. 3.11. Comparing the contributions of Terms II and III found in Ref. [48] and in the current study, when pressure variation in the wake is based on pressure measurements, shows that the contribution decreases with X/d, however, it remains slightly higher in the current study. At $X/d = 40$, the magnitude of Terms II and III is approximately 1% of the drag in Ref. [48], 5% at $Re_d = 8,000$, and 2% at $Re_d = 20,000$. As no further details regarding the experimental methodology or estimated

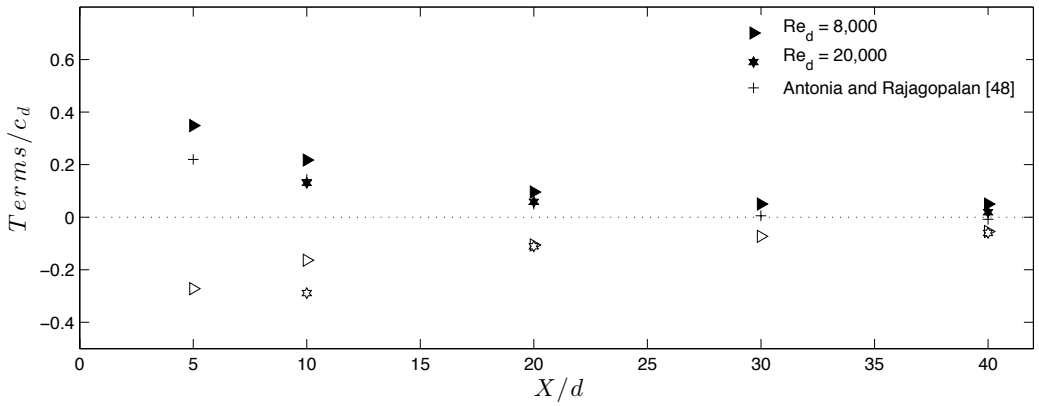

Figure 5.11: Combined contribution of Terms II and III to the total drag calculated through Eq. 5.2 in the current study compared with the findings of Ref. [48]. The pressure variation is based on static pressure measurements (solid symbols) and cross-wire measurements (hollow symbols).

error is provided in Ref. [48], these findings appear to be in reasonable agreement with the findings of the current study.

Terms I, II, and III in Fig. 5.9 and 5.10 cannot be directly compared to Terms I, II, and III in Figs. 5.5 and 5.6 since the terms are computed based on different parameters. However, a qualitative comparison reveals that the magnitudes of Terms I and III differ significantly. In van Dam's formulation, except for the drag coefficients based on profiles measured prior to $X/d = 10$, Term I is the most significant term. In the control volume formulation Term III is the most significant term at all streamwise locations investigated.

As has been determined, Eq. 3.11 cannot be used to accurately estimate the pressure variation in the wake in the current study. The same magnitude of error was introduced into the drag coefficients based on van Dam's formulation that was introduced into the complete control volume formulation based estimates by employing Eq. 3.11. Therefore, it is again concluded that static pressure variation across the wake should be measured directly.

If the measured static pressure variation is used in place of Eq. 3.11, calculations of drag coefficients are expected to contain less than 10% error, due to streamwise variation

inherent to the method, when the wake profile is measured at $X/d > 30$. In the study by Antonia and Rajagopalan [48], drag of a circular cylinder was calculated from wake profiles measured at several downstream locations. For wake profiles measured between $X/d = 5$ to 60, drag estimates varied by less than 5%, with an estimated error of approximately 4% in the drag coefficients [48]. This level of variation is lower than observed in the current study, however, the reported experimental uncertainty was also lower. As observed in the current study, the streamwise variation in drag coefficients in Ref. [48] decreases with increasing streamwise position. The drag coefficients reported in Ref. [48], confirms that drag estimates based on van Dam's formulation do vary with streamwise position of the wake profiles, however the level of variation does appear to be related to the experimental setup.

5.4 Comparison of Drag Estimate Methods

A direct comparison of the three methods used to determine the drag coefficient of the circular cylinder are shown in Fig. 5.12 for all streamwise locations investigated. The drag coefficients presented in Fig. 5.12 have all been non-dimensionalized by U_1, to match the non-dimensionalization of the reference pressure drag. The complete control volume formulation and van Dam's formulation based drag coefficients in Fig. 5.12 were calculated from cross-wire measurements and the measured static pressure variation in the wake, these results were previously presented in Figs. 5.4 and 5.8c respectively.

For both Reynolds numbers investigated, the drag coefficients based on the complete control volume formulation are within 1% of the drag coefficients based on van Dam's formulation. Thus, since van Dam's method relies on fewer experimental measurements, it is recommended that this method be selected over the complete control volume formulation for circular cylinder drag measurements. Employing the measured static pressure variation in the wake is associated with slightly higher experimental uncertainty in the drag coefficients, however, for both methods, it improves the accuracy and decreases streamwise variation in the estimates. Thus, the following discussion is limited to the results based on measure static pressure variation, presented in Fig. 5.12. However, finding an accurate

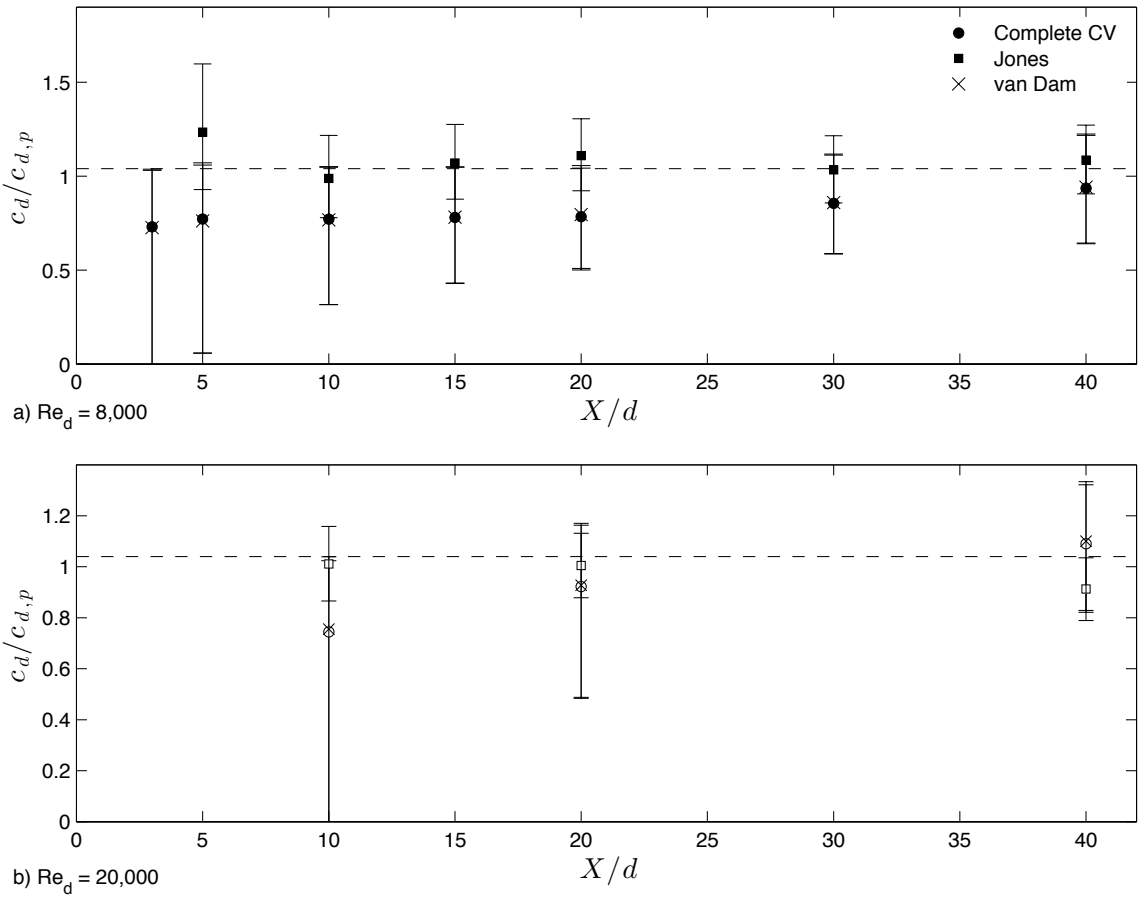

Figure 5.12: Comparison of the calculated drag coefficients based on the three methods presented above. All drag coefficients have been normalized by U_1. Static pressure variation in the wake was based on pitot-static measurements.

method of measuring the vertical velocity fluctuations in the wake to facilitate estimating the pressure variation in the wake from velocity measurements is desirable, since it reduces the experimental work necessary.

Comparing the drag coefficients calculated using Jones' method with those based on van Dam's and the complete control volume formulation reveals the different patterns of streamwise variation that exist. At $X/d > 10$, drag coefficients based on Jones' formulation

vary randomly within the estimated experimental uncertainty. In contrast, the velocity based drag estimates (van Dam's and the complete control volume formulation) continually increase, but at a diminishing rate, with streamwise position. Additionally, the estimated uncertainty in drag coefficients from Jones' method, downstream of $X/d = 10$, remains approximately constant, while for the velocity based estimates, uncertainty decreases with increasing streamwise position.

Prior to discussing recommendations for implementing these techniques, it is helpful to examine the drag coefficients used as reference values. Table 5.2 lists the pressure based drag coefficients measured during the current investigation and several published drag coefficients for circular cylinders operating under the same flow conditions. The pressure based drag coefficient in the current study has an estimated uncertainty of less than 5% at $Re_d = 8,000$ and less than 3.5% at $Re_d = 20,000$. The published drag coefficients, for the same conditions, differ between references to a greater degree than predicted by the experimental uncertainty in the present study. While it is assumed the differences are a result of specific experimental conditions, such as blockage, freestream turbulence levels, and model aspect ratio, it is reasonable to conclude that some of the variation observed is due to the measurement technique employed and the implementation of the method used to calculate drag. This variation in published results is considered when discussing the reliability of the drag techniques investigated.

Based on the findings in this study, if wake profiles are measured between $X/d = 10$ and 30, it is recommended to employ Jones' formulation to calculate the coefficient of drag. If wake profiles are measured father than $X/d = 30$ downstream from the cylinder, any of the three methods investigated in this study can be applied, however, Jones' formulation is the preferred method. Jones' method is recommended for profiles measured upstream of $X/d = 30$ since drag estimates based on van Dam's method fall below the reference pressure drag value and are also, predominantly, outside the range of drag coefficients presented in Table 5.2. Jones' method is still recommended downstream of $X/d = 30$, where the three methods provide approximately equivalent estimates of the drag coefficient, since, in general, it is the most robust method.

When employing Jones' method, the freestream reference pressure needs to be measured

Table 5.2: Drag coefficient and Reynolds number of the cylinder data references.

Experiment	Re_d	c_d	Experimental Technique
Current Study	$8,000$	1.22	surface pressure
Cantwell and Coles [64]	$8,000$	0.9 - 1.23	-*
Dryden and Heald [76]	$8,000$	1.07 - 1.15	force balance
Norberg [61]	$8,020$	1.14	surface pressure
Current Study	$20,000$	1.35	surface pressure
Achenbach [35]	$20,000$	1.02 - 1.17	surface pressure and skin friction
Dryden and Heald [76]	$20,000$	1.09 - 1.22	force balance
Lim & Lee [77]	$20,000$	1.08	force balance
Nakamura [78]	$20,900$	1.32	surface pressure

*no technique specified

in the outer flow at the location of the the wake profile measurement. To employ the complete control volume formulation, it is necessary to measure the upstream velocity, and outer flow velocity at the location of the wake profile in addition to the wake profile. The contribution due to pressure acting on boundaries 2 and 3 was negligible in the current study, it is therefore necessary to only measure the total change in outer flow velocity between boundaries 1 and 4 and not the streamwise variation along the length of the control volume. The reference velocity for van Dam's method should be measured in the outer flow at the location of wake profile measurement. It may be possible to neglect Terms II and III in Eq. 5.2 if measurements are taken at $X/d = 40$ or farther downstream, however, the terms should not be neglected independently.

Chapter 6

Airfoil Drag Estimates

Applying the findings from the previous chapter, the same drag formulations will be employed to calculate the drag of a NACA 0018 airfoil operating at a chord Reynolds number of $100,000$. With the current experimental setup, it was not possible to accurately measure the drag through an alternative method, e.g. a force balance. Therefore, drag coefficients reported in this section have not been normalized. Instead published drag data, for the NACA 0018 airfoil, are included for comparison. In a study by Heerenbrink [79], airfoil drag was measured via a force balance for chord Reynolds numbers of $80,000$ and $110,000$. The second set of comparison data employed, is reported by Sheldahl and Klimas [80] for $Re_c = 80,000$. In this study the drag data was determined from numerical simulations based on experimental measurements [80]. A summary of the reference drag data is listed in Table 6.1, along with the line designation used in all figures in this chapter.

Comparing the the data in Table 6.1 reveals a notable disparity between the reported values. Even though drag coefficients are expected to decrease with increasing Reynolds number for $80,000 \leq Re_c \leq 110,000$ [79,80], the drag coefficients from Ref. [80] for $Re_c = 80,000$ are lower than those in Ref. [79] for for $Re_c = 110,000$. These differences are likely due to differences in the experimental conditions, especially since low Reynolds number airfoil operation is sensitive to experimental conditions, and to the different techniques employed to estimate drag. Thus, the values reported from these studies are expected to differ from the results in this study and are only employed for general comparison. The

Table 6.1: Drag coefficient and Reynolds number of the NACA 0018 airfoil reference data.

Source	Re_c	$\alpha(^\circ)$	c_d	Measurement Technique	Line Type
Sheldahl and Kilmas [80]	80,000	0	0.016	numerical model based on experimental data	dashes & dots
		5	0.019		
		10	0.029		
		15	0.18		
Heerenbrink [79]	80,000	0	0.029	force balance	dotted
		5	0.043		
		10	0.060		
Heerenbrink [79]	110,000	0	0.020	force balance	dashed
		5	0.030		
		10	0.0588		

study by Heerenbrink [79] did not include post-stall angles of attack, and, therefore, only a single comparison point is available at $\alpha = 15^\circ$. However, it is assumed that the variation in drag coefficients, measured in different facilities, will be similar at $\alpha = 15^\circ$ to that observed for lower angles of attack.

The drag estimates are calculated from wake profiles measured at four downstream locations, specifically $x/c = 1$, 2, 3, and 4.5. Three angles of attack were investigated, $\alpha = 5^\circ$, 10°, and 15°, spanning the two flow regimes common to low Reynolds number airfoil operation [14]. At $\alpha = 5^\circ$ and 10°, a separation bubble forms over the upper surface of the airfoil, and, at $\alpha = 15^\circ$, the flow separates without reattachment. Drag calculations were not preformed for $\alpha = 0^\circ$ since the flow development is sensitive to model imperfections [17]. Details regarding the flow development, and the measured wake profiles for $\alpha = 10^\circ$ and 15°, are included in Chapter 4. Profiles measured in the wake of the airfoil operating at $\alpha = 5^\circ$ are provided in Appendix D. The error bars on the computed drag coefficients are based on estimated measurement uncertainty and do not include the contributions from inherent errors associated with a given methodology employed for estimating the drag force. The details of the uncertainty calculations are given in Appendix A. The normalization velocity used for all drag coefficients presented in this chapter is U_1, the upstream velocity

in the test section, to permit direct comparison of the drag coefficient calculated from the different methods.

6.1 Control Volume Drag Estimates

Drag coefficients calculated from Eq. 3.13, referred to as the complete control volume formulation, are shown in Fig. 6.1. The solid symbols in Fig. 6.1 represent the drag estimates based solely on cross-wire velocity measurements and the hollow symbols indicate the drag coefficients calculated from the measured static pressure variation in the wake and cross-wire velocity measurements. The initial discussion focuses on the drag estimates based solely on cross-wire measurements, i.e. calculations where wake static pressure variation was predicted by Eq. 3.11. The calculated drag coefficients fall within the variation seen between the reported values from Refs. [79] and [80] when the airfoil is operating with the flow attached at the trailing edge. When the airfoil is stalled, $\alpha = 15°$, the predicted drag is significantly higher than the value reported in Ref. [80], but is within the expected variation between sources. As was observed in the complete control volume drag estimates for the circular cylinder, the calculated drag coefficients vary with streamwise location. This is true for all three angles investigated. However, the pattern in streamwise variation is not as easily identified in the airfoil drag coefficients. For the attached flow case, while the variation in drag coefficient diminishes with streamwise position, the calculated drag coefficient appears to fluctuate at random. It is unclear if the variation in the drag coefficients for the stalled airfoil follows a streamwise trend. Without a firm reference value for the drag coefficient, it is difficult to assess the validity of the results shown in Fig. 6.1. However, since the drag estimates are not expected to vary with streamwise position of the wake profile, based on the theoretical formulation of the method, the sources of the variation shall be investigated.

The analysis of the circular cylinder results was used as a guide for the airfoil investigation. Since the method used to predict the static pressure variation in the wake was found to introduce a significant degree of error into the cylinder drag calculations this was the first assumption verified for the airfoil calculations. Though, for the airfoil, analysis of the

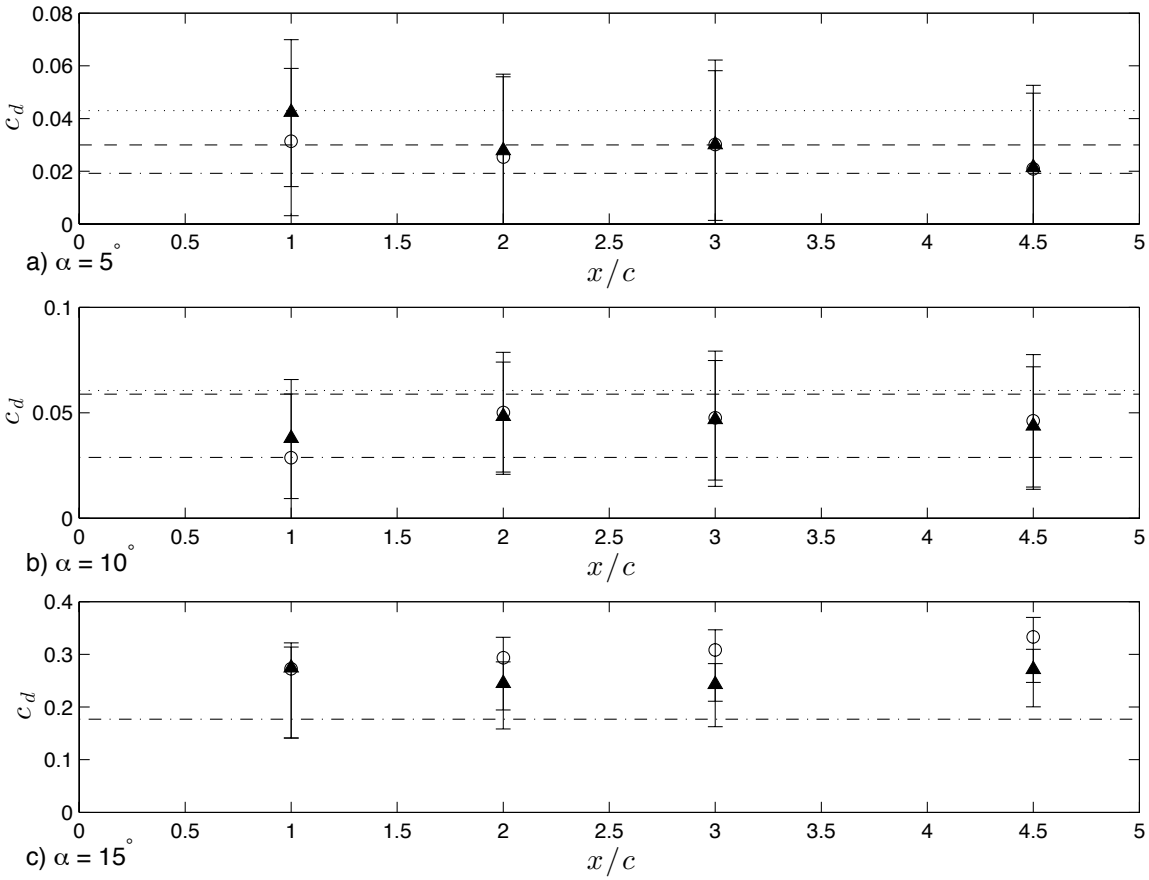

Figure 6.1: Calculated drag coefficients for the NACA 0018 airfoil at three angles of attack; a) $\alpha = 5°$, b) $\alpha = 10°$, and c) $\alpha = 15°$. Solid markers display the estimate of drag coefficient based solely on cross-wire measurements in the wake. Unfilled markers display the results of the calculations where static pressure variation in the wake was based on the measured variation. Comparison data points indicated by the dashed and dotted line, and dotted line are for the airfoil operating at $Re_d = 80,000$ from Refs. [80] and [79], respectively. The dashed line indicates the drag coefficient at $Re_d = 110,000$ from Ref. [79].

wake measurements did not reveal the vertical velocity to be under-predicted by the cross-wire measurement technique employed. To check the validity of the predicted pressure variation, the maximum static pressure predicted by Eq. 3.11 was compared against the maximum measured static pressure deficit. The results of this comparison are displayed

graphically in Fig. 6.2. For all three angles, Fig. 6.2 indicates that the pressure variation in the wake is likely under estimated by employing Eq. 3.11. The discrepancy between the predicted and measured static pressure deficit decreases with increasing streamwise position. The same discrepancy between predicted and measured maximum static pressure deficit was found in the wake of the circular cylinder and, there too, the difference diminished with increasing streamwise distance (see Fig. 5.3).

To determine what effect the error in the predicted static pressure variation has on the drag estimates, drag coefficients were recalculated using the measured static pressure variation. The recalculated drag coefficients are shown in Fig. 6.1 by the hollow symbols.

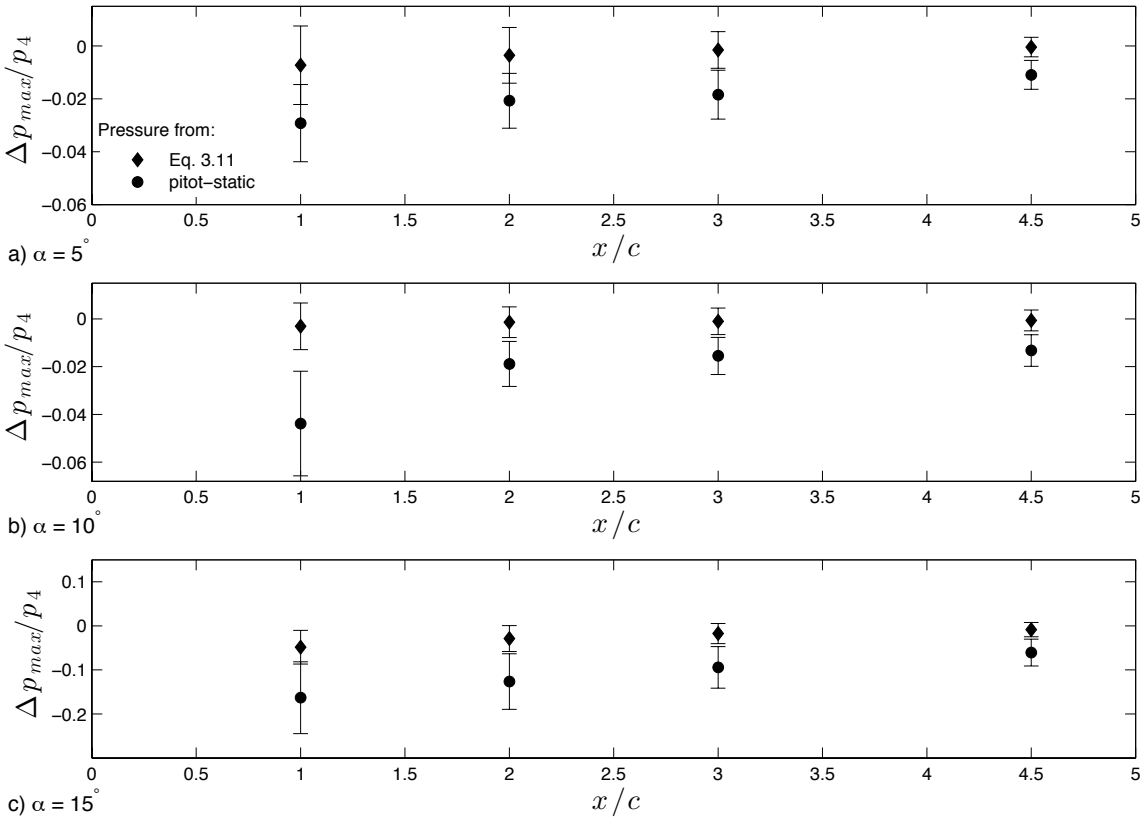

Figure 6.2: Comparison of the maximum static pressure deficit in the wake based on the pressure variation predicted by Eq. 3.11 and the measured static pressure profile.

Except at $x/c = 1$ and 2, for $\alpha = 15°$, the change in drag coefficient follows the trend expected from Fig. 6.2. For the angles of attack at which flow is attached at the trailing edge, the error due to Eq. 3.11 is greatest at $x/c = 1$, and diminishes with increasing streamwise position. When the airfoil is stalled, the change, due to calculating the pressure variation from Eq. 3.11, diminishes with streamwise position for $x/c > 2$. However, for $x/c \leq 2$ the percent change in drag coefficient is smaller than that observed farther downstream. This is visible at $x/c = 1$ in Fig. 6.1, where the drag coefficient changes less than 2%. The explanation for this difference is found in the static pressure profiles, shown in Fig. 4.34. At $x/c = 1$ and, to a lesser extent, at $x/c = 2$, the static pressure increases outside the deficit region before decreasing to freestream values. Since the static pressure variation is integrated to calculate the contribution to drag, these regions of increased static pressure negate the effect of under-predicting the static pressure deficit by Eq. 3.11. An increase in static pressure variation is also observed in the static pressure profile for $\alpha = 10°$ at $x/c = 1$ (Fig. 4.32), but it is significantly smaller in magnitude and extent. The streamwise variation in drag estimates for $\alpha = 15°$ is decreased by employing the measured pressure variation. At $\alpha = 5°$ and $10°$ (for $x/c > 1$), the streamwise variation also appears to be decreased, however, the estimated uncertainty increases significantly. Therefore, no firm conclusion can be drawn regarding the overall variation.

The uncertainty in the drag coefficients, due to that in measured and calculated quantities, is represented by the error bars in Fig. 6.1. For both sets of drag estimates, the experimental uncertainty remains approximately constant with streamwise position. When the flow is attached at the trailing edge, $\alpha = 5°$ and $10°$, the experimental uncertainty could account for the observed streamwise variation. However, at $\alpha = 15°$, the streamwise variation exceeds that expected solely from uncertainty estimates. This suggests that all causes of streamwise variation may not yet have been identified. Since relying on Eq. 3.11 in the current study was shown to introduce significant error into the drag estimates for the circular cylinder and for the airfoil operating at $\alpha = 15°$, the drag coefficients based on the measured static pressure variation will be the focus of the investigation for all three angles of attack.

To determine if the streamwise variation can be attributed to any of the remaining as-

sumptions employed in deriving Eq. 3.13, the contribution from pressure acting on boundaries 2 and 3 and the contribution from viscous stresses was estimated. The methods used to approximate these terms are detailed in Chapter 5 for the circular cylinder. Including an approximation of the contribution from the pressure variation along boundaries 2 and 3 in the drag calculations results in an approximate change of 2% at $x/c = 1$ for all angles. However, for $x/c > 1$, the drag coefficients change by less than 1%. Therefore, the pressure contribution is negligible under these conditions and does not appreciably contribute to the observed streamwise variation. The contribution from viscous stresses is estimated to be less than 0.01% of the total drag at all streamwise locations and angles of attack investigated. Based on this finding, it is concluded that viscous stresses are negligible and do not contribute towards the streamwise variation.

The significance of the individual terms in Eq. 3.13 to the drag calculation is illustrated in Figs. 6.3a, 6.3b, and 6.3c for $\alpha = 5°$, $10°$, and $15°$ respectively. In all three plots, the individual terms have been normalized by the calculated drag coefficient at the given streamwise position, and estimates of experimental uncertainty have been omitted for clarity. As noted for the circular cylinder, Terms I and III display opposite trends. Using a similar approach to measure the drag of an airfoil from PIV flow measurements, van Oudheusden et al. [12] noted that Term III had a more significant contribution than Term I to the total drag coefficient, which is also observed here. For $\alpha = 5°$ and $10°$, Term II is a relatively small term at all streamwise positions, neglecting this term would change the drag estimates by less than 5%. In Ref. [12], this term was found to be similarly insignificant. Term II is more significant for the stalled airfoil, at $x/c = 4.5$, where the term is the lowest, it is approximately 10% of the drag coefficient. Overall, none of the terms can be neglected from Eq. 3.13.

For non-zero angles of attack, the outer flow in the test section and wake are not symmetric about the centreline. This can be observed in the pressure variation measured along the upper and lower test section walls, and corresponding outer flow velocity variation, presented in Figs. 4.17 and 4.18, respectively. This was incorporated into the drag estimates by calculating the upstream flow conditions in the upper and lower sections of the test section independently, and employing a linear fit to create the velocity and

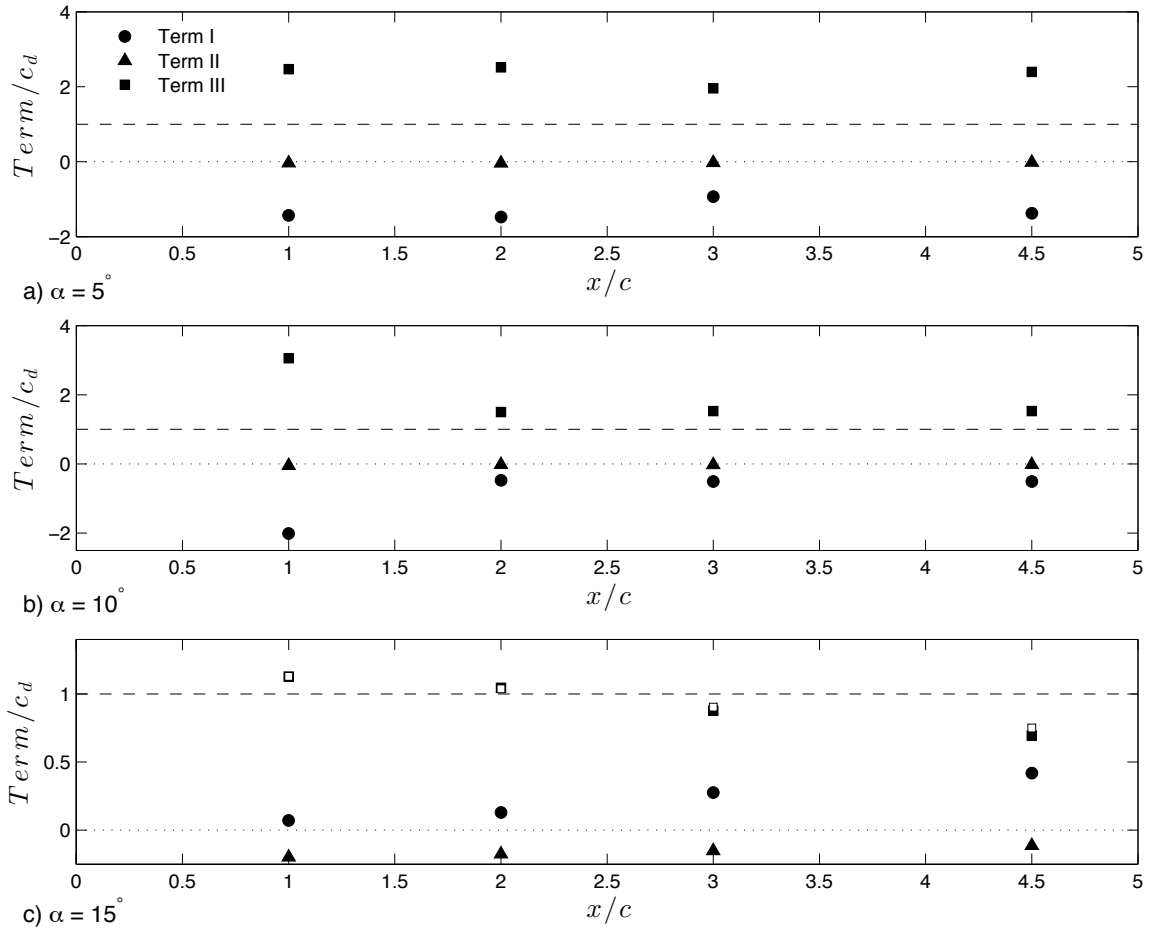

Figure 6.3: Contribution of the individual terms in Eq. 3.13 to total calculated drag, where; Term I is the contribution due to rate of change of linear momentum in the control volume, Term II the contribution due to Reynolds and viscous stresses acting on the boundaries, and Term III the drag contribution due to pressure acting on the control volume surface. Solid markers indicate terms calculated from cross-wire measurements and unfilled symbols those based on pitot-static tube measurements. Values are shown normalized by the calculated drag coefficient at the streamwise position of the estimate.

pressure profiles at boundary 1. In van Dam's formulation the upstream properties are constant, thereby averaging the asymmetric outer flow properties. To determine the effect a similar approach would have on the complete control volume based drag estimates, drag

calculations were based on the average properties in the upper and lower outer flows. The drag estimates most affected by averaging asymmetric flow parameters were those based on profiles measured at $x/c = 1$, at this location drag coefficients changed between 2% and 5%. At locations farther downstream, drag estimates were altered by less than 1%. Therefore, it is assumed that averaging the asymmetry in outer flow properties will not introduce significant error into van Dam's method.

When the flow is attached at the trailing edge of the airfoil, the streamwise variation is within the estimated uncertainty in drag coefficients, however, the variation does appear to decrease with increasing streamwise position. For $\alpha = 5^\circ$ calculated drag coefficients vary by approximately 25% downstream of $x/d = 1$, and for $\alpha = 10^\circ$ streamwise variation is less than 10% for $x/c \geq 3$. Although the variation is within the estimated uncertainty, it is still recommended to measure wake profiles at $x/c > 3$ due to decreasing variation in the estimate with increasing x/c. When the airfoil is stalled, $\alpha = 15^\circ$, the streamwise variation of the estimated drag coefficients is similar to that observed in the circular cylinder cases. Since the accuracy of the complete control volume formulation was found to increase with streamwise distance for the circular cylinder and the streamwise variation is within the uncertainty bounds for $x/c \geq 3$, it is recommended that the wake profiles be measured at $x/c > 3$ for a stalled airfoil. Therefore, regardless of flow development over the airfoil, the complete control volume formulation should be based on wake profiles measured farther than 3 chord lengths downstream from the trailing edge.

6.2 Drag Estimates Based on Jones' Methods

Drag coefficients calculated using Jones' equation, Eq. 5.1, are shown in Fig. 6.4. Based on the finding for the circular cylinder, the reference pressure (G_∞) was based on the outer flow measurements in the wake profile. At $\alpha = 5^\circ$ and 10°, the drag estimates fall within the general range of the comparison data, when based on profiles measured at $x/c > 1$. The streamwise variation is similar to that observed in Jones' based estimates for the circular cylinder; the variation appears random with streamwise position for $x/c \geq 2$ and is within the experimental uncertainty. For the stalled airfoil case, the drag estimates, again

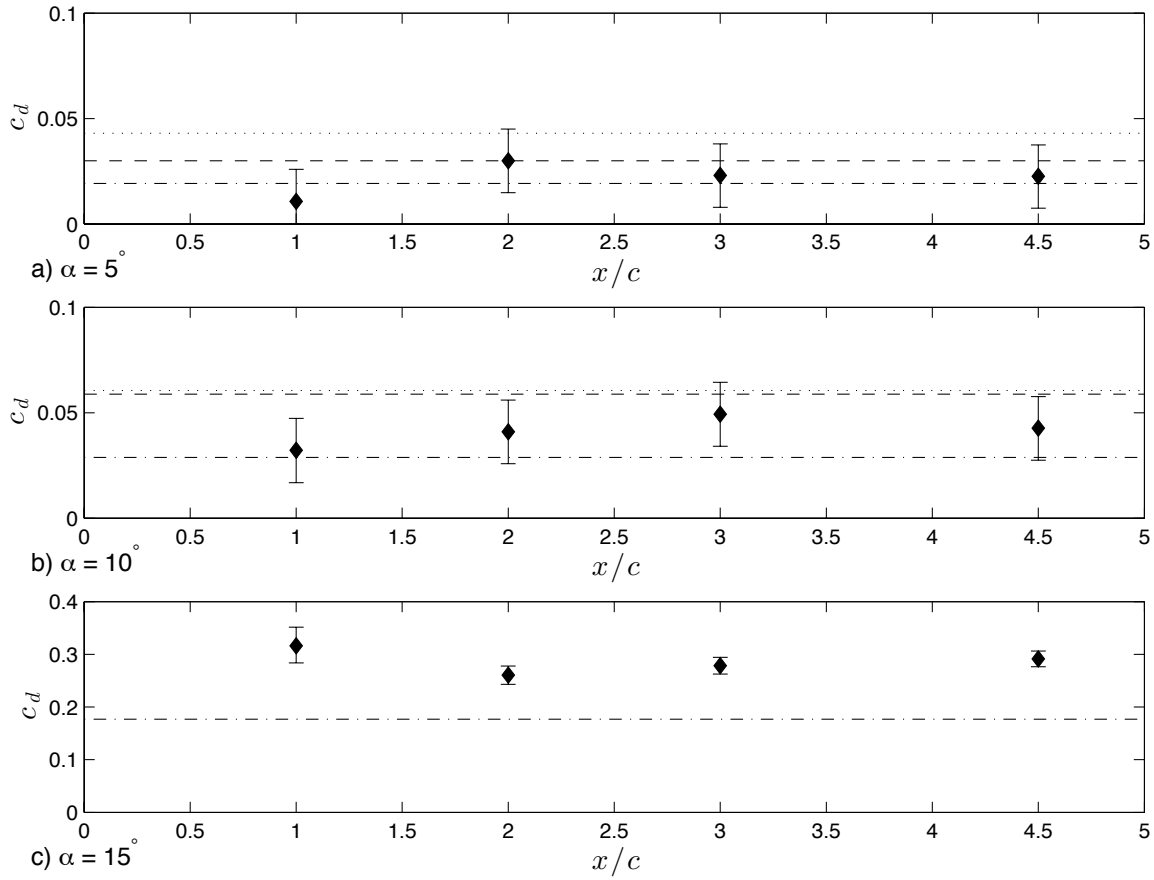

Figure 6.4: Drag coefficients, based on Jone's method, for the NACA 0018 airfoil at three angles of attack; a) $\alpha = 5°$, b) $\alpha = 10°$, and c) $\alpha = 15°$. Comparison data points indicated by the dashed and dotted line, and dotted line are for the airfoil operating at $Re_d = 80,000$ from Refs. [80] and [79], respectively. The dashed line indicates the drag coefficient at $Re_d = 110,000$ from Ref. [79].

vary with streamwise position, however, the variation appears to diminish with increasing streamwise distance. For all three angles, the estimated uncertainty is highest at $x/c = 1$, diminishes downstream of this point but then remains relatively constant.

A source of error was introduced in the airfoil calculations that was not present in the cylinder calculations. Jones' formulation requires measurements to be taken along a

plane perpendicular to the flow [10]. On the average, this was possible in the wake of the circular cylinder, since regions of flow angularity are localized. However, for the airfoil, wake profiles were measured perpendicular to the freestream flow direction. In the wake, as indicated by the downward migration of the velocity deficit region observed in the wake profiles (see Fig. 4.20 and 4.24), the measurement plane is no longer perpendicular to the flow angle. However, the flow angles are still relatively small and should, consequently, have a negligible effect on flow measurements. The effect was confirmed to be negligible by determining flow angle from cross-wire measurements and quantifying the integral effect on drag calculations. Drag coefficients were estimated to change by less than 2% due to flow angle, well within the bounds of experimental uncertainty.

The calculated drag coefficients indicate that Jones' method is suitable for wake profiles measured more than one chord length from the trailing edge of the airfoil. The relatively high estimated experimental uncertainty in the drag coefficients for attached flow experiments is due to the relatively low flow velocities and the narrow wake.

6.3 Drag Estimates Based on van Dam's Formulation

Airfoil drag coefficients based on van Dam's formulation are shown in Fig. 6.5. Based on the findings for the circular cylinder the reference velocity, U_∞, was based on wake profile measurements in the outer flow. The van Dam's based estimates appear to be similar to the estimates based on the complete control volume formulation, this was also found to be the case for the circular cylinder. Therefore, they will only be briefly elaborated on here. Looking first at the drag coefficient based solely on cross-wire measurements, the drag estimates vary with streamwise position at all angles of attack. The estimates for $\alpha = 5^\circ$ and 10° fall within the general range of the drag coefficient from different sources. At $\alpha = 15^\circ$, values of drag are greater that from Ref. [80]. Accounting for the error introduced by Eq. 3.11, results in the same change in drag estimates as observed previously for the estimates based on the complete control volume formulation. Drag estimates for $\alpha = 15^\circ$ are the most significantly affected by accounting for the error introduced through Eq. 3.11.

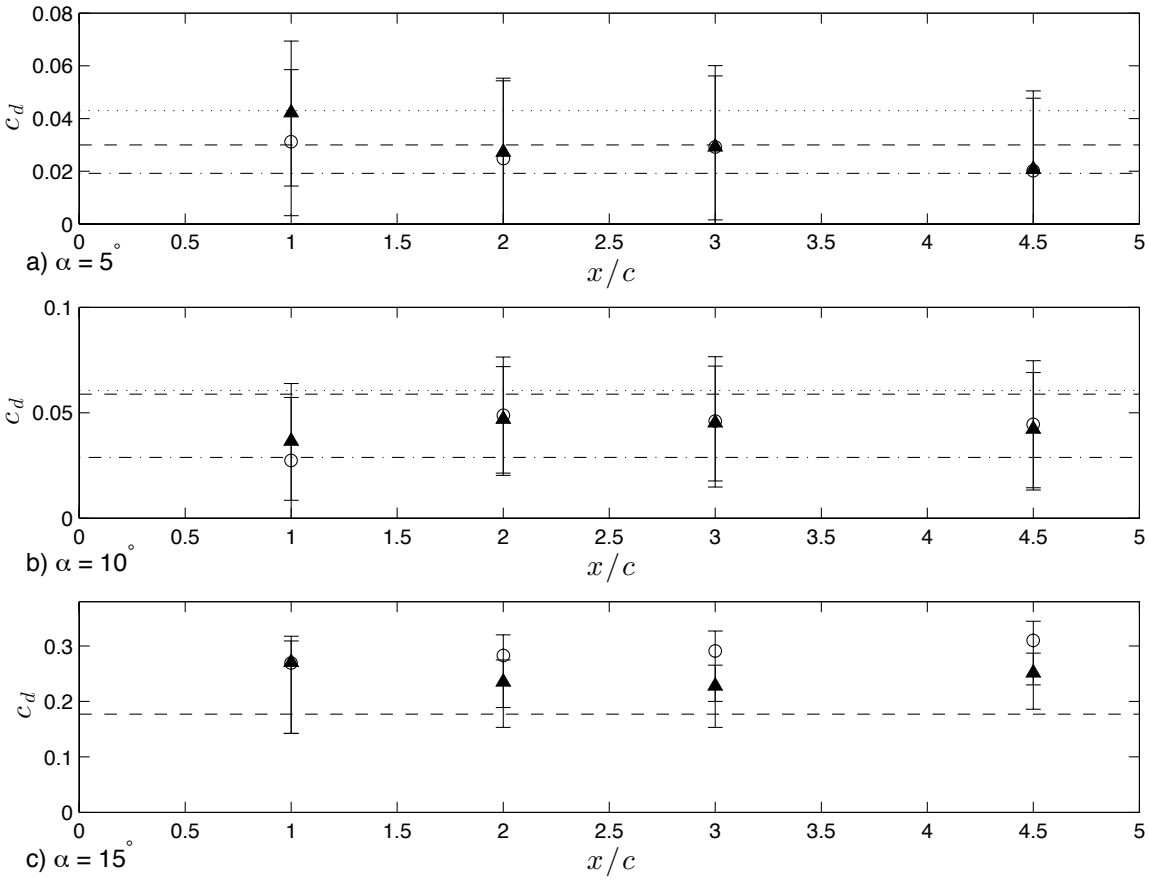

Figure 6.5: Drag coefficients based on van Dam's method, for three angles of attack; a) $\alpha = 5°$, b) $\alpha = 10°$, and c) $\alpha = 15°$. Solid markers display the estimate of drag coefficient based solely on cross-wire measurements in the wake. Hollow markers display the results of the calculations where static pressure variation in the wake was based on the measured variation. Comparison data points indicated by the dashed and dotted line, and dotted line are for the airfoil operating at $Re_d = 80,000$ from Refs. [80] and [79], respectively. The dashed line indicates the drag coefficient at $Re_d = 110,000$ from Ref. [79].

Similar to the complete control volume formulation the measured static pressure variation shall be employed for drag calculations, for all three angles of attack.

A breakdown of the terms in Eq. 5.2 is shown in Figs. 6.6a, 6.6b, and 6.6c for $\alpha = 5°$, $10°$, and $15°$, respectively. For all three angles of attack, the largest contribution is from Term

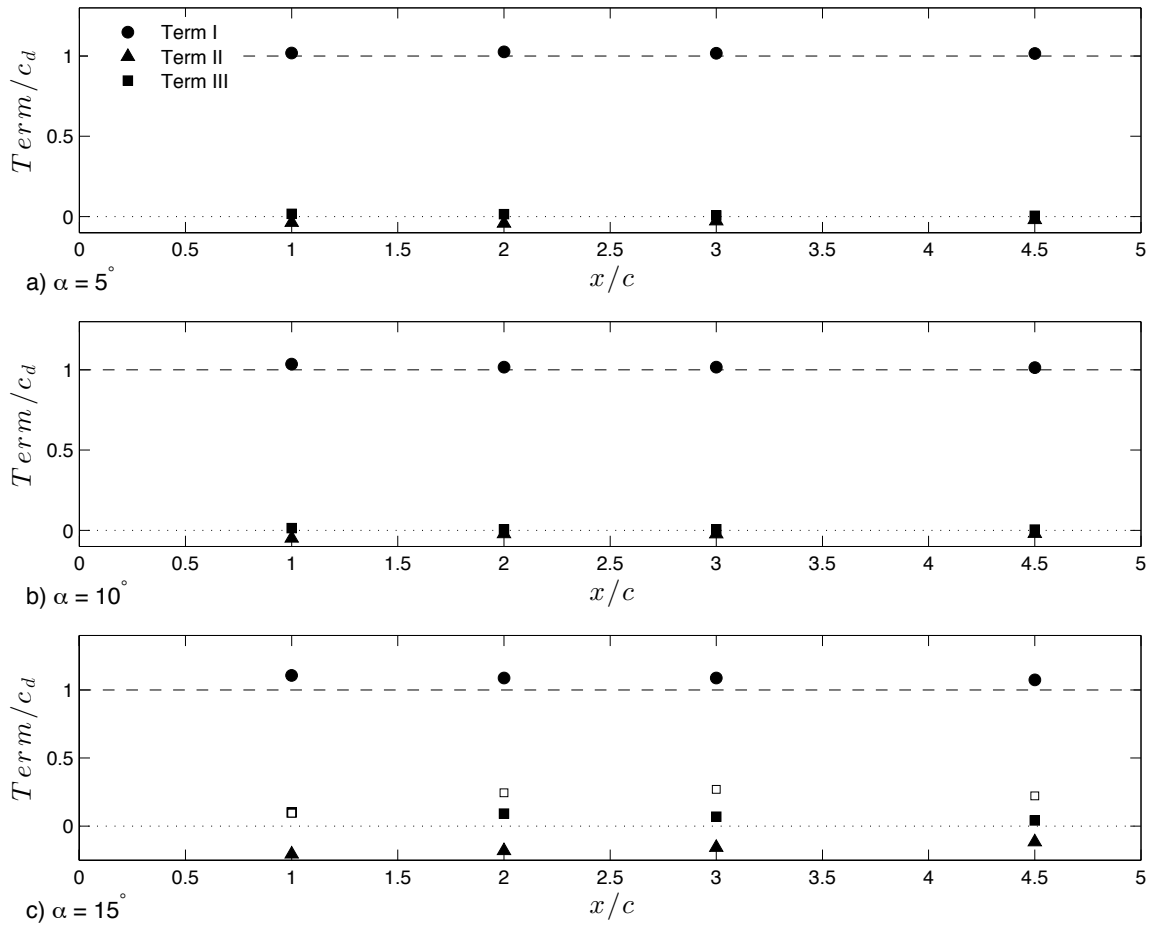

Figure 6.6: Contribution of the individual terms in Eq. 5.2 to total calculated. Values are shown normalized by the calculated drag coefficient at the streamwise position of the estimate.

I, similar to the circular cylinder results. Terms II and III are both relatively minor terms in the drag calculations when the flow is attached at the trailing edge; for profiles measured at $x/c > 2$, the individual contribution of both terms does not exceed 5% of the total drag coefficient. At $\alpha = 15°$, all three terms are significant. Figure 6.6c also highlights the increasing magnitude of Term III with streamwise position, when based on the measured static pressure variation. Unlike in the circular cylinder study, the contribution from Terms

II and III remains significant at all streamwise locations investigated. Though the terms in Eq. 5.2 cannot be compared quantitatively with those in Eq. 3.13, a general comparison can be made. In the case of attached flow at the trailing edge ($\alpha = 5^\circ$ and 10°), Term III is small in van Dam's formulation, this is not the case in the complete control volume formulation. This was also found in the comparison of terms, between methods, for circular cylinder.

Drag estimates, of the airfoil operating under conditions where the flow is attached at the trailing edge, can rely on Eq. 3.11 to predict the static pressure variation in the wake for profiles measured downstream of $x/c = 2$. For $\alpha = 5^\circ$ and 10° , the cases where flow is attached at the trailing edge, the streamwise variation is within uncertainty bounds but does diminish with streamwise distance. For $\alpha = 15^\circ$, the streamwise variation is within uncertainty bounds for drag coefficients based on wake profiles measured at $x/c = 3$, or farther downstream. As such it is recommended to measure wake profiles, for the purpose of calculating drag, at $x/c \geq 3$ for all angles of attack.

6.4 Comparison of Drag Estimate Methods

The drag coefficients, based on the three methods investigated, are compared in this section. A direct comparison of the drag coefficients calculated from the three methods is shown in Figs. 6.7, 6.8, and 6.9 for $\alpha = 5^\circ$, 10°, and 15°, respectively. The results, as a whole, show that all three methods contain similar levels of streamwise variation, and the agreement between methods increases as streamwise distance increases.

A study, conducted on a NACA 642A015 airfoil by van Oudheusden et al. [12], examined the accuracy of drag estimates based on PIV flow field measurements. The PIV based drag estimates were calculated through two methods, (i) a contour integral approach, similar to the complete control volume formulation, and (ii) a wake integral approach, similar to van Dam's formulation [12]. Uncertainty in the drag estimates was determined by varying the contour length and the location of wake profile measurement, and it was determined that both methods exhibited sensitivity to measurement location [12]. The variation due to streamwise position was affected by Reynolds number, angle of attack, and method of

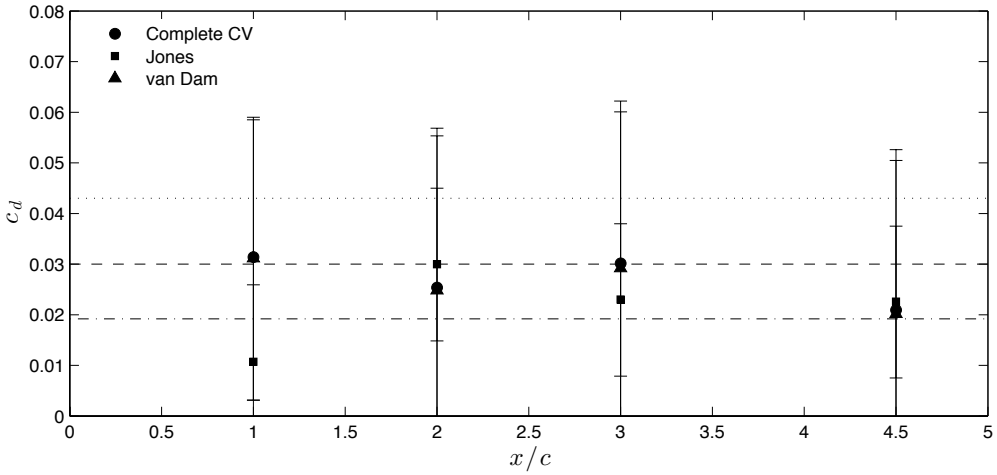

Figure 6.7: Comparison of the three methods employed to calculated drag coefficient based on wake profiles measured behind the airfoil operating at $\alpha = 5°$. Comparison data points indicated by the dashed and dotted line, and dotted line are for the airfoil operating at $Re_d = 80,000$ from Refs. [80] and [79], respectively. The dashed line indicates the drag coefficient at $Re_d = 110,000$ from Ref. [79].

calculating drag [12]. The streamwise variation in the drag estimates seen in Ref. [12] increases when the airfoil is operating under stalled conditions, as observed in the current study. Streamwise variation also increased with decreasing Reynolds number, the highest variation was observed at the lowest Reynolds number investigated, 100,000, presumably due to increased experimental uncertainty [12]. The streamwise variation observed in Ref. [12] cannot be compared directly since the downstream regions investigated differ greatly, however, the results support the current work.

For the circular cylinder, estimating drag based on van Dam's and the complete control volume formulations resulted in estimates within 1% of each other. Comparing the same drag estimates for the airfoil reveals that, when flow is attached at the trailing edge, drag estimates are within 2% for measurements taken at $x/c > 2$. The drag estimates measured at $x/c < 2$ differ by up to 4%. The observed variation is equivalent to that observed when, for an asymmetric wake, an average outer flow velocity is used in the complete control volume formulation. Therefore, the discrepancy is attributed to the difference in

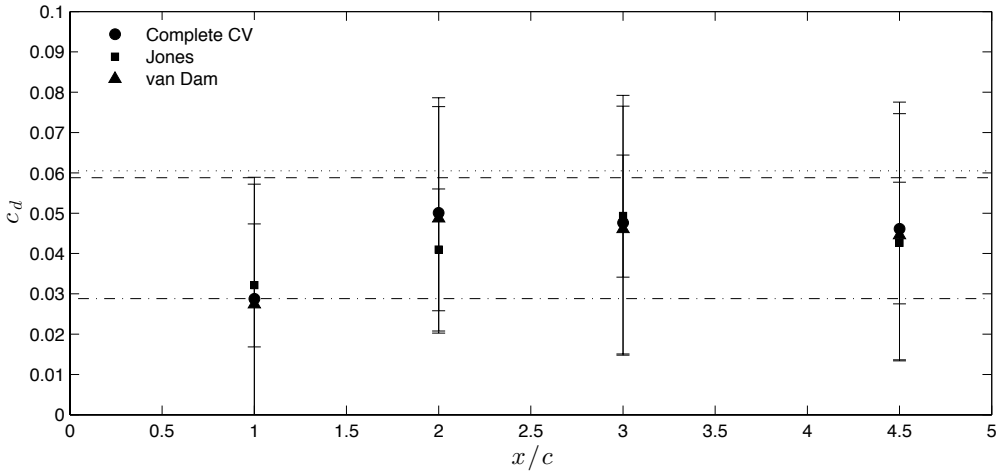

Figure 6.8: Comparison of the three methods employed to calculated drag coefficient based on wake profiles measured behind the airfoil operating at $\alpha = 10°$. Comparison data points indicated by the dashed and dotted line, and dotted line are for the airfoil operating at $Re_d = 80,000$ from Refs. [80] and [79], respectively. The dashed line indicates the drag coefficient at $Re_d = 110,000$ from Ref. [79].

the outer flow conditions above and below the velocity deficit region. However, since flow asymmetry decreases with streamwise distance, it is recommended to use wake profiles measured at $x/c > 3$ for either method. At this $x/c > 3$, the difference between the complete control volume drag estimate and the van Dam's estimate is negligible. For the stalled airfoil, the drag estimates from van Dam's formulation and the complete control volume formulation differed by less than 7%. This level of discrepancy is well within the experimental uncertainty. Due to these reasons it is recommended to employ van Dam's formulation to measure drag at all angles of attack, as it requires fewer experimental measurements.

Comparing van Dam's and the complete control volume formulation based drag coefficients with those based on Jones' method reveals that the differences in estimated value decrease with increasing streamwise position. For all angles of attack, the differences between the three drag estimates are less than 10% at $x/c = 4.5$, which is within the estimated uncertainty for the three methods used to calculate drag. Since the relative uncertainty

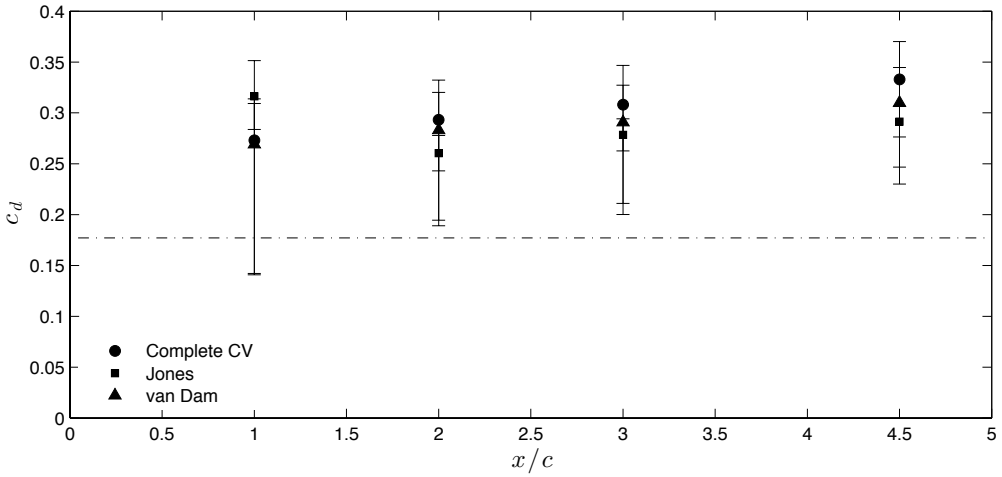

Figure 6.9: Comparison of the three methods employed to calculated drag coefficient based on wake profiles measured behind the airfoil operating at $\alpha = 15°$. Comparison data indicated by the dashed and dotted line is the the drag coefficient at $Re_d = 80,000$ from Ref. [80].

is similar for all three methods, it is recommended to rely on Jones' method to calculate drag estimates regardless of flow development. Overall, Jones' method appears to be the most robust.

Chapter 7

Conclusions

The main goal of this study was to identify a reliable method of measuring the drag of a body based on flow field measurements. To accomplish this, three methods of calculating drag were investigated; specifically, (i) the complete control volume formulation, (ii) Jones' formulation [10], and (iii) van Dam's formulation [5]. To apply these methods, detailed wake velocity and pressure measurements were conducted for a circular cylinder and an airfoil. In conjunction with the wake profiles, variation of the outer flow in the wind tunnel was measured through wall static pressure measurements. Based on the measured profiles, drag coefficients were calculated for each set of experimental conditions. Assumptions associated with each drag estimation method were verified against measured data when possible and the specific details of implementation were investigated. The resulting drag coefficients were compared and contrasted to identify the optimal methodology, implementation, and guidelines for measuring drag in each experimental flow examined.

7.1 Wake Development

Velocity and pressure profiles were measured in the wake of a circular cylinder operating at $Re_d = 8,000$ and $20,000$, and a NACA 0018 airfoil operating at $Re_c = 100,000$ and three angles of attack, 5°, 10°, and 15°. The flow characteristics detailed through wake profiles included the total and static pressure, and mean and RMS fluctuating components of the

streamwise and vertical velocities. Velocity measurements were taken with a cross-wire constant temperature anemometry probe, and pressure profiles were measured through a pitot-static tube and a three-hole probe.

Profiles were measured between 3 to 40 diameters downstream from the circular cylinder. The wake profiles indicated classical turbulent wake development. From the perspective of flow field drag calculations, the circular cylinder wake profiles revealed the static pressure in the wake does not recover to freestream values by $X/d = 40$, the farthest downstream location considered here. Additionally, the RMS fluctuating components of velocity in the cylinder wake are still appreciable at $X/d = 40$. The range of experimental conditions selected for the airfoil experiments permitted the two flow regimes common to low Reynolds number airfoil operation to be studied. Measurements were conducted in the wake between 1 and 4.5 chord lengths from the trailing edge. As expected, the wake of the airfoil operating with attached flow at the trailing edge was found to be narrower than the wake of the airfoil operating under separated flow conditions.

In the wake of the circular cylinder the comparison of the pressure profiles measured via a pitot-static tube and a three-hole probe revealed that the two methods result in different static pressure values up to $X/d = 20$. The inherently larger physical size of the three-hole probe leads to notably higher adverse effects on measurements in regions of higher spatial pressure gradients. Such conditions exist in the wake of the cylinder up to $X/d = 20$. Through comparison with cross-wire measurements, the pitot-static tube was shown to produce accurate measurements of total and static pressure, except immediately downstream of the recirculation region, $X/d = 3$ at $Re_d = 8,000$.

7.2 Drag Measurements

The estimates of drag coefficient based on all three methods investigated exhibited significant variation with streamwise position of the wake profile measurement. In general, the observed variation decreased with increasing streamwise distance. For drag estimates based on Jones' method, the variation between estimates decreased significantly when profiles were measured farther than 10 times the frontal height of the body downstream.

Beyond that point, the streamwise variation appeared to remain relatively constant. When calculated through Jones' method using profiles at $3 \leq X/d \leq 40$, drag estimates varied within approximately 15% of the pressure based drag coefficient. When Jones' method was used to estimate the drag of the airfoil based on wake profiles measured at $1 \leq x/c \leq 4.5$ streamwise variation in the estimates was up to 50% of the drag estimate at $x/c = 4.5$ when the flow was attached at the trailing edge. The variation was approximately 15% when the airfoil was stalled. For drag estimates based on van Dam's method or the complete control volume formulation, the streamwise variation decreased as the streamwise position of measurements increased. For the circular cylinder the maximum variation observed was approximately 30% of the pressure based drag coefficient. The streamwise variation observed in the airfoil estimates was up to 50% and 20% of the drag estimate at $x/c = 4.5$ for the cases of attached flow and separated flow at the trailing edge respectively.

It is recommended to employ Jones' method in preference to either van Dam's or the complete control volume formulation since it appears to be the most consistent method. In addition, it is necessary to measure only two flow properties, total and static pressure. To employ Jones' method, wake profiles should be measured at least 10 times the projected model height downstream of the model. For the circular cylinder, this is equivalent to 10 diameters and, for the airfoil investigated, it is approximately 1 chord length from the trailing edge. The freestream reference conditions should be measured in the outer flow at the x location of the wake profile measurement.

Of the two methods based on wake velocity measurements, van Dam's and the complete control volume formulation, van Dam's method is recommended since it requires fewer experimental measurements than the complete control volume formulation, and results in approximately identical drag estimates. To employ van Dam's method wake profiles should be measured at a distance of 30 times the projected model height, or farther, downstream. For the cylinder, this is equivalent to measuring at $X/d \geq 30$ and for the airfoil at $x/c \geq 3$. The reference velocity must be measured in the outer flow at the streamwise location of the wake profile measurement. It is important to note that drag estimates are sensitive to the value of the reference velocity employed. It is recommended to measure the static

pressure variation in the wake directly, instead of approximating it from vertical velocity fluctuations, to improve the accuracy of the drag estimate.

The complete control volume formulation is recommended in applications where there is a significant difference between the outer flow properties above and below the wake velocity deficit region, such as might exist with a non-uniform freestream, or an asymmetric model. The levels of flow asymmetry observed in the current study were not large enough to necessitate the use of the complete control volume formulation. To employ the complete control volume formulation, wake profiles should be made at the same streamwise locations as for van Dam's method; at least 30 times the projected model height downstream. It is also recommended to measure the static pressure variation in the wake directly. In addition to the wake profile measurements, it is necessary to measure the upstream flow conditions. If the upstream conditions are uniform, they can be based on a single measurement point, otherwise, they should be quantified in detail. Drag estimates based on the complete control volume formulation are sensitive to the value of upstream conditions, therefore, quantifying these flow characteristics is important for accurate estimation of drag.

Chapter 8

Recommendations

Based on the findings in this thesis the following recommendations for future work are made:

1. Quantify the effects of blockage on the wake development and drag calculations. This can be accomplished by employing the wall streamlining capabilities of the University of Waterloo's adaptive walled wind tunnel. Repeating the same experimental measurements with the test section walls set in the streamlined configuration would allow the wake development to be measured, and drag coefficients calculated without blockage effects.

2. Conduct force balance based drag measurements, for the same experimental conditions, on both the circular cylinder and NACA 0018 airfoil model. This would permit the variation in measured drag estimate due to measurement technique to be quantified.

3. Determine the necessary spatial refinement of the wake profiles to accurately estimate drag. In the current study two measurement spacings were employed. The first was a coarser spacing, used in the outer flow regions of the wake profiles, and the second, a refined spacing employed in the velocity deficit region. However, this required significantly more measurements to be taken for the stalled airfoil, which has a wider wake compared to the case of an airfoil operating under attached flow conditions. If

the measurement refinement could be linked to a parameter such as velocity gradient it might decrease the experimental time of flow field based drag measurements.

4. Employ an alternative method of decomposing the two components of velocity from cross-wire measurements. The method employed during this study under predicted the streamwise velocity in regions of high turbulence intensity, as such pressure variation in the wake could not be accurately predicted based on cross-wire measurements alone. If vertical velocity fluctuations could be more accurately predicted the error due to estimating pressure variation in the wake could be assessed separately from the measurement error.

5. Investigate the spanwise wake development to ascertain the level of uncertainty introduced by spanwise flow variations. Wake profiles measured simultaneously with a spanwise separation would not only reveal the extent of spanwise variations, but could also be used to determine the effect on the calculated drag coefficients.

REFERENCES

[1] T. J. Mueller, L. J. Pohlen, P. E. Conigliaro, and B. J. Jr. Jansen. The influence of free-stream disturbances on low-Reynolds number airfoil experiments. *Experiments in Fluids*, 14:3–14, 1983.

[2] P. B. S. Lissaman. Low-Reynolds-number airfoils. *Annual Review Fluid Mechanics*, 15:223–239, 1983.

[3] T. J. Mueller and J. D. DeLaurier. Aerodynamics of small vehicles. *Annual Review of Fluid Mechanics*, 35(1):89–111, January 2003.

[4] M. Gad-el Hak. Control of low-speed airfoil aerodynamics. *AIAA Journal*, 28(9):1537–1552, 1990.

[5] C. P. van Dam. Recent experience with different methods of drag prediction. *Progress in Aerospace Sciences*, 35:751–798, 1999.

[6] M. Méheut and D. Bailly. Drag-breakdown methods from wake measurements. *AIAA Journal*, 46(4):847–862, April 2008.

[7] J. B. Barlow, W. H. Rae, and A. Pope. *Low-Speed Wind Tunnel Testing*. John Wiley & Sons, New York, 1999.

[8] M. S. H. Boutilier. *Experimental Investigation of Transition Over a NACA 0018 Airfoil at a low Reynolds Number*. MASc Thesis, University of Waterloo, 2011.

[9] J. J. Guglielmo and M. S. Selig. Spanwise variations in the profile drag for airfoil at low Reynolds numbers. *Journal of Aircraft*, 33(4):699–707, 1996.

[10] B. M. Jones. The measurement of profile drag by the pitot-traverse method. Technical report, Air Ministry - Aeronautical Research Committe Reports and Memoranda No. 1688, 1936.

[11] E. C. Maskell. Progress towards a method for the measurement of the components of the drag of a wing of finite span. Technical report, Royal Aircraft Establishment Technical Report 72232, 1973.

[12] B. W. van Oudheusden, E. W. F. Casimiri, and F. Scarano. Aerodynamic load characterisation of a low speed aerofoil using particle image velocimetry. *The Aeronautical Journal*, 112(1130):197–205, 2008.

[13] K. Kusunose. *A Wake Integration Method for Airplane Drag Prediction*. Sasaki Printing & Publishing Co. Ltd., Sendai, Japan, 2005.

[14] S. Yarusevych, P. E. Sullivan, and J. G. Kawall. On vortex shedding from an airfoil in low-Reynolds-number flows. *Journal of Fluid Mechanics*, 632:245, July 2009.

[15] B. H. Carmichael. Low Reynolds number airfoil survey. Volume 1. Technical report, National Aeronautics and Space Administration Contractor Report 165803, 1981.

[16] S. Yarusevych and M. S. H. Boutilier. Vortex shedding characteristics of a NACA 0018 airfoil at low Reynolds numbers. *AIAA Journal*, 49(10):2221–2227, 2011.

[17] T. J. Mueller. The influence of laminar separation and transition on low Reynolds number airfoil hysteresis. *Journal of Aircraft*, 22(9):763–770, September 1985.

[18] M. S. H. Boutilier and S. Yarusevych. Effects of end plates and blockage on low-Reynolds-number flows over airfoils. *AIAA Journal*, 50(7):1547–1559, July 2012.

[19] L. E. Jones, R. D. Sandberg, and N. D. Sandham. Direct numerical simulations of forced and unforced separation bubbles on an airfoil at incidence. *Journal of Fluid Mechanics*, 602:175–207, April 2008.

[20] S. Burgmann and W. Schröder. Investigation of the vortex induced unsteadiness of a separation bubble via time-resolved and scanning PIV measurements. *Experiments in Fluids*, 45(4):675–691, August 2008.

[21] G. S. Schmidt and T. J. Mueller. Analysis of low Reynolds number separation bubbles using semiemperical methods. *AIAA Journal*, 27(8):993–1001, 1989.

[22] M. M. O'Meara and T. J. Mueller. Laminar separation bubble characteristics on an airfoil at low Reynolds numbers. *AIAA Journal*, 25(8):1987, 1987.

[23] R. J. Gerakopulos, M. S. H. Boutilier, and S. Yarusevych. Aerodynamic characterization of a NACA 0018 airfoil at low Reynolds numbers. In *40th AIAA Fluid Dynamics Conference and Exhibit*, number July, pages 1–13, Chicago, Illinois, 2010.

[24] A. Roshko. Perspectives on bluff body aerodynamics. *Journal of Wind Engineering and Industrial Aerodynamics*, 49:79–100, 1993.

[25] C. H. K. Williamson. Vortex dynamics in the cylinder wake. *Annual Review Fluid Mechanics*, 28:477–539, 1996.

[26] C. Norberg. Fluctuating lift on a circular cylinder: review and new measurements. *Journal of Fluid and Structures*, 17:57–96, 2003.

[27] M. M. Zdravkovich. *Flow Around a Circular Cylinder, Vol. 1: Fundamentals*, volume 1. Oxford University Press, 1997.

[28] M. M. Zdravkovich. *Flow Around a Circular Cylinder, Vol. 2: Applications*, volume 2. Oxford University Press, 2003.

[29] M. S. Bloor. The transition to turbulence in the wake of a circular cylinder. *Journal of Fluid Mechanics*, 19(1964):290–304, 1963.

[30] J. H. Gerrard. The mechanics of the formation region of vortices behind bluff bodies. *Journal of Fluid Mechanics*, 25:401–413, 1966.

[31] H. Schlichting. On the plane wake problem. *Ingenieur Archiv*, 1:533–571, 1930.

[32] T. Okamoto and M. Takeuchi. Effect of side walls of wind-tunnel on flow around two-dimensional circular cylinder and its wake. *Bulletin of the JSME*, 18(123):1011–1017, 1975.

[33] R. E. D. Bishop and A. Y. Hassan. The lift and drag forces on a circular cylinder in a flowing fluid. *Proceedings of the Royal Society A: Mathematical and Physical Sciences*, 277(1368):32–50, 1964.

[34] J. H. Gerrard. An experimental investigation of the oscillating lift and drag of a circular cylinder shedding turbulent vortices. *Journal of Fluid Mechanics*, 11(02):244–256, March 1961.

[35] E. Achenbach. Distribution of local pressure and skin friction around a circular cylinder in cross-flow up to Re = 5x10ˆ6. *Journal of Fluid Mechanics*, 34(04):625, March 1968.

[36] C. Tropea, A. L. Yarin, and J. F. Foss, editors. *Springer Handbook of Experimental Fluid Mechanics*. Springer-Verlag Berlin Heidelberg, 2007.

[37] K. B. M. Q. Zaman and D. E. Culley. Flow separation control over an airfoil: implication of wake velocity-deficit reduction. In *4th Flow Control Conference*, number June, pages 1–20, Seattle, Washington, 2008.

[38] R. J. Goldstein, editor. *Fluid Mechanics Measurements*. Taylor & Francis, Washington, 2nd ed. edition, 1996.

[39] F. M. White. *Fluid Mechanics*. McGraw-Hill, New York, 7th edition, 2011.

[40] G. I. Taylor. The determination of drag by the pitot traverse method. Technical report, Reports and Memoranda of the Aeronautical Research Committee no. 1808, 1937.

[41] G. W. Brune. Quantitative low-speed wake surverys. *Journal of Aircraft*, Vol. 31(No. 2), 1994.

[42] T. T. Takahashi. On the decomposition of drag components from wake flow measurements. In *35th AIAA Aerospace Sceinces Meeting & Exhibit*, pages 1–10, Reno, NV, 1997.

[43] D. G. Bohl and M. M. Koochesfahani. MTV measurements of the vortical field in the wake of an airfoil oscillating at high reduced frequency. *Journal of Fluid Mechanics*, 620:63, January 2009.

[44] B. W. van Oudheusden, F. Scarano, E. W. M. Roosenboom, E. W. F. Casimiri, and L. J. Souverein. Evaluation of integral forces and pressure fields from planar velocimetry data for incompressible and compressible flows. *Experiments in Fluids*, 43(2-3):153–162, February 2007.

[45] A. Betz. A method for the direct determination of wing-section drag. Technical report, National Advisory Committee for Aeronautics Techinal Memorandum No. 337, 1925.

[46] A. Fage and L. J. Jones. On the drag of an aerofoil for two-dimensional flow. *Proceedings of the Royal Society A: Mathematical, Physical and Engineering Sciences*, 111(759):592–603, 1926.

[47] H. C. Neatby and S. Yarusevych. Towards reliable experimental drag measurements on an airfoil at low Reynolds numbers. In *42nd AIAA Fluid Dynamics Conference and Exhibit*, number June, pages 1–17, New Orleans, Louisiana, 2012.

[48] R. A. Antonia and S. Rajagopalan. Determination of drag of a circular cylinder. *AIAA Journal*, 28(10):1833–1384, 1990.

[49] M. J. Bishop. *Experimental Investigation of the Effect of Wall Adaptation on Flow Over a Cylinder in a Modernized Adaptive-Wall Wind Tunnel*. MASc Thesis, University of Waterloo, 2010.

[50] D. Sumner. *An Experimental Investigation of 3-D models in a 2-D Adaptive Wall Test Section*. MASc Thesis, Universtiy of Waterloo, 1994.

[51] R. J. Gerakopulos. *Investigating Flow over an Airfoil at low Reynolds Numbers Using Novel Time-Resolved Surface Pressure Measurements.* MASc Thesis, University of Waterloo, 2011.

[52] T. A. Fox and G. S. West. On the use of end plates with circular cylinders. *Experiments in Fluids*, 9:237 – 239, 1990.

[53] P. K. Stansby. The effects of end plates on the base pressure coefficient of a circular cylinder. *Aeronautical Journal*, 78:36–37, 1974.

[54] H. H. Bruun, M. A. Khan, H. H. Al-Kayiem, and A. A. Fardad. Velocity calibration relationships for hot-wire anemometry. *Journal of Physics E: Scientific Instruments*, 21(2):225–232, 1988.

[55] R. J. Gerakopulos. Wind tunnel traversing mechanism integration and flow quality assessment. Technical report, University of Waterloo, 2008.

[56] J. G. Kawall, M. Shokr, and J. F. Keffer. A digital technique for the simultaneous measurement of streamwise and lateral velocities in turbulent flows. *Journal of Fluid Mechanics*, 133:83–112, April 1983.

[57] D. W. Bryer and R. C. Pankhurst. *Pressure-Probe Methods for Determining Wind Speed and Flow Direction.* Her Majesty's Stationery Office, London, 1971.

[58] T. J. Dudzinski and L. N. Krause. Flow-direction measurement with fixed-position probes. Technical report, NASA, 1969.

[59] W. E. Lewis. Fixed-direction probes for aerodynamic measurements. *Proceedings of the Institution of Mechanical Engineers, Conference Proceedings*, 180, 1965.

[60] K. M. Argüelles Díaz, J. M. Fernández Oro, and E. Blanco Marigorta. Direct calibration framework of triple-hole pressure probes for incompressible flow. *Measurement Science and Technology*, 19(7):075401, July 2008.

[61] C. Norberg. Effects of Reynolds number and a low-intensity freestream turbulence on the flow around a circular cylinder. Technical Report 87, Chalmers University of Technology Department of Applied Thermodynamics and Fluid Mechanics, 1987.

[62] C. Norberg. Pressure forces on a circular cylinder in cross flow. In H. Eckelmann and International Union of Theoretical and Applied Mechanics, editors, *IUTAM Symposium Bluff-Body Wakes, Dynamics, and Instabilites*, pages 275–278, Gottingen, Germany, 1992. Springer-Verlag.

[63] A. Thom. An investigation of fluid flow in two dimensions. Technical report, Aeronautical Research Committee, 1928.

[64] B. Cantwell and D. Coles. An experimental study of entrainment and transport in the turbulent near wake of a circular cylinder. *Journal of Fluid Mechanics*, 136:321–374, April 1983.

[65] Oertel, H. Jr. Wakes behind blunt bodies. *Annual Review Fluid Mechanics*, 22:539–564, 1990.

[66] L. Ong and J. Wallace. The velocity field of the turbulent very near wake of a circular cylinder. *Experiments in Fluids*, 20(6):441–453, April 1996.

[67] V. C. Patel and G. Scheuerer. Calculation of two-dimensional near and far wakes. *AIAA Journal*, 20(7):900–907, 1982.

[68] M. Matsumura and R. A. Antonia. Momentum and heat transport in the turbulent intermediate wake of a circular cylinder. *Journal of Fluid Mechanics*, 250:651–668, April 1993.

[69] H. Schlichting and K. Gersten. *Boundary-Layer Theory*. Springer-Verlag, Berlin, 8th edition, 2003.

[70] B. R. Ramaprian, V. C. Patel, and M. S. Sastry. The symmetric turbulent wake of a flat plate. *AIAA Journal*, 20(9):1228–1235, 1982.

[71] A. A. Townsend. Measurements in the turbulent wake of a cylinder. *Proceedings of the Royal Society A: Mathematical, Physical and Engineering Sciences*, 190(1023):551–561, September 1947.

[72] I. Tani. Low speed flows involving bubble separations. *Progress in Aerospace Sciences*, 5:70–103, 1964.

[73] M. S. H. Boutilier and S. Yarusevych. Separated shear layer transition over an airfoil at a low Reynolds number. *Physics of Fluids*, 24(8):084105, 2012.

[74] A. Silverstein, S. Katzoff, and W. K. Bullivant. Downwash and wake behind plain and flapped Airfoils. Technical report, National Advisory Committee for Aeronautics No. 651, 1939.

[75] S. Yarusevych. *Investigation of Airfoil Boundary Layer and Turbulent Wake Development at Low Reynolds Numbers*. PhD Thesis, University of Toronto, 2006.

[76] H. L. Dryden and R. H. Heald. Investigation of turbulence in wind tunnels by a study of the flow about cylinders. Technical Report 231, NACA Report No. 231, 1926.

[77] H. Lim and S. Lee. Flow control of circular cylinders with longitudinal grooved surfaces. *AIAA Journal*, 40(10):2027–2036, 2002.

[78] H. Nakamura and T. Igarashi. Omnidirectional reductions in drag and fluctuating forces for a circular cylinder by attaching rings. *Journal of Wind Engineering and Industrial Aerodynamics*, 96(6-7):887–899, June 2008.

[79] M. K. Heerenbrink. *Simultaneous PIV and balance measurements on a pitching aerofoil*. MS Thesis, Delft University of Technology, 2011.

[80] R. E. Sheldahl and P. C. Klimas. Aerodynamic characteristics of seven symmetrical airfoil sections through 180-degree angle of attack for use in aerodynamic analysis of vertical axis wind turbines. Technical report, Sandia National Laboratories Energy Report SAND80-2114, 1981.

[81] R. J. Moffat. Describing the uncertainties in experimental results. *Experimental Thermal and Fluid Science*, 1:3–17, 1988.

[82] H. H. Bruun. *Hot-Wire Anemometry: Principles and Signal Analysis*. Oxford University Press, 1995.

APPENDICES

Appendix A

Experimental Uncertainty

The experimental uncertainty in the measured properties presented in this thesis are listed in Table A.1. All affected figures and tables, and any associated limitations, have also been included in Table A.1. All experimental uncertainty values reported were calculated based on the approach recommend in Ref. [81]. The estimated uncertainty is stated as a 95% confidence interval on the listed value. For each source of error the uncertainties are estimated and then combined, assuming they are mutually exclusive, to arrive at the overall uncertainty. A general equation for the total estimated uncertainty is shown below, as specified in Ref. [81].

$$\delta R = \left\{ \sum_{i=1}^{N} \left(\frac{\delta R}{\delta X_i} \delta X_i \right)^2 \right\}^{1/2} \tag{A.1}$$

Note, the estimated uncertainty in drag coefficients are not included in Table A.1, since they are affected by multiple parameters. Instead the uncertainty in drag coefficients have been included in the applicable figures and tables with the text. The method used to calculate uncertainty in the estimated drag coefficients has been described in detail below.

A.1 Uncertainty in Experimental Conditions

Experimental conditions, such as test section velocity, model orientation, and flow properties, are specified for each experimental test. When conducting a test, the experimental conditions in the wind tunnel were set to match the specified conditions and monitored through out the duration of the experiment, to prevent deviations from occurring. However,

Table A.1: Summary of experimental uncertainty in measured values.

Parameter	Applicability	Uncertainty	Related Tables and Figures
$c_{p,w}$	$Re_c = 100,000$	± 0.016	Fig. 4.17
	$Re_d = 8,000$	± 0.030	Fig. 4.1
	$Re_d = 20,000$	± 0.005	Fig. D.1
$c_{p,surf}$	$Re_c = 100,000$	± 0.016	Fig. 4.19
	$Re_d = 8,000$	± 0.026	Fig. 4.3
	$Re_d = 20,000$	± 0.005	Fig. D.3
Re_c		± 2600	
Re_d	$Re_d = 8,000$	± 330	
	$Re_d = 20,000$	± 360	
u'	based on u'/U	1-5%	Figs. 4.5, 4.11b, 4.21, 4.25, D.5, D.11b, D.17, & D.19
U	based on u'/U	2-12%	Figs. 4.4, 4.11a, 4.20, 4.24, D.4, D.11a, D.17, & D.18
v'	based on u'/U	1-15%	Figs. 4.7, 4.11c, 4.22, 4.26, D.7, D.11d, D.17, &D.21
V	based on u'/U	2-20%	Figs. 4.6, 4.11d, 4.23, 4.27, D.6, D.11c, D.17, & D.20
x/c		± 0.005	Figs. 4.28, 4.29, 4.30, 4.37, & 4.38
X/d		± 0.05	Figs. 4.8, 4.9, 4.10, 4.15, 4.16, 5.1, 5.2, 5.4, 5.7, 5.8, 5.12, D.8, D.9, D.10, D.15, & D.16
y/c		± 0.0025	Figs. 4.20, 4.21, 4.22, 4.23, 4.24, 4.25, 4.26, 4.27, 4.31, 4.32, 4.35, 4.33, 4.34, 4.36, D.17, D.18, D.19, D.20, D.21, D.22, D.23, D.24, & D.25
Y/d		± 0.025	Figs. 4.4, 4.5, 4.6, 4.7, D.4, D.5, D.6, D.7, D.12, D.13, & D.14
α		$\pm 0.22^\circ$	
θ		$\pm 0.51^\circ$	Figs. 4.3 & D.3

there is uncertainty inherent in all experimental test parameters. This section contains the uncertainty estimates for all measurements relating to experimental conditions.

Airfoil angle of attack was set with a digital protractor, mounted on the model axis, with

an angular resolution of 0.1°. A bias error will be introduced into the angle of attack from uncertainty in the zero angle. Aerodynamic zero was determined though a series of model surface pressure measurements at different set angles. Upper and lower surface pressure distributions were measured and compared, aerodynamic zero was identified as the angle at which the same positive and negative angle provided the best symmetry [51]. Model imperfections, even relatively minor ones, can make determining the zero angle difficult since the flow development is sensitive to experimental conditions [17]. The uncertainty in the zero angle has been estimated to be less than 0.2° for the NACA 0018 airfoil [8]. The overall uncertainty in angle of attack is estimated to be less than 0.22°.

Surface pressure profiles, on the circular cylinder, were measured by rotating a single pressure tap through a 180° arc. Tap angle from the stagnation point, θ, was measured via a digital protractor with an angular resolution 0.1°. The stagnation point, $\theta = 0°$, was identified by measuring pressure distributions passing through the stagnation point and then identifying the angle of maximum surface pressure from the measured distributions. Due to tap size and uncertainty in pressure measurements, the uncertainty in the zero angle was estimated to be less than 0.5°. The overall uncertainty in θ is estimated to be less than 0.51°.

Reynolds number is based on the test section velocity, characteristic length of the model, and fluid properties. Test section velocity is set via the contraction pressure drop, which has been calibrated against a pitot-static tube reading of the freestream velocity, in the empty test section. The contraction pressure drop is measured with an inclined manometer. For the airfoil tests and the cylinder tests at $Re_d = 8,000$, the minor division of the manometer was 0.25 Pa. For the cylinder tests at $Re_d = 20,000$, the minor division of the manometer used was 0.50 Pa. The estimated uncertainty in contraction pressure drop is less than 0.50 Pa for the airfoil and lower speed cylinder tests, and less than 1.0 Pa for the higher speed cylinder tests. The uncertainty in pitot-static measurements during calibration of the contraction pressure drop is estimated to be less than 0.50 Pa [8]. The allowed variation in freestream speed, over the duration of an experiment, was less than 1% of the set speed. The overall uncertainty in freestream speed is less than 2.8% for the airfoil tests, under 4% for the cylinder tests at $Re_d = 8,000$, and less than 1.6% for the cylinder operating at $Re_d = 20,000$. The ambient temperature was permitted to vary within ±1°C of the hot-wire calibration temperature, therefore changes in fluid properties are limited by the allowed temperature change. The resulting estimated uncertainty in Reynolds number for the three test conditions are listed in Table A.1.

A.2 Cross-Wire Uncertainty

Uncertainty in constant temperature anemometry measurements has been the focus of many studies [36, 54, 56, 82]. Measurement error is related to probe geometry, calibration technique, flow direction, turbulence intensity, probe orientation, and velocity gradients [82]. All hot-wire measurements in this study were taken with a cross-wire oriented to capture streamwise and vertical velocity components. For the purposes of estimating experimental uncertainty it will be assumed that the mean wake flow is entirely two-dimensional, i.e. there is no mean spanwise component of flow. Estimates of the uncertainty in cross-wire measurements were based on the extensive study of hot-wire error by Kawall et al. [56]. Three factors were accounted for when estimating the measurement uncertainty based on the findings in Ref. [56], specifically probe geometry, voltage response, and local turbulence intensity. The ranges in estimated measurement uncertainty, for the four measured flow parameters, are listed in Table A.1, along with the ranges of turbulence intensity for which they are applicable. In general, as the turbulence intensity increases so does cross-wire measurement uncertainty.

A.3 Pressure Measurement Uncertainty

Several different pressure measurements were conducted during this investigation. They include wall static pressure measurements, model surface pressure measurements, pitot-static tube measurements, and three-hole probe measurements. The experimental uncertainty is related to the pressure transducer, freestream velocity, and specific measurement. A summary of the uncertainties in pressure measurements for specific flow conditions is listed in Table A.1.

An excellent discussion of the experimental uncertainty in the wall and model surface pressure measurements can be found in Ref. [8] for the same experimental set-up. The overall uncertainty in wall pressure coefficients and model surface pressure coefficients is estimated to be less than 1.6% of the freestream dynamic pressure for the airfoil tests conducted at a chord Reynolds number of $100,000$. Since the experiments conducted on the circular cylinder were performed at different freestream speeds the relative magnitude of these uncertainties differ. The specific uncertainty estimates, in wall and model surface pressure coefficients, for the circular cylinder tests can be found in Table A.1.

A.4 Drag Coefficient Uncertainty

Experimental uncertainty in the drag coefficients, due to measurement uncertainty, was estimated based on the method suggested for formulas involving numerical integration in Ref. [81]. This method was incorporated in the drag coefficient calculations to minimise the possibility of introducing calculation error. To calculate the uncertainty, each experimental variable involved in the drag calculation was individually perturbed, by the estimated measurement uncertainty, and the drag coefficient recalculated for each perturbation. The overall uncertainty was then calculated from the root squared sum (RSS) of all the changes of drag estimate. Each variable was perturbed twice, to find the resulting positive and negative changes in drag coefficient. The potential upper and lower bounds of the drag coefficient were calculated separately because some of the drag equations contain non-linear terms. The resulting uncertainty estimates are reported with the results of the drag coefficient calculations. The uncertainty in the measurements, each estimate is based on, are listed in Table A.1.

Appendix B

ASW Wall Coordinates

For all tests presented in this study, tests were conducted in a neutrally buoyant test section of the University of Waterloo's adaptive walled wind tunnel. This was achieved by setting the moveable top and bottom walls of the test section in the aerodynamically straight walled (ASW) configuration. The ASW configuration accommodates for boundary layer growth on the four test section walls and results in a constant centreline velocity. Boundary layer growth was predicted using the 1/7th power law for turbulent boundary layers, as described in Ref. [50] and is affected by the freestream velocity of the test. The wall positions for the ASW configuration are shown in Fig. B.1, as vertical displacement from the geometrically straight walled (GSW) configuration, for the three freestream speeds employed during this study. The roof position is indicated by the hollow symbols and the floor position by the solid symbols. Figure B.1a depicts the wall positions for the circular cylinder tests at $Re_d = 8,000$ and $Re_d = 20,000$, and Fig. B.1b the wall positions for the airfoil tests conducted at $Re_c = 100,000$. In all three cases the upper and lower walls diverge as the streamwise position increases, compensating for the growing boundary layer.

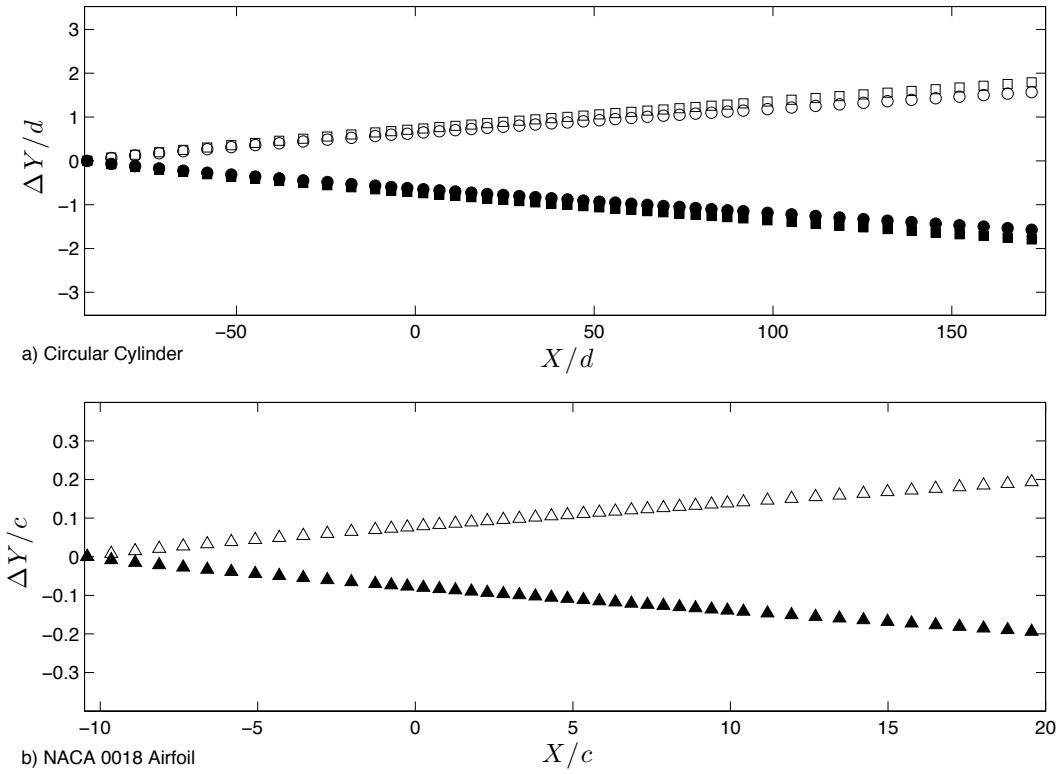

Figure B.1: Upper and lower test section wall positions, from the geometrically straight configuration, in ASW configuration. Hollow symbols indicate the roof displacement and solid symbols the floor displacement.

Appendix C

Probe Calibration Curves

C.1 Three-Hole Probe

C.1.1 Calibration Curves

The three-hole probe was calibrated in the empty test section against a pitot-static tube positioned 20 mm away in the spanwise direction. To construct a set of calibration curves, the three three-hole pressures, p_A, p_B, and p_C, were measured while the probe was rotated from approximately $+22°$ to $-22°$, from the freestream velocity, by two degree increments. Simultaneously pitot-static pressures were measured in the flow. Using the five pressure measurements and calibration equations, Eqs. C.1 - C.3, a complete set of calibration curves could then be constructed.

$$C_\alpha = \frac{p_B - p_C}{p_A - 0.5\,(p_B + p_C)} \tag{C.1}$$

$$C_{p_0} = \frac{p_0 - p_A}{p_A - 0.5\,(p_B + p_C)} \tag{C.2}$$

$$C_{p_s} = \frac{p_0 - p_s}{p_A - 0.5\,(p_B + p_C)} \tag{C.3}$$

A set of typical calibration curves for the three-hole probe are shown in Fig. C.1. Curves were constructed from the calibrated data points through linear interpolation as recommended by Ref. [60].

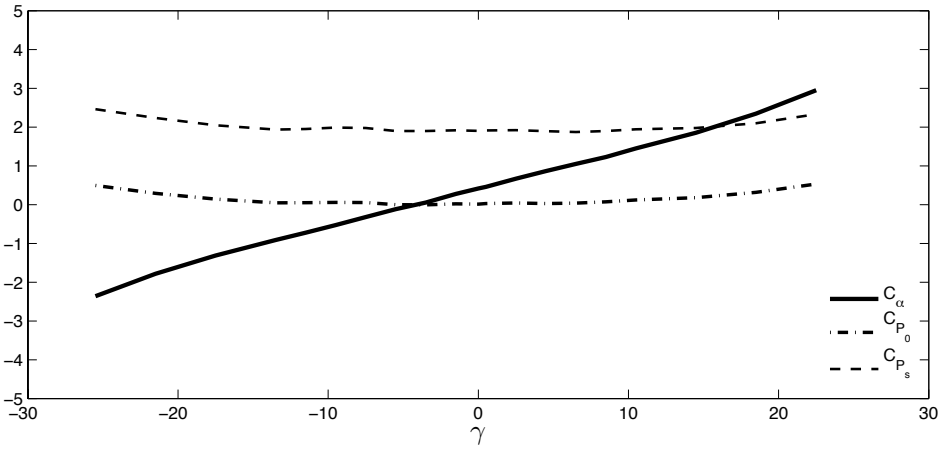

Figure C.1: Typical calibration curves for the three hole probe.

C.1.2 Pressure Gradient

Pressures measured via the three-hole probe differ from the same measurements made with the pitot-static tube for $X/d \leq 20$. The difference between the two measurement techniques is greatest in the region of maximum pressure deficit, around the wake centreline. While there are differences in the measured value for both the total and static pressure profiles, it is most significant in the static pressure profiles.

The discrepancies are due to the presence of a steep vertical pressure gradient in the wake. Neither the pitot-static tube, nor the three-hole probe, are designed to be used in flows containing a vertical pressure gradient, however, due to the physical geometry and calibration method employed, three-hole probe measurements are more sensitive to pressure gradients. The pitot-static tube consists of two concentric tubes. The central tube forms the tip of the probe and is used to measure the total pressure. The outer tube is fused to the central tube at the tip, creating a smooth surface, and has static pressure taps drilled around the circumference of the tube, several millimetres downstream from the tip. The static pressure is then measured from the far end of the outer tube. Since static pressure taps are drilled around the entire circumference, the measured pressure is, as a consequence, an average of the static pressures surrounding the tube. Therefore, in the presence of a pressure gradient, while the individual static pressure taps are exposed to different pressures, the cumulative static pressure is an average of the static pressure at all the taps. Whereas, the three-hole probe consists of three individual tubes arranged vertically. From the three tubes, three independent pressures, p_A, p_B, and p_C, are mea-

sured. Then using the calibration curves, see Fig. C.1, and Eq. C.1, the total and static pressure is calculated. In the presence of a steep, vertical pressure gradient, the total and static pressure of the fluid at the tip of each tube will differ, even if only slightly. This will cause the probe response to deviate from the calibrated probe operation. Since the total and static pressure are calculated from using the probe response seen during calibration, an error is then introduced in the reported values.

To confirm the vertical pressure gradient is the cause of the observed measurement error, an artificial pressure gradient was introduced into the calibration data, and the resulting change in total and static pressure quantified. The slope of the artificial gradient was based on the total and static pressure gradients which exist in the wake profiles for $X/c \leq 20$. For the total pressure the slope of the gradient ranges between 400 Pa/m and 100 Pa/m, and for the static pressure it is between 140 Pa/m and 20 Pa/m. Since the pressure measured by the individual tubes in the three-hole probe is a combination of total and static pressure a range of pressure gradients was tested to determine the impact on the results. The resulting deviation from calibrated values, for the total and static pressure, due to select pressure gradients are listed in Table. C.1. For each slope a range of errors is reported, this captures the effect of a positive, negative, and non-constant gradient on the calculated pressure. The impact on the calculated static pressure is much greater than on the total pressure for all conditions investigated, this is due to both the magnitude of the pressure term and the sensitivity of the static pressure calculations to the pressure gradient.

Table C.1: Percent error in total and static pressure from calibrated values when the three-hole probe is employed in the presence of a vertical pressure gradient of varying slopes.

[ht]

Value	Pressure Gradient [Pa/m]		
	370	200	100
p_0	$< 4\%$	$< 0.5\%$	0%
p_s	$5 - 40\%$	$2 - 25\%$	$1 - 15\%$

Several other findings came to light whilst investigating the effect of the pressure gradient on pressure calculations. The total pressure is most sensitive to a constant vertical gradient, while the static pressure is most sensitive to a non-uniform gradient. These findings agree with the experimental data, where the greatest difference between the pitot-static tube and the three-hole probe occurs around the centreline, a region of rapidly changing pressure gradients. The only location where the pressure gradient was steep enough to

affect the total pressure reading significantly occurred at $X/d = 3$. This is the location where the greatest disparity in measurements occurs.

The differences between the pressure profiles measured with the pitot-static tube and the three-hole probe are a consequence of the vertical pressure gradient which exist in the wake. The three-hole probe static pressure measurements are most sensitive to regions of changing pressure gradient, such as occur near the wake centerline. It leads to noticeable differences between measurement techniques up to $X/d = 20$ downstream from the cylinder. For this reason, wake profile measured with the three-hole probe will not be used for drag calculations.

C.2 Cross-Wire Probe

C.2.1 Calibration Curves

Calibration of the cross-wire probe was performed with the probe in situ. The cross-wire probe was positioned, via the three axis traversing mechanism, upstream of the model in an area of undisturbed flow. The cross-wire was calibrated against a pitot-static tube positioned 10 mm below the cross-wire, at the same streamwise location. A set of calibration curves, representative of typical calibration curves, for the two wires are depicted in Fig. C.2. Calibration data points were taken for the entire range of anticipated velocities for the specific test conditions. The curves shown in Fig. C.2 were measured in advance of performing tests with a freestream speed of approximately 7.5 m/s.

A fifth order polynomial fit, shown by the solid and dotted lines in Fig. C.2, was employed to fit the voltage response of the two wires, and used to interpolate between calibration points [54]. Probe calibration was found to remain accurate for a maximum of 72 hours if no significant change in ambient conditions occurred prior to that time.

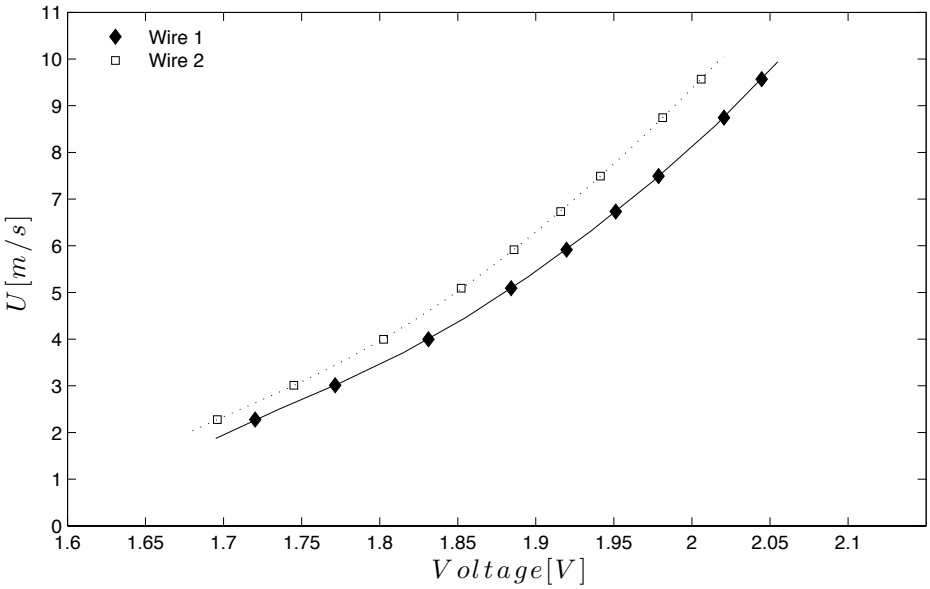

Figure C.2: Representative calibration curves for wires 1 and 2 of the cross-wire probe.

Appendix D

Additional Flow Development Plots

Contained within this appendix are the wake profiles for the circular cylinder operating at a Reynolds number of $20,000$ and the NACA 0018 airfoil operating at a chord Reynolds number of $100,000$ for two angles of attack, $0°$ and $5°$. The trends observed in the wake profiles included in this section match those discussed in the main body. In both cases, the plots illustrate classical turbulent wake development. This data, when combined with the summative plots found in the main body of the thesis, are designed to provide a complete picture of wake development for a circular cylinder operating at $Re_d = 20,000$ and a NACA 0018 airfoil operating at $\alpha = 5°$. The data for $\alpha = 0°$ has been included as an additional point of comparison.

D.1 Circular Cylinder Flow Development

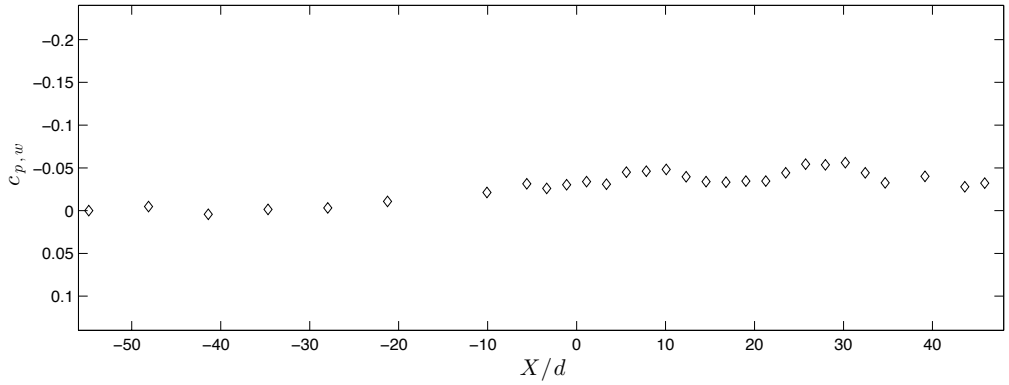

Figure D.1: Surface pressure distribution along the roof of the test section, set in the ASW configuration, with a circular cylinder operating at a Reynolds number of $20,000$.

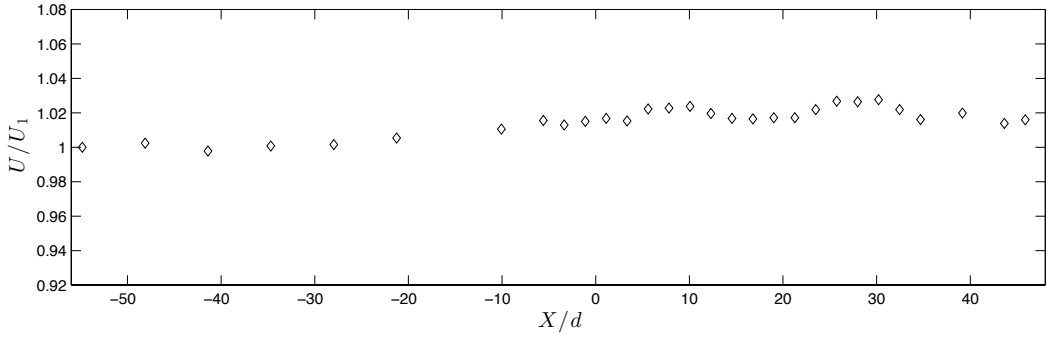

Figure D.2: Variation in the outer flow velocity along the test section for circular cylinder experiments.

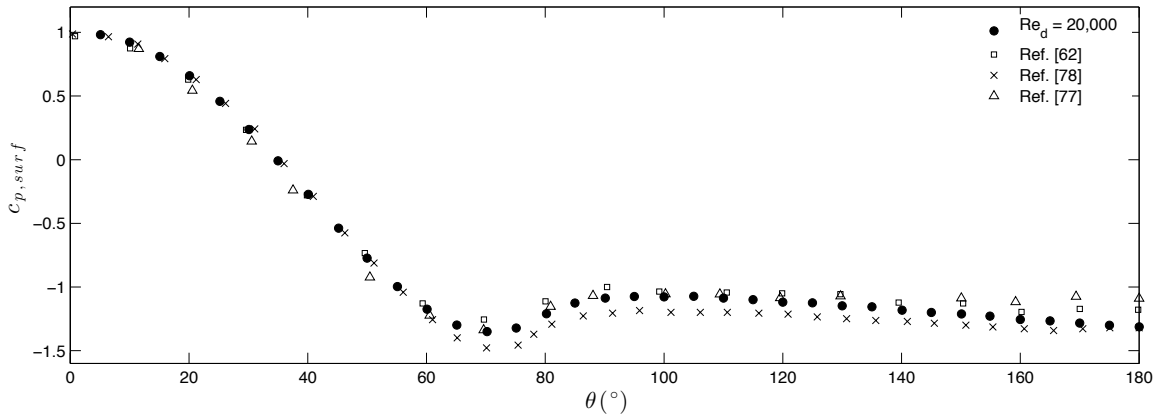

Figure D.3: Surface pressure distribution measured on the surface of the circular cylinder operating at a Reynolds number of $20,000$ shown with reference to profiles from the work of Norberg [62], Nakamura and Igarashi [78], and Lim and Lee [77].

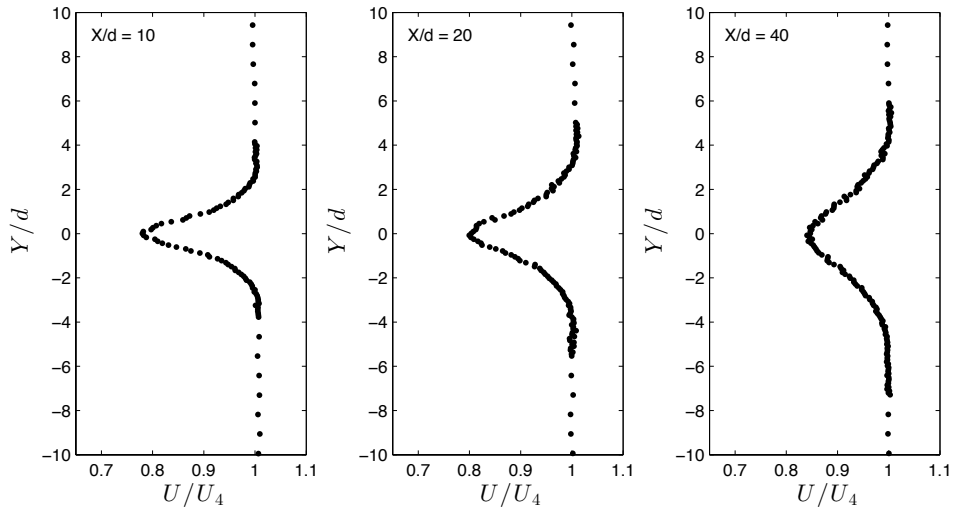

Figure D.4: Mean streamwise velocity wake profiles for the circular cylinder operating at a Reynolds number of $20,000$.

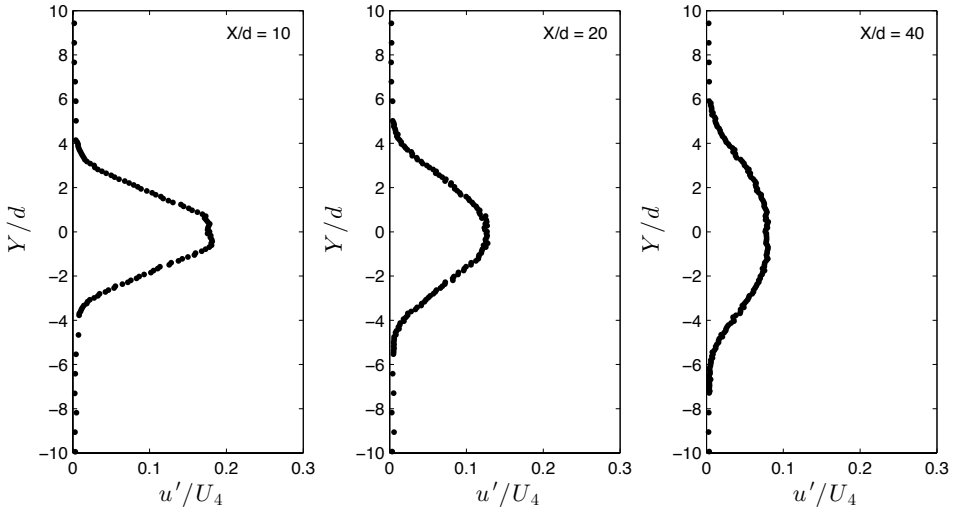

Figure D.5: Streamwise RMS velocity wake profiles for the circular cylinder operating at a Reynolds number of 20,000.

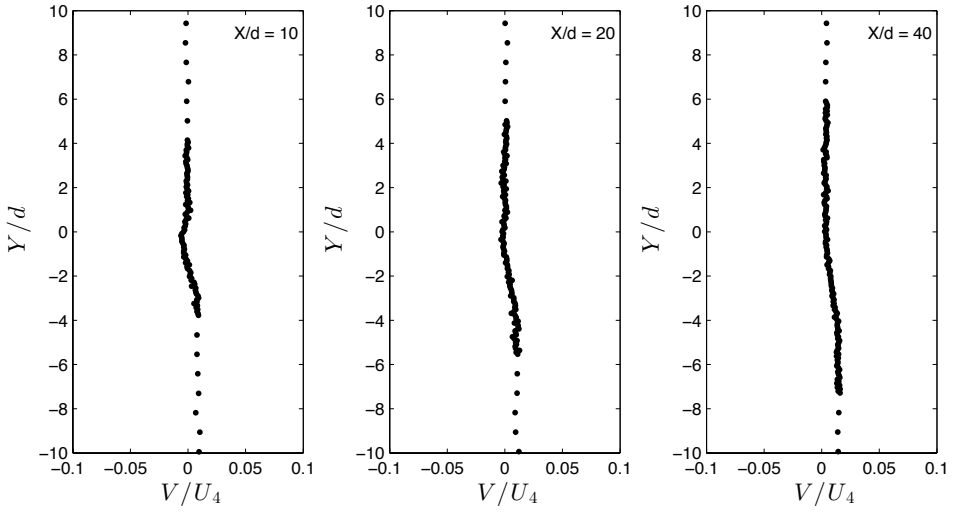

Figure D.6: Mean vertical velocity wake profiles for the circular cylinder operating at a Reynolds number of 20,000.

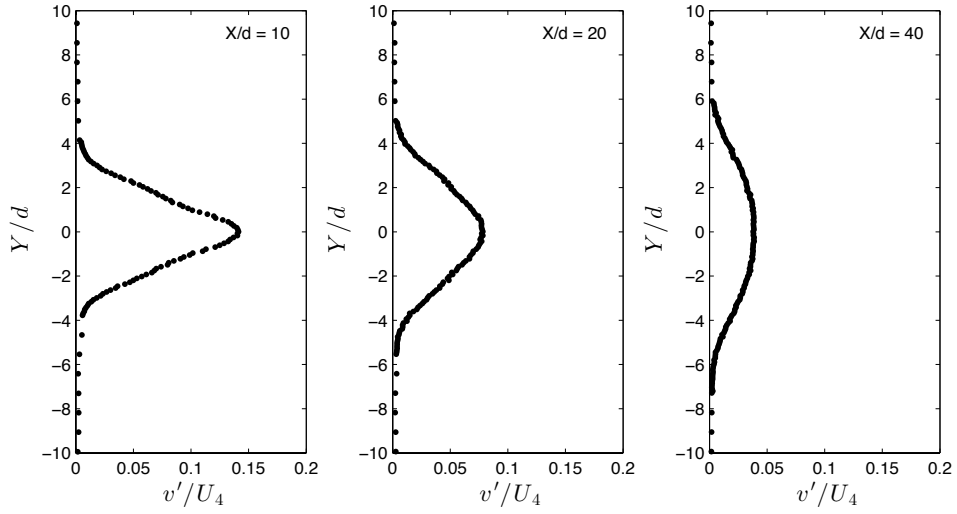

Figure D.7: Vertical RMS velocity wake profiles for the circular cylinder operating at a Reynolds number of $20,000$.

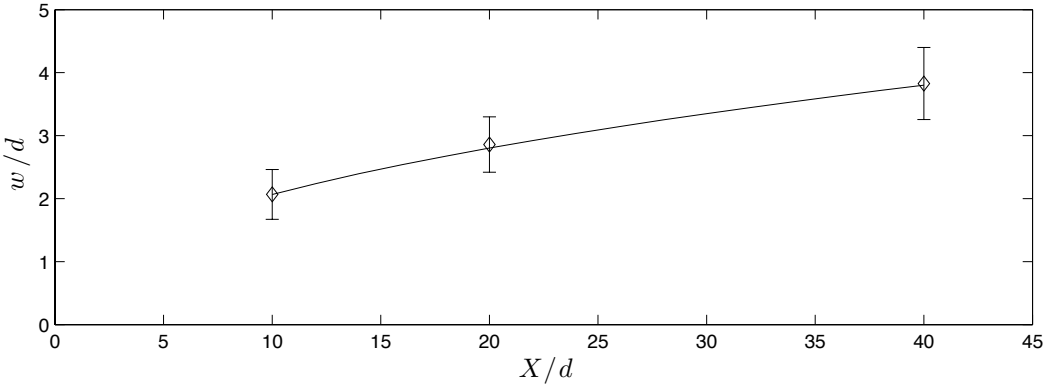

Figure D.8: Wake half width growth for the circular cylinder operating at a Reynolds number of $20,000$.

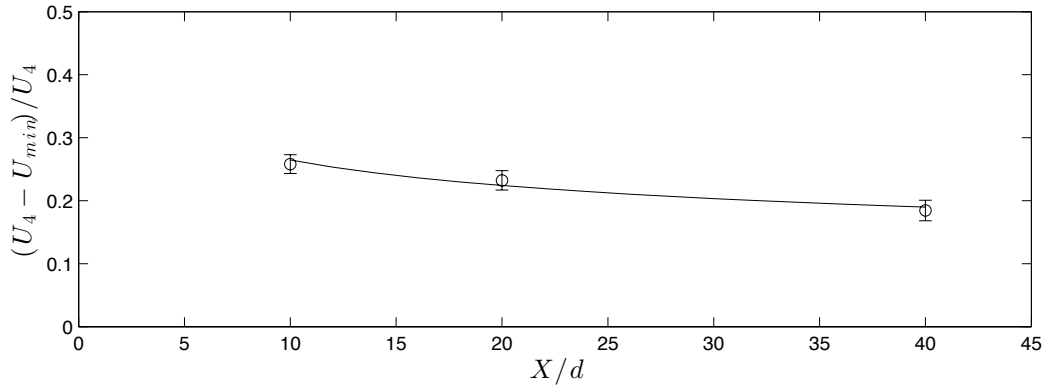

Figure D.9: Streamwise maximum velocity deficit for the circular cylinder operating at a Reynolds number of $20,000$.

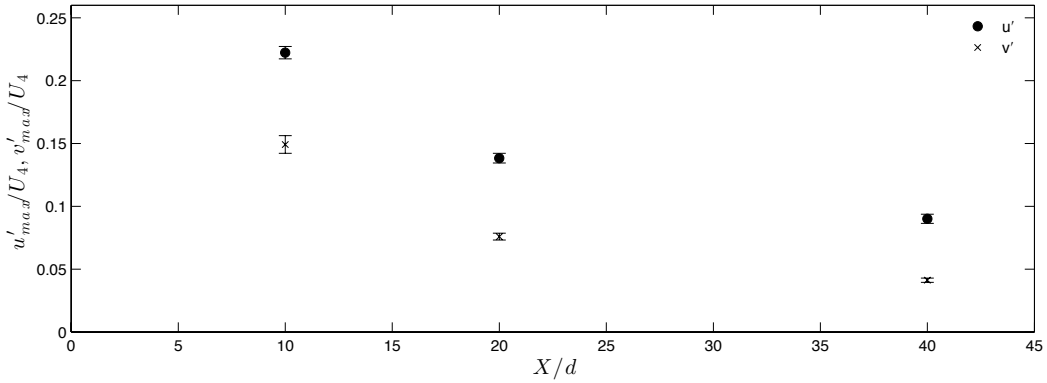

Figure D.10: Decay of maximum streamwise and vertical RMS velocity components in the wake of a circular cylinder operating at a Reynolds number of $20,000$.

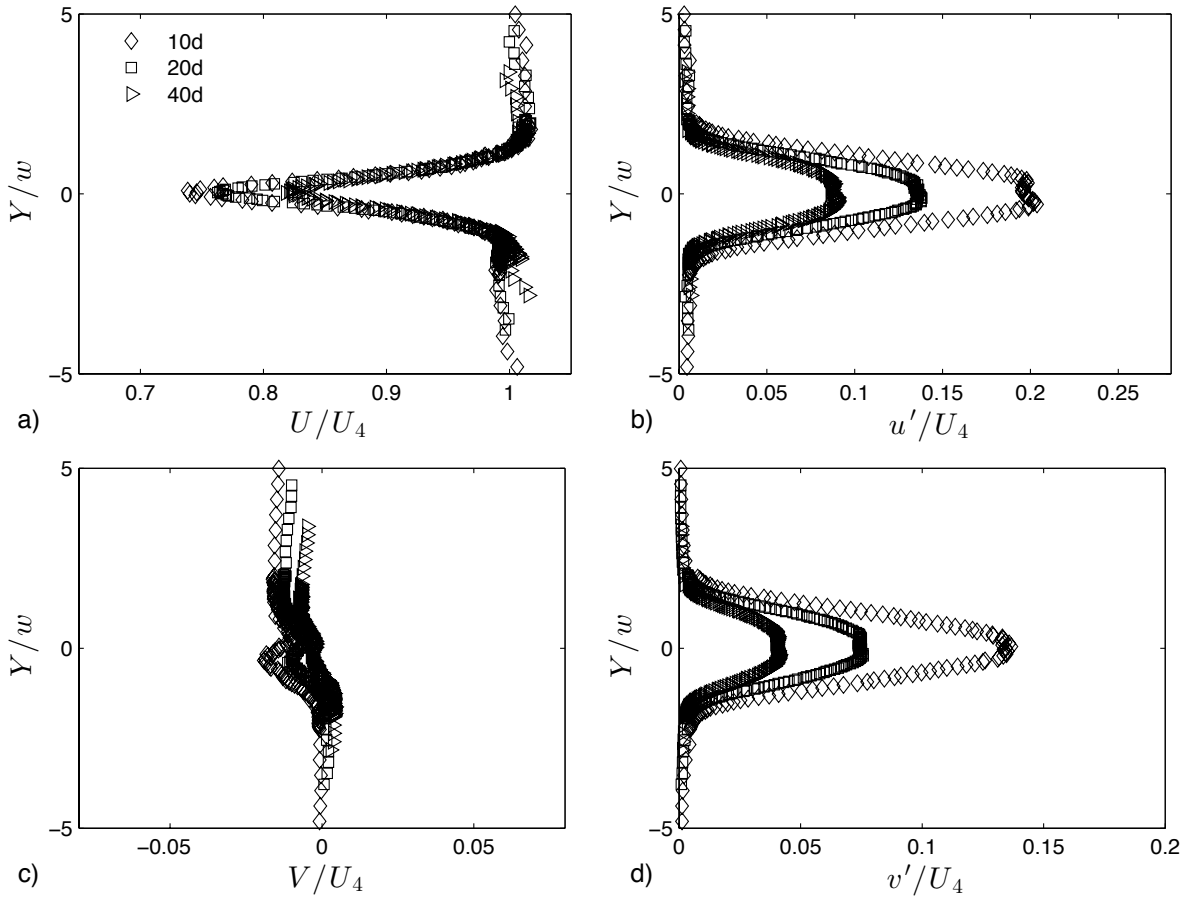

Figure D.11: Normalized velocity profiles scaled by wake half width for the circular cylinder operating at a Reynolds number of $20,000$.

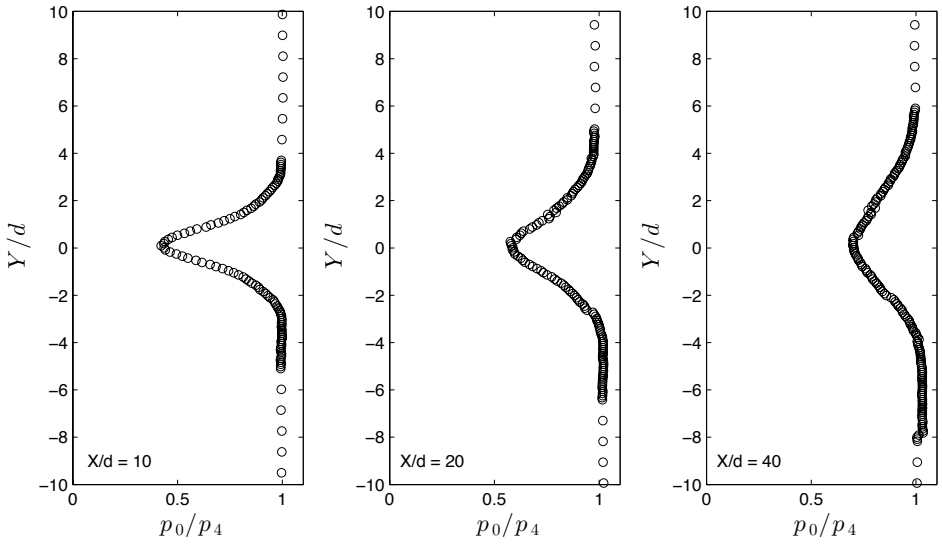

Figure D.12: Normalized total pressure profiles measured in the wake of the circular cylinder operating at a Reynolds number of $20,000$ with the pitot-static tube.

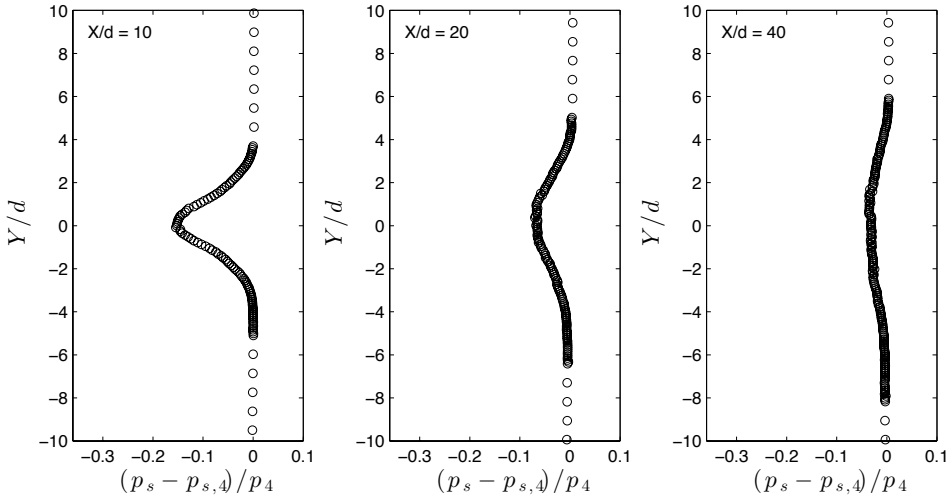

Figure D.13: Static pressure variation in the wake profile, measured via the pitot-static tube downstream of the cylinder operating at a Reynolds number of $20,000$.

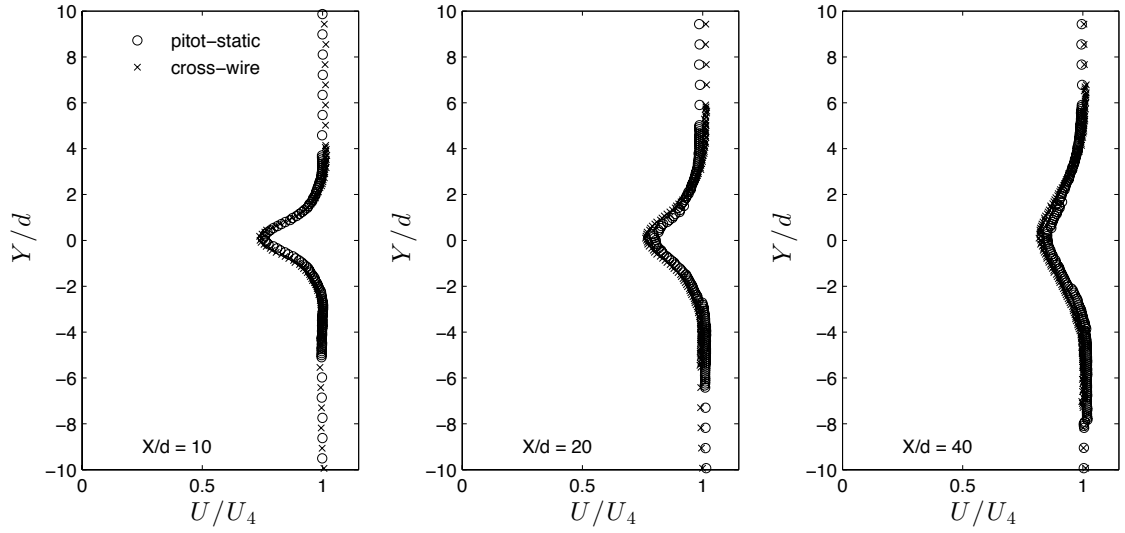

Figure D.14: Comparison of streamwise velocity profiles based on pitot-static tube and cross wire measurements for $Re_d = 20,000$.

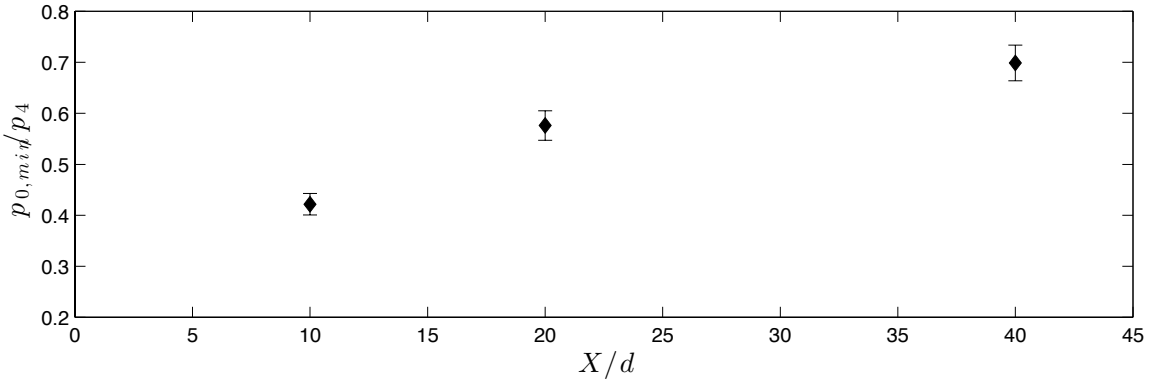

Figure D.15: Streamwise change of wake centreline total pressure for the circular cylinder operating at a Reynolds number of $20,000$.

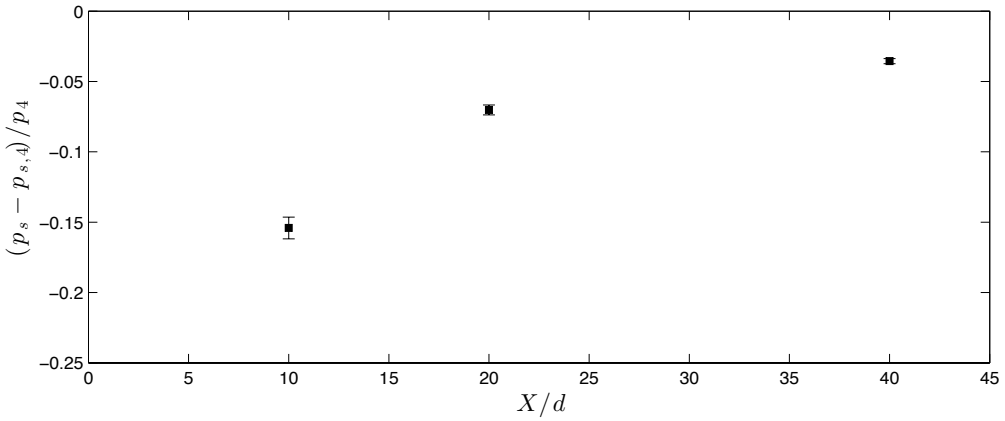

Figure D.16: Recovery of maximum static pressure deficit along the wake of the circular cylinder operating at $Re_d = 20,000$.

D.2 NACA 0018 Airfoil Flow Development

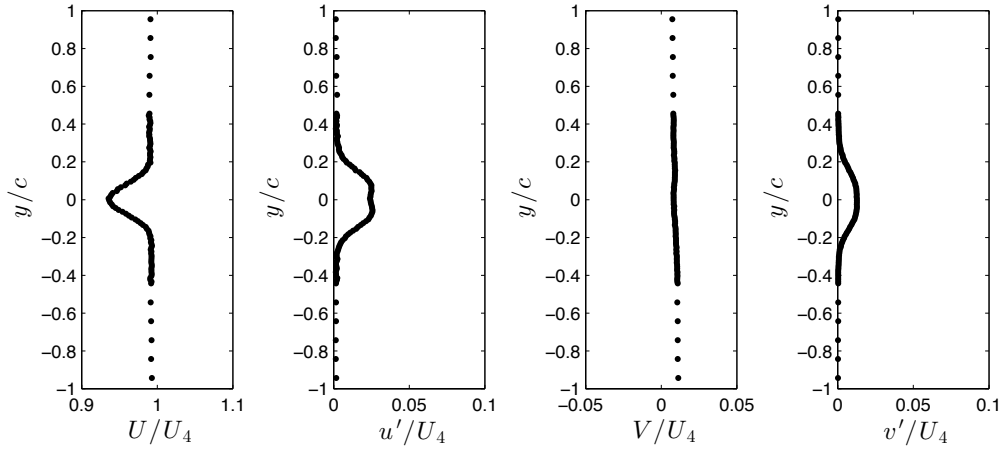

Figure D.17: Wake profiles measured $4.5c$ downstream from the airfoil operating at $Re_c = 100,000$ and $\alpha = 0°$.

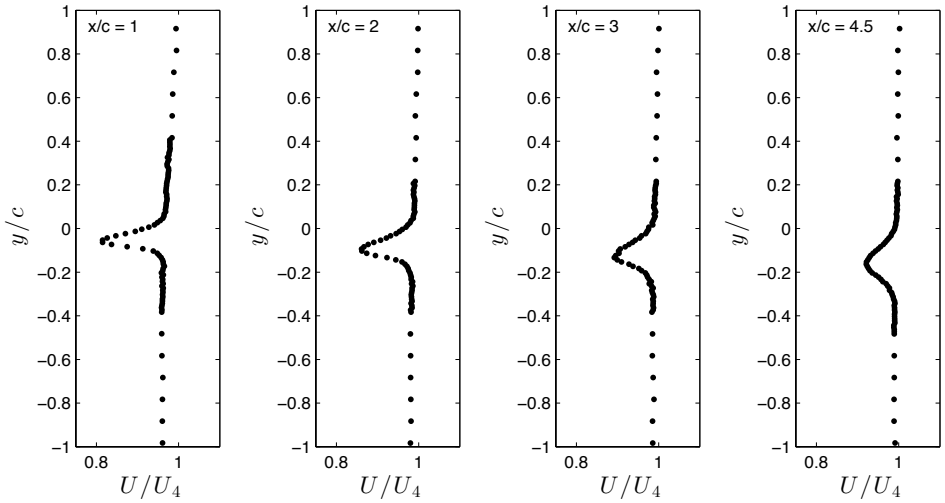

Figure D.18: Mean streamwise wake profiles measured with the airfoil operating at $Re_c = 100,000$ and $\alpha = 5°$.

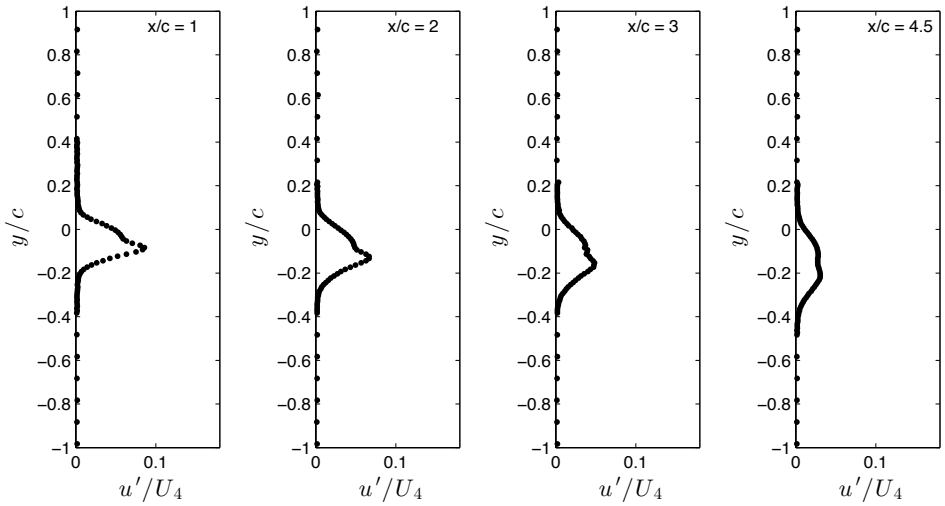

Figure D.19: RMS streamwise wake profiles measured with the airfoil operating at $Re_c = 100,000$ and $\alpha = 5°$.

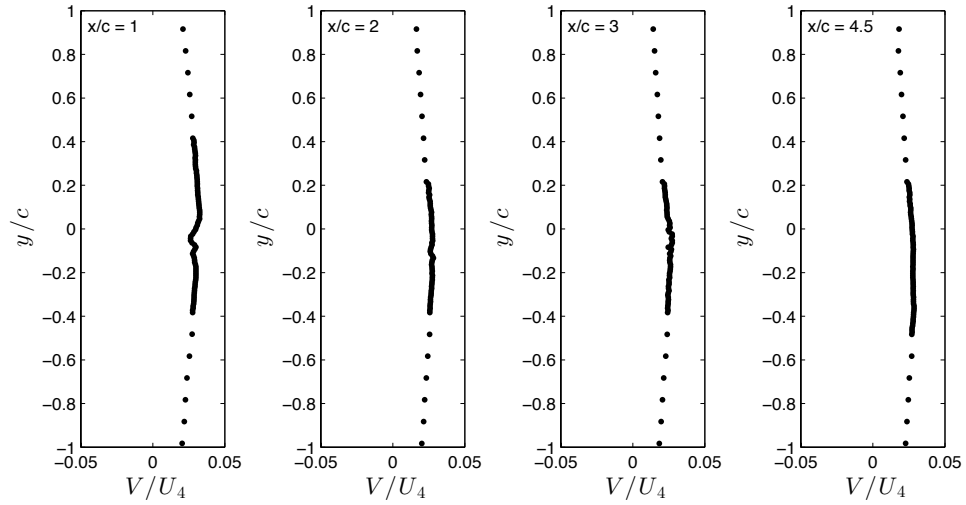

Figure D.20: Mean vertical wake profiles measured with the airfoil operating at $Re_c = 100,000$ and $\alpha = 5°$.

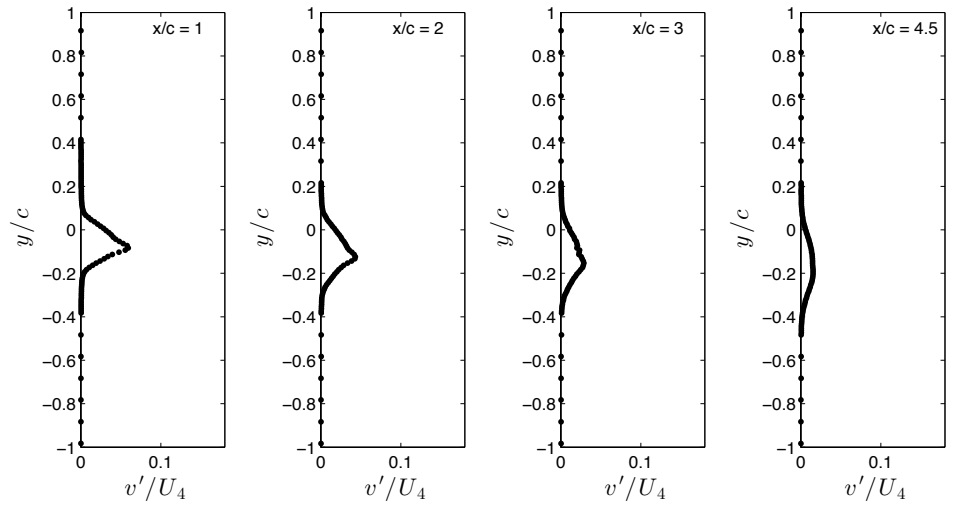

Figure D.21: RMS vertical wake profiles measured with the airfoil operating at $Re_c = 100,000$ and $\alpha = 5°$.

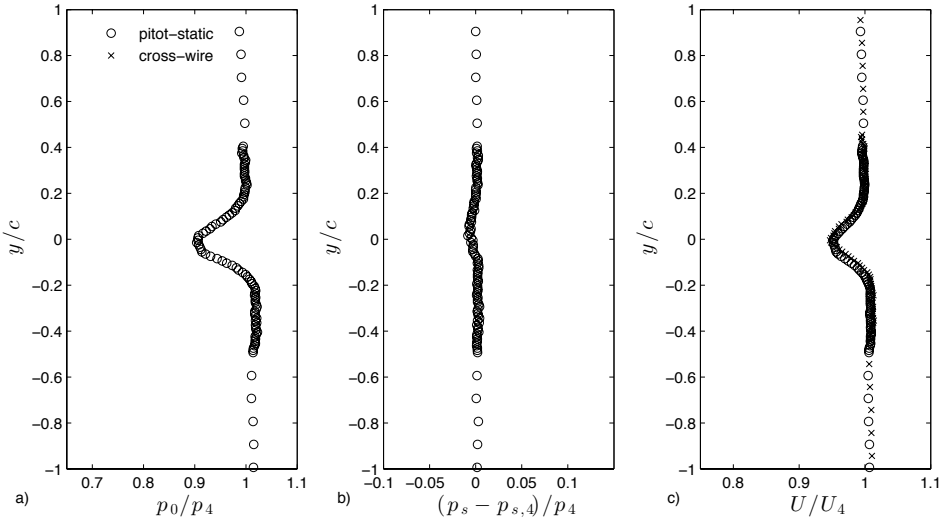

Figure D.22: Pressure profiles measured $4.5c$ downstream from the airfoil set at $\alpha = 0°$. Plot a) shows the total pressure in the wake measured, b) depicts the static pressure variation in the wake, and c) the streamwise velocity profiles based on pitot-static and cross-wire measurements.

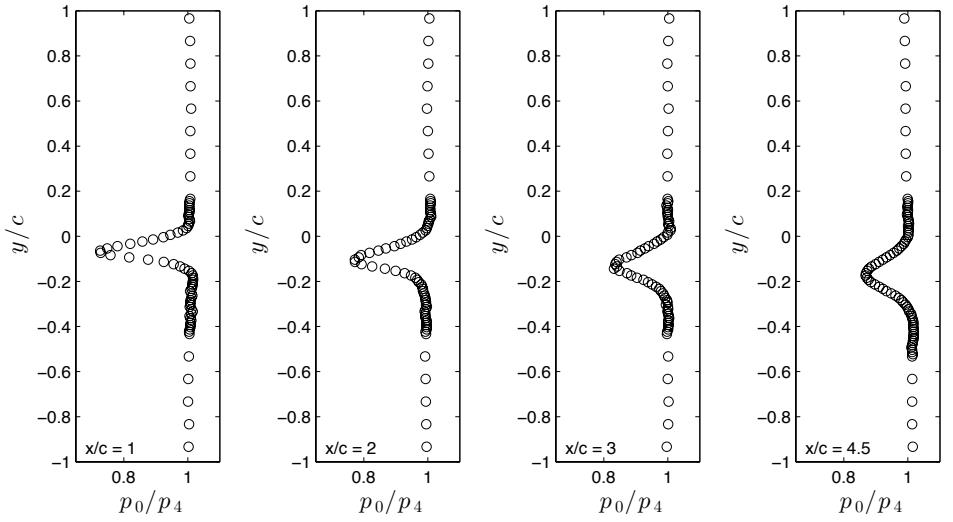

Figure D.23: Total pressure profiles measured in the wake of the airfoil at $\alpha = 5°$.

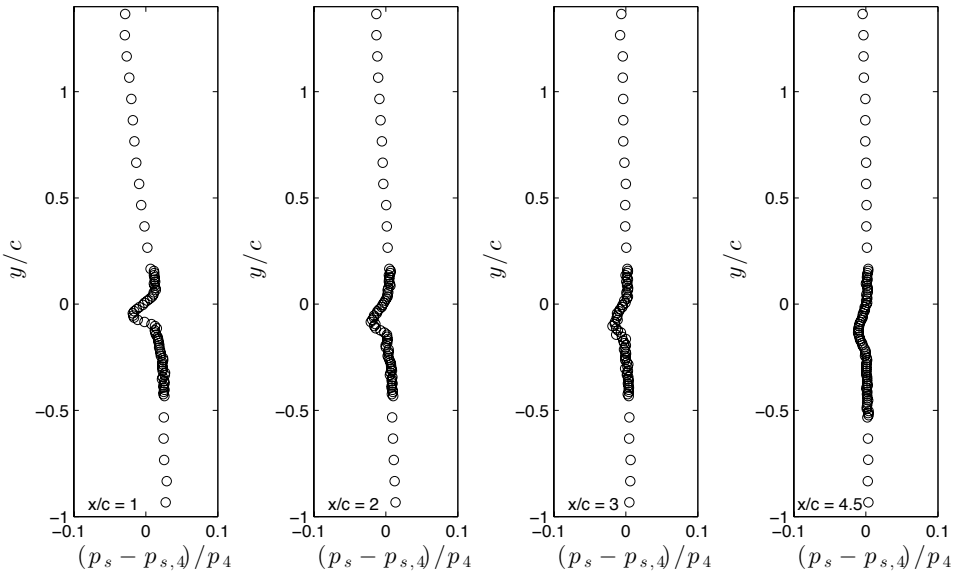

Figure D.24: Static pressure variation in the wake of the airfoil at $\alpha = 5°$.

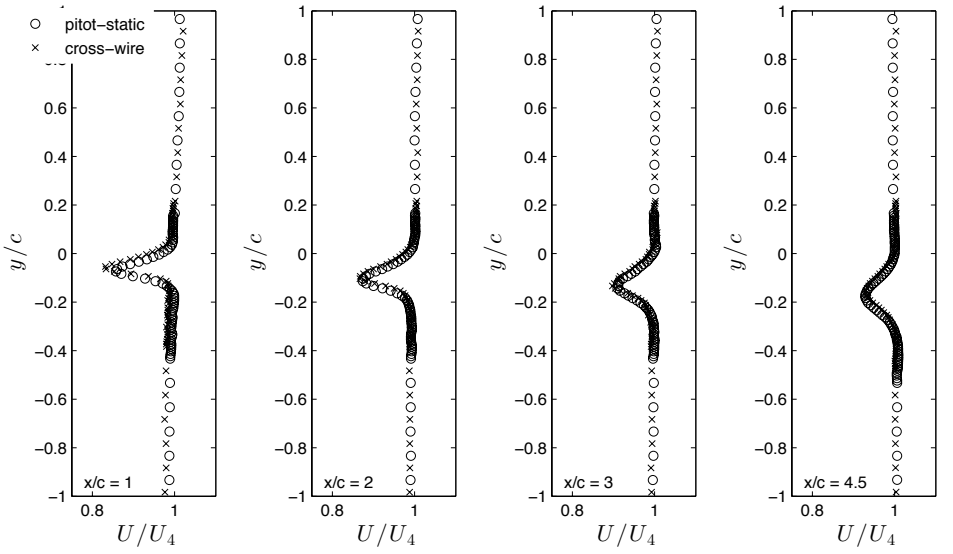

Figure D.25: Streamwise velocity profiles measured in the wake of the airfoil at $\alpha = 5°$.